

# TABLE OF CONTENTS

	ABSTRACT .....	vii
I	INTRODUCTION .....	1
II.	THE IDEAL SPHERICAL CAVITY RESONATOR .....	3
	A. Governing Equations for Fluid Motion .....	3
	B. Spherical Polar Coordinate Solution .....	7
	C. Resonant Frequencies and Motions .....	9
III.	THE EFFECTS OF BOUNDARY SHAPE PERTURBATIONS .....	13
	A. Boundary Perturbation Theory Development .....	13
	B. Calculation of A-Integrals .....	16
	C. Calculation of N-Integrals .....	17
	D. Radial Mode Eigenvalue Perturbations .....	18
	E. Nonradial Mode Eigenvalue Perturbations .....	20
	F. The Nature of the <b>B</b> Matrix .....	25
IV.	MODEL DEFORMATION #1 – HEMISHELL CONSTRUCTION .....	28
	A. Hemishells of Differing Radii .....	28
	B. Shortened or Elongated Hemishells .....	30
	C. Hemishells with Non-coincident Symmetry Axes .....	32
	D. Hemishells with Nonparallel Symmetry Axes .....	34
	E. Eigenfrequency Calculations and Discussion .....	35
V.	MODEL DEFORMATION #2 – AXISYMMETRIC DEFORMATION ...	44
	A. Eigenfrequency Calculation .....	44
	B. A First Method for Computing Deformation Coefficients .....	45
	C. A Second Method for Computing Deformation Coefficients .....	47
VI.	DISSIPATIVE EFFECTS .....	49
	A. Boundary Condition Formalism .....	49
	B. Wave Equation for a Viscous Compressible Fluid .....	50
	C. Viscous and Thermal Boundary Effects .....	59
	D. Compliant Boundary Effects .....	66
	E. Discussion and Examples .....	69

VII.	APPLICATION DISCUSSIONS . . . . .	76
	A. Vibration Detection Sensitivity . . . . .	76
	B. Pressure and Density . . . . .	79
	C. Isotope Ratio Determination . . . . .	81
	D. Phase of Interior Cavity Contents . . . . .	82
	E. Cavity Boundary Characterization . . . . .	88
	F. Solid Fuel Distribution . . . . .	108
VIII.	APPENDICES . . . . .	110
	A. Spherical Polar Coordinates . . . . .	110
	B. Spherical Bessel Functions . . . . .	112
	C. Spherical Harmonic Functions . . . . .	113
	D. Roots of the Spherical Bessel Functions and Their Derivatives . . . .	116
	E. Axisymmetric Fluid Resonance Representations . . . . .	118
	F. Useful Mathematical Relations . . . . .	119
	G. Clebsch-Gordan Coefficients . . . . .	120
	H. <b>B</b> -Matrices and Eigenvalues . . . . .	129
	I. Material Properties of Some Solids . . . . .	134
	J. Material Properties of Some Fluids . . . . .	141
	K. Thermal Expansion Properties of Some Solids . . . . .	144
	L. Thermodynamic Relations . . . . .	145
	M. Representative ICF Capsule Properties . . . . .	147
	N. Notation and Units Summary . . . . .	148
	O. References . . . . .	152

## **ABSTRACT**

Theoretical approaches to fluid characterization and nonideal spherical cavity characterization through resonant acoustic measurements have been compiled, clarified, and extended. Consideration is given to geometric defects, cavity boundary and bulk dissipative mechanisms, and the effects of a compliant boundary. The overall general nature of this report allows it to serve as a primer and reference for a variety of applications. However, the emphasis is toward current Laboratory interests in quantifying geometric properties of millimeter-sized capsules manufactured for fusion implosion studies and equation-of-state experiments.



## I. INTRODUCTION

This report addresses theoretical issues of acoustic characterization of fusion fuels and fusion implosion capsules. Of specific interest are fill-pressure, cryogenic vapor density, solid hydrogen fuel distribution, capsule cavity geometry details, and equation-of-state measurements of hydrogen isotope mixtures. The spherical symmetry of these capsules allows this variety of information to be obtained through the application of acoustic resonator theory. Fortunately, the use of spherical acoustic resonators for determining physical properties of contained fluids has been an area of active research for many years. The resonance signatures provide measures of sound velocity and molecular dissipative effects. Together with various experimental constraints, these quantities translate into equation-of-state data, viscosity, thermal diffusivity, and interestingly, resonator shape parameters. While most experiments are readily designed for precise temperature and pressure control, the greatest attraction of spherical resonators is the ability to approach six-digit accuracy in resonance frequency placement.

Four goals have motivated this report. First, there is a need for compiling the theoretical structure that analyzes the mechanical response of nominally spherical objects. This report seeks to extract and compile the body of knowledge relevant to capsule geometry and fluid characterization. Second, this report seeks to clarify the development of often mathematically involved theories. In this way a greater understanding can be attained and the complete tools for extending certain results can exist in one place. Third, some theories need to be extended and limiting cases examined. Fourth, this report becomes a reference for the experimenter in dealing with this somewhat specialized problem.

Treatment begins with the ideal spherical cavity acoustic resonator. The effects of a nonspherical cavity boundary on the resonance signature is then examined with extensive development of model cavity deformations. Next, the effects of a compliant boundary are examined. Then consideration is given to the dissipative mechanisms inherent to nonideal fluids. Finally, various ties to experimental applications are addressed. Much of the theory and results are compiled, woven, and extended from existing treatments. It

is impossible to present comprehensive citations; however, liberal references are cited in the text which are representative of major efforts. Extensive appendices tabulate information necessary for reproducing and extending calculations, computing acoustic responses and developing the most helpful experiments. The appendices also provide a notation summary and reference list.

I would like to thank several people whose contributions have been valuable in compiling this report: James Hoffer for continually clarifying the special issues of inertial confinement fusion (ICF) capsule characterization; Kevin Vixie for discussions of data analysis; Larry Foreman and Art Nobile for always keeping me focused on relevant issues; and Peter Ebey for suggesting this report in the first place.

## II. THE IDEAL SPHERICAL CAVITY RESONATOR

This opening section develops the resonant response of an inviscid fluid contained by the infinitely rigid wall of a spherical cavity. The normal mode fluid motions and frequencies are described and much of the notation is established for use in later sections. This basic treatment follows closely that of any beginning acoustics text. A good fluid dynamics reference is Pierce (1989).

### A. The Governing Equations for Fluid Motion

The density  $\rho$ , pressure  $P$ , and velocity  $\vec{v}$  of an inviscid fluid are related in time and space through Euler's equation:

$$\rho \frac{\partial \vec{v}}{\partial t} + \rho (\vec{v} \cdot \vec{\nabla}) \vec{v} = -\vec{\nabla} P \quad (1)$$

where the usual vector notation has been used. This equation simply relates the changes in the state variables in space and time. This equation is also nonlinear. Thus, it is advantageous to develop a linear version of equation (1) suitable for small amplitude disturbances. Consider the notation:

$$\rho = \rho_0 + \rho' \quad (2a)$$

$$s = s_0 + s' \quad (2b)$$

$$P = P_0 + P' \quad (2c)$$

$$\vec{v} = \vec{v}_0 + \vec{v}' = \vec{v}' \quad (2d)$$

where the zero subscript is descriptive of the ambient fluid conditions and the prime notation indicates deviations from that ambient. In this case, the ambient conditions are static ( $\vec{v}_0 = 0$ ). The entropy is denoted  $s$ . The primed quantities are restricted to be small relative to the ambient conditions, and  $\vec{v}'$  to be small in the sense that it can only produce small changes in  $\rho$  and  $P$ . Equation (1) is now linearized by keeping only terms linear in the primed quantities:

$$\rho_0 \frac{\partial \vec{v}'}{\partial t} = -\vec{\nabla} P'. \quad (3)$$

This equation is the linear Euler's equation. In a simplistic (but true) sense it says that fluid particles accelerate from regions of higher pressure to regions of lower pressure. Alternately, it says that particle convergence is accompanied by an increase in pressure and vice versa.

There is no *a priori* reason for introducing the velocity potential. It just turns out to be a very convenient way to describe most of what follows. Consider the curl of equation (3):

$$\begin{aligned} \vec{\nabla} \times \left[ \rho_0 \frac{\partial \vec{v}'}{\partial t} = -\vec{\nabla} P' \right] \\ \rho_0 \frac{\partial}{\partial t} (\vec{\nabla} \times \vec{v}') = -\vec{\nabla} \times \vec{\nabla} P'. \end{aligned} \quad (4)$$

Now the right hand side of equation (4) is identically zero. The curl of a gradient is always zero! Thus the left hand side of equation (4) must also equal zero:

$$\frac{\partial}{\partial t} (\vec{\nabla} \times \vec{v}') = 0. \quad (5)$$

This equation is satisfied if the velocity is written as a gradient of some scalar function (since the curl of a gradient is zero, again). Let

$$\vec{v}' \equiv \vec{\nabla} \Psi. \quad (6)$$

$\Psi$  is known as the velocity potential function. It is a scalar whose gradient maps out the velocity field of the fluid according to equation (6). Inserting this equation into equation (3) yields a new expression for the pressure:

$$P' = -\rho_0 \frac{\partial \Psi}{\partial t}. \quad (7)$$

Still, the usefulness of the velocity potential is not obvious. However, it is nice to have a scalar function that completely expresses the fluid properties throughout the volume.



Fluid motion is further governed by the idea that mass is conserved in the system. In other words, movement of mass always accompanies density changes in the system. This idea is expressed mathematically as

$$\vec{\nabla} \bullet \vec{v} + \frac{1}{\rho} \frac{\partial \rho}{\partial t} = 0 \quad (8)$$

which is the mass conservation equation. Once again a linear approximation is sought using equations (2). The result is

$$\rho_0 (\vec{\nabla} \bullet \vec{v}') + \frac{\partial \rho'}{\partial t} = 0. \quad (9)$$

Or, in terms of the velocity potential:

$$\frac{\partial \rho'}{\partial t} = -\rho_0 \nabla^2 \Psi. \quad (10)$$

To study sound propagation in the fluid, we must consider the relationship between the pressure and density. The pressure is written as a function of density and entropy:

$$P = P(\rho, s) = P(\rho_0 + \rho', s_0 + s'). \quad (11)$$

Equation (11) is the equation of state (EOS) for the fluid of interest. If this function is expanded in a Taylor series it is found that

$$P = P(\rho_0, s_0) + \left( \frac{\partial P}{\partial \rho} \right)_0 \rho' + \left( \frac{\partial P}{\partial s} \right)_0 s' + \dots \quad (12)$$

Now for typical acoustic wave propagation,  $s'$  is negligible (acoustic waves are very nearly adiabatic for virtually all acoustic applications of general interest). Immediate correspondences follow:

$$P_0 = P(\rho_0, s_0) \quad (13)$$

$$P' = \left( \frac{\partial P}{\partial \rho} \right)_0 \rho'. \quad (14)$$

The starting point for a workable sound wave propagation equation is equation (14). Taking the time derivative yields:

$$\frac{\partial P'}{\partial t} = \left( \frac{\partial P}{\partial \rho} \right)_0 \frac{\partial \rho'}{\partial t}. \quad (15)$$

Now using equation (10) and the time derivative of equation (7), equation (15) becomes

$$\nabla^2 \Psi = \frac{1}{\left( \frac{\partial P}{\partial \rho} \right)_0} \frac{\partial^2 \Psi}{\partial t^2}. \quad (16)$$

This equation is the wave equation for adiabatic sound wave propagation. The form itself reveals the adiabatic sound speed  $c$  to be given by

$$c^2 = \left( \frac{\partial P}{\partial \rho} \right)_0 \quad (17)$$

so that a compact form is obtained for the wave equation

$$\nabla^2 \Psi - \frac{1}{c^2} \frac{\partial^2 \Psi}{\partial t^2} = 0. \quad (18)$$

For harmonic time varying phenomena, such as is the case for resonant acoustics, the velocity potential can be written

$$\Psi = \psi e^{i\omega t}. \quad (19)$$

Here  $\omega$  is the harmonic angular frequency and use is made of the complex number notation  $i = \sqrt{-1}$ . Using this notation, the wave equation is transformed into the Helmholtz equation:

$$\nabla^2 \psi + k^2 \psi = 0 \quad (20a)$$

$$k \equiv \omega/c. \quad (20b)$$

This expression is the basis for the description of all small amplitude acoustic resonance phenomena. Thus far there is complete generality with regard to fluid properties,

boundary conditions, and fluid volume geometry. It is not descriptive of travelling waves as is equation (18).

## B. Spherical Polar Coordinate Solution

Since the goal is to describe resonances within a spherical enclosure, it can be expected that the boundary conditions and mode shapes (to be encountered later) will be most compactly expressed in terms of spherical polar coordinates. Thus, solutions of equation (20) should be sought within this framework. The Helmholtz equation is

$$\left[ \sin \theta \frac{\partial}{\partial r} \left( r^2 \frac{\partial \psi}{\partial r} \right) + \frac{\partial}{\partial \theta} \left( \sin \theta \frac{\partial \psi}{\partial \theta} \right) + \frac{1}{\sin \theta} \frac{\partial^2 \psi}{\partial \phi^2} \right] + k^2 r^2 \sin \theta \psi = 0. \quad (21)$$

The radial coordinate  $r$  is the distance from the coordinate origin (center of the sphere of interest). The polar coordinate  $\theta$  is analogous to latitude on a globe and is measured in degrees from the vertical. The azimuthal coordinate  $\phi$  is analogous to longitude and is measured in degrees from any reference axis perpendicular to the vertical. The triplet axes  $(\hat{r}, \hat{\theta}, \hat{\phi})$  form a right-handed coordinate system. The solution of equation (21) for regions enclosing the coordinate origin is well known and is simply quoted here:

$$\psi = \sum_{\ell=0}^{\infty} \sum_{m=-\ell}^{+\ell} a_{\ell m} \psi_{\ell m} \quad (22)$$

where

$$\psi_{\ell m} = j_{\ell}(kr) Y_{\ell m}(\theta, \phi). \quad (22a)$$

Equation (22) states that all harmonic fluid motion  $\psi$  can be written as a sum of individual and orthogonal resonant modes  $\psi_{\ell m}$  with various amplitudes  $a_{\ell m}$ . Each resonant mode of order  $\ell$  has radial dependence described by the spherical Bessel function of the same order  $j_{\ell}(kr)$ . Similarly, the angular dependence is described by the spherical harmonic functions  $Y_{\ell m}(\theta, \phi)$ . It is important to recall that the actual velocity

and displacement are calculated using equations (6) and (7). Some of these functions are tabulated here with more detail provided in Appendices B and C.

$$j_0(x) = \frac{\sin x}{x} \quad (23a)$$

$$j_1(x) = \frac{\sin x}{x^2} - \frac{\cos x}{x} \quad (23b)$$

$$j_2(x) = \left( \frac{3}{x^3} - \frac{1}{x} \right) \sin x - \frac{3}{x^2} \cos x. \quad (23c)$$

$$Y_{00}(\theta, \phi) = \sqrt{\frac{1}{4\pi}} \quad (24a)$$

$$Y_{1,-1}(\theta, \phi) = +\sqrt{\frac{3}{8\pi}} \sin \theta e^{-i\phi} \quad (24b)$$

$$Y_{10}(\theta, \phi) = +\sqrt{\frac{3}{4\pi}} \cos \theta \quad (24c)$$

$$Y_{11}(\theta, \phi) = -\sqrt{\frac{3}{8\pi}} \sin \theta e^{+i\phi} \quad (24d)$$

$$Y_{20}(\theta, \phi) = \sqrt{\frac{5}{4\pi}} \left( \frac{3}{2} \cos^2 \theta - \frac{1}{2} \right) \quad (24e)$$

$$Y_{30}(\theta, \phi) = \sqrt{\frac{7}{4\pi}} \left( \frac{5}{2} \cos^3 \theta - \frac{3}{2} \cos \theta \right). \quad (24f)$$

### C. Resonance Frequencies and Motions

The eigenvalues (or frequencies) of the Helmholtz equation are determined by the boundary conditions. For a rigid spherical boundary the normal component of the fluid velocity must vanish at the cavity wall ( $r = a$ )

$$[\hat{r} \cdot \vec{v}']_{r=a} = 0. \quad (26)$$

Here  $\hat{r}$  is the unit vector in the radial direction. For a given resonance mode this condition reduces to

$$\left. \frac{\partial \psi_{\ell m}}{\partial r} \right|_{r=a} = \frac{\partial}{\partial r} [j_{\ell}(kr)]_{r=a} = 0 \quad (27)$$

which is commonly written as

$$j'_{\ell}(ka) = 0 \quad (28)$$

so that the prime indicates a derivative with respect to the radial coordinate and the function is then evaluated at the boundary  $r = a$ . Let  $z_{\ell s}$  be the roots of equation (28). They can be computed directly or looked up in tables. The index  $\ell$  indicates the order of the resonance mode, and the index  $s$  enumerates the infinite number of roots for a given order. The relationship to the modal frequencies is given through equation (20b) as

$$z_{\ell s} = k_{\ell s} a = \frac{2\pi f_{\ell s} a}{c} \quad (29)$$

$$\text{or} \quad f_{\ell s} = \frac{z_{\ell s} c}{2\pi a} \quad (30)$$

where  $c$  is the sound velocity and  $f_{\ell s}$  is the long-sought resonance frequency. Appendix D lists several of the (dimensionless) roots  $z_{\ell s}$ .

It is important to note that the resonance frequencies are independent of the azimuthal index  $m$ . For a given mode index  $\ell$ ,  $m$  can take on  $2\ell+1$  values from  $-\ell$  to  $\ell$ . Because of the high degree of symmetry in this system, each of these  $2\ell+1$  modes has the same frequency. This commonality in frequency is termed *degeneracy*. In a system

with less symmetry (such as a distorted sphere) some or all of this degeneracy would disappear and the frequencies would then have index  $m$  dependence.

Notice also that the velocity potential eigenfunctions appear to be independent of the index  $s$ . This is not actually the case. When equation (22) was written it was not then known that each eigenfunction is satisfied by an infinite number of frequencies (index  $s$ ). This is completely analogous to standing waves in an open ended pipe in which a single eigenfunction  $[\psi = \sin kx]$  is satisfied by an infinite number of frequencies  $[f_s = (s+1)c/2L, s = 0, 1, 2, \dots]$ . This index represents fundamental ( $s = 0$ ) and overtone ( $s > 0$ ) frequencies. With this knowledge, equation (22) can be written as

$$\psi_{\ell ms} = j_\ell(k_{\ell s}r)Y_{\ell m}(\theta, \phi) \quad (31)$$

which explicitly shows all geometric and resonance dependence. Once again,  $k$  is shown without  $m$  dependence because  $k$  is completely degenerate with respect to  $m$ .

Consider first the simplest case  $\ell = 0$ . The allowed values for  $m$  range from  $-\ell$  to  $\ell$  so that  $m = 0$  also. The velocity potential is

$$\psi_{00s} = j_0(k_{0s}r)Y_{00}(\theta, \phi) \quad (32)$$

or more explicitly

$$\psi_{00s} = \sqrt{\frac{1}{4\pi}} \frac{\sin k_{0s}r}{k_{0s}r}. \quad (33)$$

The velocity profile is computed from equation (6) and the pressure distribution from equation (7):

$$\vec{v}' \propto \frac{k_{0s}r \cos(k_{0s}r) - \sin(k_{0s}r)}{k_{0s}r^2} \hat{r} \quad (34)$$

$$P' \propto \frac{\sin(k_{0s}r)}{k_{0s}r}. \quad (35)$$

The velocity and pressure throughout the cavity depend only upon the radial coordinate. The direction of motion is also radial. These  $\ell = 0$  modes are known as radial modes or breathing modes. The roots  $k_{0s}$  are found in the top row of Table D2. The first root represents a physically unrealizable solution. Higher-order roots show typical overtone structure with pressure and velocity nodal surfaces in increasing complexity. A few modes are sketched in the top row of Table E1.

Next consider the  $\ell = 1$  modes. Now  $m$  can take on three values: -1, 0, and 1. Each of these three modes has a different pressure and velocity pattern within the cavity *but the same frequency*. Thus, for clarity's sake, consider the axisymmetric  $m = 0$  mode as a representative example. The velocity potential, velocity, and pressure in the cavity are given by:

$$\psi_{10s} = \sqrt{\frac{3}{4\pi}} \left[ \frac{\sin(k_{1s}r)}{(k_{1s}r)^2} - \frac{\cos(k_{1s}r)}{(k_{1s}r)} \right] \cos\theta \quad (36)$$

$$\begin{aligned} \vec{v}' \propto & \frac{\cos\theta}{(k_{1s}r)^3} \left[ (k_{1s}r)^2 \sin(k_{1s}r) + 2(k_{1s}r) \cos(k_{1s}r) - 2 \sin(k_{1s}r) \right] \hat{r} \\ & - \frac{\sin\theta}{(k_{1s}r)^3} \left[ \sin(k_{1s}r) - (k_{1s}r) \cos(k_{1s}r) \right] \hat{\theta} \end{aligned} \quad (37)$$

$$P' \propto \frac{\cos\theta}{(k_{1s}r)^2} \left[ \sin(k_{1s}r) - (k_{1s}r) \cos(k_{1s}r) \right]. \quad (38)$$

The velocity and pressure now depend upon both the radial and polar coordinates. Already the mathematical description is quite complicated. The roots  $k_{1s}$  are found in the second row of Table D2. The fundamental frequency of this series is the lowest frequency mode of the cavity and is characterized by a sloshing motion from one side of the cavity to the other. This mode and a few of the overtones are sketched in the second row of Table E1.

The mathematical expression of higher-order modes and their overtones quickly becomes unwieldy. However, the sketches of Table E1 neatly summarize all of the basic characteristics. This table shows only the axisymmetric  $m = 0$  modes. The non-axisymmetric  $m \neq 0$  modes have the same frequencies but different azimuthal characteristics.

In Table E1, shades of gray indicate instantaneous local fluid velocity during one half of the harmonic cycle. During the other half of the cycle, fluid flow reverses the pressure. For example, the  $\ell = 0, s = 1$  radial mode has fluid alternately moving outward toward the cavity wall and inward toward the cavity center with frequency  $f_{01}$ . Similarly, the  $\ell = 1, s = 0$  mode has fluid sloshing from one end of the cavity to the other with frequency  $f_{10}$ . Overtone modes show similar behavior with an increasing number of regimes of motion/pressure. Extrapolation to higher order modes and overtones is clear from the table progression.



### III. THE EFFECTS OF BOUNDARY SHAPE PERTURBATIONS

This section outlines the important and useful structure of boundary perturbation theory (BPT) applied to a nearly spherical cavity. The relationship between cavity boundary defects (deviations from sphericity) and changes in the normal mode fluid response are established. The derivations and notation follow that of Mehl (1982 and 1986), although the mathematical framework appears here in greater detail.

#### A. Boundary Perturbation Theory Development

Consider a nearly spherical cavity boundary given by

$$r = a \left[ 1 - \sum_{p,q} \varepsilon_{pq} Y_{pq}(\theta, \phi) \right]. \quad (39)$$

Where  $a$  is the unperturbed cavity radius and  $\varepsilon_{pq} \ll 1$  for all  $p$  and  $q$ . It is convenient to abbreviate the notation of equation (39) as

$$r = a(1 - \varepsilon \bar{g}) \quad (40)$$

where equivalency is understood. The angular perturbation information is contained in the function  $\bar{g}$  which need not be small. The single parameter  $\varepsilon$  represents the entire smallness information necessary for the cavity to be nearly spherical.

The eigenfunctions, equation (31), are no longer orthonormal over this nonspherical cavity volume and do not represent a solution to equation (20). However, because the cavity boundary is only slightly perturbed, it is an excellent approximation to consider the eigenfunction set

$$\varphi_{\ell ms} = \sum_{\ell' m' s'} b_{\ell ms, \ell' m' s'} \psi_{\ell' m' s'} \quad (41)$$

So that each new eigenfunction  $\varphi_{\ell ms}$  is a linear combination of the old eigenfunctions  $\psi_{\ell ms}$ . The correct boundary condition at the perturbed surface  $S$  is given by the generalization of equation (26):

$$\hat{n} \bullet \vec{\nabla} \varphi_{\ell ms} \Big|_S = 0. \quad (42)$$

Where  $\hat{n}$  is the unit normal to the surface  $S$ . With this approach, Morse and Feshbach, (1953) and Mehl (1982), derive an expression for the eigenvalues of this cavity:

$$\frac{k^2}{k_{\ell s}^2} = 1 + \frac{A_{\ell ms, \ell ms}}{k_{\ell s}^2 N_{\ell ms}} + \sum_{\ell' m' s'}^* \frac{|A_{\ell ms, \ell' m' s'}|^2}{N_{\ell ms} N_{\ell' m' s'} (k_{\ell s}^2 - k_{\ell' s'}^2) k_{\ell s}^2} + O(\varepsilon^3). \quad (43)$$

In this expression the unperturbed eigenvalues  $k_{\ell s}$  of equation (29) and the perturbed eigenvalues  $k$  (with any subscripts suppressed) are found. The asterisk on the summation indicates the exclusion of the triplet  $\{\ell ms\}$ . This equation is correct to order  $\varepsilon^2$  although this dependence is not immediately apparent. The  $A$  and  $N$  integrals are defined by

$$A_{\ell ms, \ell' m' s'} \equiv \int_S \psi_{\ell' m' s'}^* \hat{n} \bullet \vec{\nabla} \psi_{\ell ms} dS \quad (44)$$

$$N_{\ell ms} \equiv \int_V |\psi_{\ell ms}|^2 r^2 dr d\Omega. \quad (45)$$

An asterisk superscript indicates complex conjugation,  $dS = r^2 \sin \theta d\theta d\phi$ , and  $d\Omega = \sin \theta d\theta d\phi$ .

Equations (40), (43), and (45) contain all information for calculating the resonance frequencies of a nearly spherical cavity correct to second order in the smallness parameter  $\varepsilon$ . Further development is facilitated by expressions for the radial derivatives of the spherical Bessel functions. From Arfkin (1985) Problem 11.7.4:

$$j'_\ell(k_{\ell s} a) = 0 \quad (28)$$

$$j_\ell''(k_{\ell_s}a) = -\left[1 - \frac{\ell(\ell+1)}{(k_{\ell_s}a)^2}\right] j_\ell(k_{\ell_s}a) \quad (46)$$

$$j_\ell'''(k_{\ell_s}a) = \left[1 - \frac{2\ell(\ell+1)}{(k_{\ell_s}a)^2}\right] \left(\frac{2}{k_{\ell_s}a}\right) j_\ell(k_{\ell_s}a). \quad (47)$$

Now, from condition (40) the Taylor expansions of the spherical Bessel function and its first two derivatives are:

$$j_\ell(k_{\ell_s}r) = j_\ell(k_{\ell_s}a) + O(\varepsilon^2) \quad (48)$$

$$j_\ell'(k_{\ell_s}r) = \varepsilon \bar{g} \frac{j_\ell(k_{\ell_s}a)}{k_{\ell_s}a} \left\{ [(k_{\ell_s}a)^2 - \ell(\ell+1)] + \varepsilon \bar{g} [(k_{\ell_s}a)^2 - 2\ell(\ell+1)] \right\} + O(\varepsilon^3) \quad (49a)$$

$$j_\ell''(k_{\ell_s}r) = -\left[1 - \frac{\ell(\ell+1)}{(k_{\ell_s}a)^2}\right] j_\ell(k_{\ell_s}a) - 2\varepsilon \bar{g} \left[1 - \frac{2\ell(\ell+1)}{(k_{\ell_s}a)^2}\right] j_\ell(k_{\ell_s}a) + O(\varepsilon^2) \quad (49b)$$

Finally, the normal derivative on a spherical surface  $S$  is given in spherical coordinates by

$$\hat{n} \bullet \vec{\nabla} = \frac{\vec{\nabla} S}{|\vec{\nabla} S|} \bullet \left( \hat{r} \frac{\partial}{\partial r} + \frac{\hat{\theta}}{r} \frac{\partial}{\partial \theta} + \frac{\hat{\phi}}{r \sin \theta} \frac{\partial}{\partial \phi} \right). \quad (50)$$

Where specifically from equation (40):

$$S = r - a(1 - \varepsilon \bar{g}). \quad (51)$$

Thus,

$$r^2 \hat{n} \bullet \vec{\nabla} = \frac{r^2 \frac{\partial}{\partial r} + a\varepsilon \frac{\partial \bar{g}}{\partial \theta} \frac{\partial}{\partial \theta} + \frac{a\varepsilon}{\sin^2 \theta} \frac{\partial \bar{g}}{\partial \phi} \frac{\partial}{\partial \phi}}{\left[ 1 + \left( \frac{a\varepsilon}{r} \right)^2 \left( \frac{\partial \bar{g}}{\partial \theta} \right)^2 + \left( \frac{a\varepsilon}{r \sin \theta} \right)^2 \left( \frac{\partial \bar{g}}{\partial \phi} \right)^2 \right]^{1/2}}. \quad (52)$$

## B. Calculation of the $A$ Integrals

Now consider the evaluation of equation (44). Making liberal use of the relations in the previous section, the various components of the integral can be expanded to appropriate orders in  $\varepsilon$ :

$$\psi_{\ell'm's'}^* = Y_{\ell'm'}^*(\theta, \phi) j_{\ell'}(k_{\ell's'} a) \left\{ 1 - \frac{(k_{\ell's'} a)^2}{2} \left[ 1 - \frac{\ell'(\ell'+1)}{(k_{\ell's'} a)^2} \right] \varepsilon^2 \bar{g}^2 + O(\varepsilon^3) \right\} \quad (53)$$

$$r^2 \frac{\partial \psi_{\ell ms}}{\partial r} = k_{\ell s}^2 a^3 j_{\ell}(k_{\ell s} a) Y_{\ell m}(\theta, \phi) \left\{ \left[ 1 - \frac{\ell(\ell+1)}{(k_{\ell s} a)^2} \right] \varepsilon \bar{g} - \varepsilon^2 \bar{g}^2 \right\} + O(\varepsilon^3) \quad (54)$$

$$a \varepsilon \frac{\partial \bar{g}}{\partial \theta} \frac{\partial \psi_{\ell ms}}{\partial \theta} = a \varepsilon \frac{\partial \bar{g}}{\partial \theta} \frac{\partial Y_{\ell m}(\theta, \phi)}{\partial \theta} j_{\ell}(k_{\ell s} a) + O(\varepsilon^3) \quad (55)$$

$$a \varepsilon \frac{\partial \bar{g}}{\partial \phi} \frac{\partial \psi_{\ell ms}}{\partial \phi} = a \varepsilon \frac{\partial \bar{g}}{\partial \phi} \frac{\partial Y_{\ell m}(\theta, \phi)}{\partial \phi} j_{\ell}(k_{\ell s} a) + O(\varepsilon^3) \quad (56)$$

$$\left[ 1 + \left( \frac{a \varepsilon}{r} \right)^2 \left( \frac{\partial \bar{g}}{\partial \theta} \right)^2 + \left( \frac{a \varepsilon}{r \sin \theta} \right)^2 \left( \frac{\partial \bar{g}}{\partial \phi} \right)^2 \right]^{1/2} = 1 + O(\varepsilon^2). \quad (57)$$

Keeping all terms up to order  $\varepsilon^2$ :

$$A_{\ell ms, \ell' m' s'} = \int \left\{ \begin{aligned} & j_{\ell'}(k_{\ell' s'} a) j_{\ell}(k_{\ell s} a) Y_{\ell' m'}^*(\theta, \phi) \times \\ & \left[ a \varepsilon \frac{\partial \bar{g}}{\partial \theta} \frac{\partial Y_{\ell m}(\theta, \phi)}{\partial \theta} + \frac{a \varepsilon}{\sin^2 \theta} \frac{\partial \bar{g}}{\partial \phi} \frac{\partial Y_{\ell m}(\theta, \phi)}{\partial \phi} \right] \\ & + a \varepsilon (k_{\ell s} a)^2 \bar{g} \left( 1 - \frac{\ell(\ell+1)}{(k_{\ell s} a)^2} \right) Y_{\ell m}(\theta, \phi) \\ & - a \varepsilon^2 (k_{\ell s} a)^2 \bar{g}^2 Y_{\ell m}(\theta, \phi) \end{aligned} \right\}. \quad (58)$$

This integral simplifies considerably for the special (but important) case of radial oscillations ( $\ell = 0, m = 0$ ):

$$A_{00s, \ell' m' s'} = k_{0s}^2 a^3 j_{\ell'}(k_{\ell' s} a) j_0(k_{0s} a) [\varepsilon \langle \ell' m' | \bar{g} | 00 \rangle - \varepsilon^2 \langle \ell' m' | \bar{g}^2 | 00 \rangle] + O(\varepsilon^3) \quad (59)$$

$$A_{00s, 00s} = k_{0s}^2 a^3 j_0^2(k_{0s} a) [\varepsilon \langle 00 | \bar{g} | 00 \rangle - \varepsilon^2 \langle 00 | \bar{g}^2 | 00 \rangle] + O(\varepsilon^3) \quad (60)$$

where

$$\langle \ell' m' | x | \ell m \rangle \equiv \int Y_{\ell' m'}^*(\theta, \phi) x Y_{\ell m}(\theta, \phi) d\Omega. \quad (61)$$

### C. Calculation of the $N$ integrals

Now consider the  $N$  integral equation (45). Making the use of Arfken Problem 11.2.1.b:

$$\int_0^x [J_\nu(kr)]^2 r dr = \frac{x^2}{2} \left\{ [J'_\nu(kx)]^2 + \left( 1 + \frac{\nu^2}{(kx)^2} \right) [J_\nu(kx)]^2 \right\} \quad (62)$$

and the substitutions  $x = a(1 - \varepsilon \bar{g})$  and  $\nu = \ell + 1/2$  it can be quickly shown that

$$N_{\ell ms} = \frac{a^3}{2} j_\ell^2(k_{\ell s} a) \left[ 1 - \frac{\ell(\ell+1)}{(k_{\ell s} a)^2} \right] (1 - 2\varepsilon \langle \ell m | \bar{g} | \ell m \rangle) + O(\varepsilon^2). \quad (63)$$

Use has again been made of the shorthand notation of equation (61). For the case  $N_{000}$ , equation (62) cannot be used because  $k = 0$  for this unphysical root. The integral is still required for completeness in subsequent calculations and is given thus:

$$N_{000} = \int_V r^2 dr d\Omega = \frac{a^3}{3} (1 - 3\varepsilon \langle 00 | \bar{g} | 00 \rangle) + O(\varepsilon^3). \quad (64)$$

The general case for overtone radial oscillations ( $\ell = 0, m = 0, s > 0$ ) is given from equation (63) as:

$$N_{000} = \frac{a^3}{2} j_0^2(k_{0s} a) (1 - 2\varepsilon \langle 00 | \bar{g} | 00 \rangle) + O(\varepsilon^3), \quad s > 0. \quad (65)$$

#### D. Radial Mode Eigenvalue Perturbations

Equation (43) can now be evaluated for all resonant modes. Consider first the radial mode eigenvalue shifts to second order in  $\epsilon$ .

$$\frac{k^2}{k_{0s}^2} = 1 + \frac{A_{00s,00s}}{k_{0s}^2 N_{00s}} + \sum_{\ell'm's'}^* \frac{|A_{00s,\ell'm's'}|^2}{N_{00s} N_{\ell'm's'} (k_{0s}^2 - k_{\ell's'}^2) k_{0s}^2} + O(\epsilon^2). \quad (66)$$

This equation is evaluated with equations (59), (60), (63), (64), and (65). The result is

$$\begin{aligned} \frac{k^2}{k_{0s}^2} = & 1 + 2\epsilon \langle 00 | \bar{g} | 00 \rangle - 2\epsilon^2 \langle 00 | \bar{g}^2 | 00 \rangle + 6\epsilon^2 \langle 00 | \bar{g} | 00 \rangle^2 \\ & + 4\epsilon^2 \sum_{\ell'm's'}^{**} \left( \frac{z_{0s}^2}{z_{0s}^2 - z_{\ell's'}^2} \right) \left( \frac{z_{\ell's'}^2}{z_{\ell's'}^2 - \ell'(\ell'+1)} \right) \langle \ell'm' | \bar{g} | 00 \rangle^2 + O(\epsilon^3) \end{aligned} \quad (67)$$

where the double asterisk on the sum indicates omission of the term  $\{00s\}$  as well as the term  $\{000\}$  which has already been evaluated and contributes to the last term of the first line in equation (67). The  $z$  notation of equation (29) is used for compactness. This equation can be simplified by considering the volume change produced by the boundary perturbation. The new cavity volume is given by

$$\tilde{V} = \int \int r^2 dr d\Omega = \frac{4\pi}{3} a^3 (1 - 3\epsilon \langle 00 | \bar{g} | 00 \rangle + 3\epsilon^2 \langle 00 | \bar{g}^2 | 00 \rangle + O(\epsilon^3)). \quad (68)$$

Tilde notation indicates quantities relative to the perturbed cavity volume. The equivalent radius  $\tilde{a}$  for this new volume  $\tilde{V}$  is

$$\tilde{a} = a (1 - 3\epsilon \langle 00 | \bar{g} | 00 \rangle + 3\epsilon^2 \langle 00 | \bar{g}^2 | 00 \rangle)^{1/3}. \quad (69)$$

The eigenvalue shifts are inversely proportional to the radius shift. Thus

$$\frac{\tilde{k}_{0s}^2}{k_{0s}^2} = \frac{a^2}{\tilde{a}^2} = 1 + 2\epsilon \langle 00 | \bar{g} | 00 \rangle - 2\epsilon \langle 00 | \bar{g}^2 | 00 \rangle + 5\epsilon^2 \langle 00 | \bar{g} | 00 \rangle^2 + O(\epsilon^3). \quad (70)$$

Now, subtracting these volume change terms of equation (70) from equation (67):

$$\frac{k^2 - \tilde{k}_{0s}^2}{k_{0s}^2} = \varepsilon^2 \langle 00 | \bar{g} | 00 \rangle^2 + 4\varepsilon^2 \sum_{\ell' m' s'}^{**} \left( \frac{z_{0s}^2}{z_{0s}^2 - z_{\ell' s'}^2} \right) \left( \frac{z_{\ell' s'}^2}{z_{\ell' s'}^2 - \ell'(\ell' + 1)} \right) \langle \ell' m' | \bar{g} | 00 \rangle^2 + O(\varepsilon^3). \quad (71)$$

At this point it is clear that perturbations that do not alter the volume of the cavity do not affect the radial mode frequencies to first order. In other words, all of the terms in equation (71) are second order in the perturbations. Evaluation of the summation terms further simplifies this expression. Mehl (1982) outlines the calculation, and the results are reported here.

$$\frac{k^2 - \tilde{k}_{0s}^2}{k_{0s}^2} = 4\varepsilon^2 \sum_{\ell'=2}^{\infty} S_{\ell' s'} \sum_{m'=-\ell'}^{\ell'} \langle \ell' m' | \bar{g} | 00 \rangle^2 + O(\varepsilon^3) \quad (72)$$

$$S_{\ell' s'} \equiv \sum_{\ell' s' \neq 0s} \frac{z_{0s}^2}{z_{0s}^2 - z_{\ell' s'}^2} \frac{z_{\ell' s'}^2}{z_{\ell' s'}^2 - \ell'(\ell' + 1)}. \quad (73)$$

Notice that the  $\ell' = 0$  term was evaluated and exactly cancels the leading term in equation (71). The  $\ell' = 1$  term evaluates to zero. A useful relation for evaluating the  $S$  constants is given by Mehl (1982):

$$S_{\ell' s'} = \frac{z_{0s'}^2 j_{\ell'}(z_{0s'})}{z_{0s'} j_{\ell'-1}(z_{0s'}) - 2(\ell' + 1) j_{\ell'}(z_{0s'})}, \quad \ell' > 1 \quad (74)$$

and the first few values are explicitly,

$$S_{0s'} = \frac{1}{4} \quad (75)$$

$$S_{1s'} = 0 \quad (76)$$

$$S_{2s'} = -\frac{z_{0s'}^2}{6} \quad (77)$$

$$S_{3s'} = \frac{5z_{0s'}^2}{2(z_{0s'}^2 - 20)} \quad (78)$$

$$S_{4s'} = -\frac{z_{0s'}^2(z_{0s'}^2 - 35)}{10(2z_{0s'}^2 - 35)}. \quad (79)$$

Alternatively, one can use a recursion relation to generate various  $S$  values:

$$S_{\ell's'} = \frac{[2(\ell' - 1)S_{\ell'-1,s'} - z_{0s'}^2]z_{0s'}^2}{4[z_{0s'}^2 - (\ell'^2 - 1)]S_{\ell'-1,s'} + 2(\ell' + 1)z_{0s'}^2}, \quad \ell' \geq 2. \quad (80)$$

### E. Nonradial Mode Eigenvalue Perturbations

Evaluation of the nonradial mode frequency shifts is complicated by their degeneracy. The  $(2\ell + 1)$  unperturbed modes of indices  $\{\ell ms\}$  all have the same eigenvalue  $k_{\ell s}$  rendering equation (43) unworkable. The standard approach in degenerate perturbation theory is to determine the set of linear combinations of eigenfunctions that diagonalizes the mode-coupling matrix. Each set of degenerate modes can be treated separately. As with the radial modes, consider only the perturbed eigenvalues  $k^2$  relative to the eigenvalues of a perfect sphere  $k_{\ell s}^2$  with the same volume as the unperturbed sphere. Making use of equation (70) and equation (43), define the matrix  $\mathbf{B}^{\ell s}$  whose diagonal elements are proportional to the difference of the  $\varepsilon$  coefficients:

$$\mathbf{B}_{mm'}^{\ell s} \equiv \frac{A_{\ell ms, \ell m' s}}{2\varepsilon k_{\ell s}^2 N_{\ell ms}} - \langle 00 | \bar{g} | 00 \rangle \delta_{mm'}. \quad (81)$$

Defining the matrix  $\mathbf{B}^{\ell s}$  in this way allows the degenerate mode frequency shifts to be represented simply as

$$\frac{k^2 - \tilde{k}_{\ell s}^2}{k_{\ell s}^2} = 2\varepsilon \Lambda_m^{\ell s} + O(\varepsilon^2) \quad (82)$$



where the  $\Lambda_m^{\ell_s}$  are the  $(2\ell+1)$  eigenvalues of  $\mathbf{B}^{\ell_s}$ . The remainder of this section is devoted to the reduction of equation (81) in terms of the boundary perturbation function  $\bar{g}$ . The  $A$  and  $N$  integrals are given by equation (58) and equation (63). Using equation (49a) it is readily found that

$$\begin{aligned} \mathbf{B}_{mm'}^{\ell_s} = & \int_S d\Omega Y_{\ell m'}^* \bar{g} Y_{\ell m} \\ & + \frac{1}{z_{\ell_s}^2 - \ell(\ell+1)} \int_S d\Omega Y_{\ell m'}^* \left( \frac{\partial \bar{g}}{\partial \theta} \frac{\partial Y_{\ell m}}{\partial \theta} + \frac{1}{\sin \theta} \frac{\partial \bar{g}}{\partial \phi} \frac{\partial Y_{\ell m}}{\partial \phi} \right) \\ & - \langle 00 | \bar{g} | 00 \rangle \delta_{mm'} + O(\varepsilon). \end{aligned} \quad (83)$$

Further evaluation requires specific information about the cavity shape contained in the function  $\bar{g}$ . Consider a general surface perturbation expressed as an expansion in spherical harmonics:

$$\bar{g}(\theta, \phi) = \sum_{p=0}^{\infty} \sum_{q=-p}^p c_{pq} Y_{pq}(\theta, \phi). \quad (84)$$

Actually, equation (84) is too general because we must require that  $\bar{g}$  is real. For describing such a surface it is appropriate, without loss of generality, to require that  $c_{pq}$  be real and that  $c_{p,-q} = (-1)^q c_{pq}$ . In terms of these specific boundary perturbations, equation (83) can now be expressed as

$$\begin{aligned} \mathbf{B}_{mm'}^{\ell_s} = & \frac{1}{[z_{\ell_s}^2 - \ell(\ell+1)]} \sum_{p=1}^{\infty} \sum_{q=-p}^p c_{pq} \int d\Omega Y_{\ell m'}^* \\ & \times \left( [z_{\ell_s}^2 - \ell(\ell+1)] Y_{pq} Y_{\ell m} + \frac{\partial Y_{pq}}{\partial \theta} \frac{\partial Y_{\ell m}}{\partial \theta} + \frac{1}{\sin^2 \theta} \frac{\partial Y_{pq}}{\partial \phi} \frac{\partial Y_{\ell m}}{\partial \phi} \right) \\ & + O(\varepsilon) \end{aligned} \quad (85)$$

where the  $p=0$  term exactly cancels the volume-change term shown explicitly in equation (83). Amazingly, this expression can be considerably simplified. Consider the integral portion of equation (85)

$$I \equiv \int d\Omega Y_{\ell m'}^* \left( [z_{\ell s}^2 - \ell(\ell+1)] Y_{pq} Y_{\ell m} + \frac{\partial Y_{pq}}{\partial \theta} \frac{\partial Y_{\ell m}}{\partial \theta} + \frac{1}{\sin^2 \theta} \frac{\partial Y_{pq}}{\partial \phi} \frac{\partial Y_{\ell m}}{\partial \phi} \right) \quad (86)$$

and use equation (C17) to obtain the equivalent expression in terms of Associated Legendre Polynomials:

$$I = D \int_0^{2\pi} e^{i(m+q-m')\phi} \times \int_{-1}^1 P_{\ell m'} \left( [z_{\ell s}^2 - \ell(\ell+1)] P_{pq} P_{\ell m} + (1-\xi^2) \frac{\partial P_{pq}}{\partial \xi} \frac{\partial P_{\ell m}}{\partial \xi} - \frac{qm}{(1-\xi^2)} P_{pq} P_{\ell m} \right) d\xi \quad (87)$$

where

$$\xi \equiv \cos \theta \quad (88)$$

is the suppressed argument of the Associated Legendre Polynomials and

$$D \equiv (-1)^{m+q-m'} \left[ \frac{(2\ell+1)^2 (2p+1) (\ell-m)! (\ell-m')! (p-q)!}{(4\pi)^3 (\ell+m)! (\ell+m')! (p+q)!} \right]^{1/2} \quad (89)$$

is a rather complicated constant factor, which will later be reincorporated into expressions in terms of Spherical Harmonic functions. The  $\phi$  integral in equation (87) is zero unless

$$m' = m + q. \quad (90)$$

Now consider the middle term in the  $\xi$  integral

$$I_0 = \int_{-1}^1 P_{\ell m'} (1-\xi^2) \frac{\partial P_{pq}}{\partial \xi} \frac{\partial P_{\ell m}}{\partial \xi} d\xi \quad (91)$$

and define

$$u \equiv P_{\ell m'} (1-\xi^2) \frac{\partial P_{pq}}{\partial \xi} \quad (92)$$

$$v \equiv P_{\ell m} \quad (93)$$

and integrate by parts according to equation (F3) to obtain

$$\begin{aligned} I_0 &= P_{\ell m} P_{\ell m'} (1 - \xi^2) \frac{\partial P_{pq}}{\partial \xi} \Big|_{-1}^1 \\ &\quad - \int_{-1}^1 P_{\ell m} (1 - \xi^2) \frac{\partial P_{\ell m'}}{\partial \xi} \frac{\partial P_{pq}}{\partial \xi} d\xi \\ &\quad - \int_{-1}^1 P_{\ell m} P_{\ell m'} \frac{\partial}{\partial \xi} \left( (1 - \xi^2) \frac{\partial P_{pq}}{\partial \xi} \right) d\xi. \end{aligned} \quad (94)$$

Now the first term of equation (94) vanishes identically. The integrand of the last term can be evaluated and transformed using equation (F5) to obtain

$$\begin{aligned} I_0 &= - \int_{-1}^1 P_{\ell m} (1 - \xi^2) \frac{\partial P_{\ell m'}}{\partial \xi} \frac{\partial P_{pq}}{\partial \xi} d\xi \\ &\quad + \int_{-1}^1 P_{\ell m} P_{\ell m'} P_{pq} \left( p(p+1) - \frac{q^2}{1-\xi} \right) d\xi. \end{aligned} \quad (95)$$

This may not seem like much of an improvement over equation (91). However, the first integral of equation (95) is of the same form as equation (91) with cycled indices. Thus, two more rounds of integration by parts transform equation (95) into

$$I_0 = I_0 + \int_{-1}^1 P_{\ell m} P_{\ell m'} P_{pq} \left( \ell(\ell+1) - \ell(\ell+1) + p(p+1) - \frac{m^2 - m'^2 + q^2}{1-\xi} \right) d\xi \quad (96)$$

or more compactly as

$$I_0 = \frac{1}{2} \int_{-1}^1 P_{\ell m} P_{\ell m'} P_{pq} \left( p(p+1) + \frac{2mq}{1-\xi} \right) d\xi \quad (97)$$

where equation (90) has been used. Now substitute this expression for  $I_0$  back into equation (87) to obtain the **B** matrix integral

$$\begin{aligned}
I &= D \int_0^{2\pi} e^{i(m+q-m')\phi} \\
&\times \left[ z_{\ell s}^2 - \ell(\ell+1) + \frac{1}{2} p(p+1) \right] \int_{-1}^1 P_{\ell m'} P_{pq} P_{\ell m} d\xi \quad \{m' = m + q\}
\end{aligned} \tag{98}$$

which in terms of Spherical Harmonic functions is

$$I = \left[ z_{\ell s}^2 - \ell(\ell+1) + \frac{1}{2} p(p+1) \right] \int_{-1}^1 Y_{\ell m'}^* Y_{pq} Y_{\ell m} d\Omega. \tag{99}$$

And finally, the **B** matrix expression can be compactly written as

$$\mathbf{B}_{mm'}^{\ell s} = \sum_{p=1}^{\infty} \sum_{q=-p}^p d_{pq} \langle \ell m' | Y_{pq} | \ell m \rangle \tag{100}$$

where

$$d_{pq} \equiv c_{pq} \left[ 1 + \frac{\frac{1}{2} p(p+1)}{z_{\ell s}^2 - \ell(\ell+1)} \right], \tag{101}$$

$$\langle \ell m' | Y_{pq} | \ell m \rangle \equiv \int d\Omega Y_{\ell m'}^* Y_{pq} Y_{\ell m}. \tag{102a}$$

Thus, the calculation of the degenerate mode frequency shifts of equation (82) has been reduced to a calculation of the eigenvalues of a **B** matrix whose elements are written in terms of integrals of Spherical Harmonic functions. Fortunately, integrals of this form are well known in quantum mechanics and are readily evaluated in terms of Clebsch-Gordan (*C*) coefficients. Specifically,

$$\langle \ell m' | Y_{pq} | \ell m \rangle = \sqrt{\frac{2p+1}{4\pi}} C(\ell p \ell; m q m') C(\ell p \ell; 0 0 0) \tag{102b}$$

where the *C* coefficients can be evaluated by a variety of methods or simply looked up in tables. Further, it is advantageous to define the product coefficient

$$\tilde{C}(\ell p \ell; m q m') \equiv C(\ell p \ell; m q m') C(\ell p \ell; 000) \quad (103)$$

for ease of coefficient tabulation and of **B** matrix construction.

Appendix G lists a large variety of  $C$  and  $\tilde{C}$  coefficients relevant to this work. Equation (102) is zero unless  $m' = m + q$  as would be expected as seen in the derivation. Interestingly, the symmetry properties of the  $C$  coefficients also require that  $p$  is even. Thus a general result of the BPT is that only even-order boundary perturbations affect the eigenfrequencies to first order in  $\varepsilon$ .

## F. The Nature of the B Matrix

To bring the **B** matrix from the abstract into the realm of application, consider the construction and eigenfrequency extraction for a few cases. Recall that in the **B** matrix derivation it was convenient to express the perturbed boundary by equation (40) instead of the actual boundary condition given in equation (39). The shape function  $\bar{g}$  was finally given character in equation (84) but still did not contain any “smallness” information. Now return to the frequency shift definition of equation (82) and incorporate the smallness parameter  $\varepsilon$  into the shape perturbation function  $\bar{g}$ . That is  $c_{pq} \ll 1$  for all  $p$  and  $q$ . Then correct to order  $c_{pq}$  equation (82) is recast as

$$\frac{\tilde{f}_{\ell ms} - f_{\ell s}}{f_{\ell s}} = \frac{\Delta \tilde{f}_{\ell ms}}{f_{\ell s}} = \Lambda_m^{\ell s} = Ei\{\mathbf{B}_{mm'}^{\ell s}\} \quad (104)$$

where **B** can now be compactly written as

$$\mathbf{B}_{mm'}^{\ell s} = \sum_{\substack{p=2 \\ \text{even}}}^{2\ell} d_{pq} \sqrt{\frac{2p+1}{4\pi}} \tilde{C}(\ell p \ell; m q m') \quad (105)$$

or equivalently

$$\mathbf{B}_{mm'}^{\ell s} = \sum_{\substack{p=2 \\ \text{even}}}^{2\ell} K_{\ell ps} \bar{C}(\ell p \ell; m q m') c_{pq} \quad (106)$$

where the new constant  $K$  is defined as

$$K_{\ell ps} \equiv \sqrt{\frac{2p+1}{4\pi}} \left( \frac{z_{\ell s}^2 - \ell(\ell+1) + \frac{1}{2}p(p+1)}{z_{\ell s}^2 - \ell(\ell+1)} \right). \quad (107)$$

The conditions  $m' = m + q$  and  $|m|, |m'| \leq \ell$  are implicit in the evaluation of  $\tilde{C}$ . While the condition that  $p$  be even is also implicit in the evaluation of  $\tilde{C}$ , it is explicitly stated in equation (106) to emphasize the dependence only on even orders of  $c_{pq}$ . Notice also that the eigenfrequencies  $\tilde{f}_{\ell ms}$  now have index  $m$  that enumerates the now nondegenerate frequencies (formerly  $2\ell+1$  degenerate at frequency  $f_{\ell s}$ ). However, it is possible that for a given perturbation the degeneracy may not be completely broken ( $\mathbf{B}$  may have repeated eigenvalues).

Consider the matrix describing the frequency shifts of the lowest-order resonance  $f_{10}$  and the overtones  $f_{1s}$ . In this case  $\ell = 1$  and  $p = 2$  only, and along with the coefficients in Table G1 the  $\mathbf{B}$  matrix is readily constructed:

$$\begin{aligned} \mathbf{B}^{1s} &= \frac{K_{12s}}{5} \begin{bmatrix} -c_{20} & -\sqrt{3}c_{21} & -\sqrt{6}c_{22} \\ -\sqrt{3}c_{21} & +2c_{20} & +\sqrt{3}c_{21} \\ -\sqrt{6}c_{22} & +\sqrt{3}c_{21} & -c_{20} \end{bmatrix} \\ &= \frac{1}{5} \sqrt{\frac{5}{4\pi}} \left( \frac{z_{1s}^2 + 1}{z_{1s}^2 - 2} \right) \begin{bmatrix} -c_{20} & -\sqrt{3}c_{21} & -\sqrt{6}c_{22} \\ -\sqrt{3}c_{21} & +2c_{20} & +\sqrt{3}c_{21} \\ -\sqrt{6}c_{22} & +\sqrt{3}c_{21} & -c_{20} \end{bmatrix} \end{aligned} \quad (108)$$

where the real-boundary condition  $c_{p,-q} = (-1)^q c_{pq}$  has been used.

The  $\mathbf{B}$  matrices and their eigenvalues have several interesting properties that are illustrated nicely in equation (108) and in the equations in Appendix H.

1.  $\mathbf{B}^{\ell s}$  is symmetric. Namely,  $\mathbf{B}_{m,n}^{\ell s} = \mathbf{B}_{n,m}^{\ell s}$ .
2.  $\mathbf{B}^{\ell s}$  has symmetry properties about the backwards diagonal. Specifically,  $\mathbf{B}_{m,n}^{\ell s} = -\mathbf{B}_{-n,-m}^{\ell s}$  if  $|m| \neq |n|$  and  $\mathbf{B}_{m,n}^{\ell s} = \mathbf{B}_{-n,-m}^{\ell s}$  otherwise.
3. Properties 1 and 2 together reduce the number of independent elements from  $(2\ell + 1)^2$  to  $(\ell + 1)^2$ , which nicely reduces the calculations necessary for constructing a matrix  $\mathbf{B}^{\ell s}$ . Expressions for the eigenvalues are also simplified considerably.
4.  $\text{Tr}\{\mathbf{B}^{\ell s}\} = 0$ . This property is equivalent to having eigenvalues that sum to zero. Thus to first order in the perturbation parameters  $c_{pq}$ , the sum of all the frequency shifts  $\Delta\tilde{f}_{\ell ms}$  for a given resonance set is zero, and the average of all frequencies  $\tilde{f}_{\ell ms}$  is equal to the degenerate parent frequency  $f_{\ell s}$ .
5. For the case of axisymmetric perturbations ( $q = 0$ ), the number of independent eigenvalues is  $\ell + 1$ , which are the diagonal elements of each matrix. This partial degeneracy breaking is indicative of axisymmetry and does not occur generally for any other constraints on the coefficients  $c_{pq}$ .
6. The matrix elements and eigenvalues depend only upon even-order shape perturbations ( $p$  even). Any cavity distortion described by odd-order perturbations does not affect the cavity resonances to first order in the  $c_{pq}$ .

#### IV. MODEL DEFORMATION #1 – HEMISHELL CONSTRUCTION

This section considers the cavity shape perturbations that might naturally arise from construction by adjoining two spherical hemishells. Certain predictable deformations may be present:

1. The hemishells have different radii.
2. Either hemishell is cut long or short, or the two are bonded long or short.
3. The symmetry axes are parallel but not coincident.
4. The two symmetry axes have an angular offset (non-parallel).

The perturbation parameters for each type of defect are determined separately. The eigenfrequency calculations are then collectively discussed at the end of this section. Mehl (1986) first addressed this type of perturbation.

##### A. Hemishells of Different Radii

Let the radius of one hemishell (say the top) differ from the radius of the other hemishell (say the bottom). Then the radius  $r$  of the cavity can be written:

$$r = \begin{cases} a(1 + \beta) & \text{top} \\ a(1 - \beta) & \text{bottom} \end{cases} \quad (109)$$

where  $a$  is the nominal cavity radius and the small perturbation parameter  $\beta$  is chosen to preserve the cavity volume to first order in  $\beta$ . The entire cavity profile can be expressed as:

$$\frac{r - a}{r} = \beta h(\cos \theta) \quad (110)$$

where

$$h(x) \equiv \begin{cases} +1 & x \geq 0 \\ -1 & x < 0 \end{cases}. \quad (111)$$



The goal is to express this perturbation in terms of an expansion in spherical harmonic functions so that the form of equation (84) is met and the full power of the boundary perturbation theory can be brought to bear. Consider the expansion

$$h(\cos \theta) \equiv \sum_{pq} b_{pq} Y_{pq}(\theta, \phi). \quad (112)$$

The expansion coefficients are determined uniquely by

$$b_{pq} = \int h(\cos \theta) Y_{pq}(\theta, \phi) d\Omega. \quad (113)$$

It is convenient to rewrite this expression in terms of Associated Legendre Polynomials:

$$\begin{aligned} b_{pq} &= \int_0^{2\pi} e^{iq\phi} d\phi \int_{-\pi/2}^{+\pi/2} h(\cos \theta) g_{pq} P_{pq}(\cos \theta) \sin \theta d\theta \\ &= \int_0^{2\pi} e^{iq\phi} d\phi \int_{-1}^{+1} h(x) g_{pq} P_{pq}(x) dx \end{aligned} \quad (114)$$

where  $g_{pq}$  is yet another constant defined by

$$g_{pq} \equiv (-1)^q \sqrt{\frac{2p+1}{4\pi} \frac{(p-q)!}{(p+q)!}}. \quad (115)$$

The  $\phi$  integral in equation (114) vanishes unless  $q = 0$ , in which case it evaluates to  $2\pi$ .

Thus the nonzero expansion coefficients are

$$b_{p0} = 2\pi g_{p0} \int_{-1}^{+1} h(x) P_p(x) dx. \quad (116)$$

Now  $h(x)$  is an odd function over the interval  $[-1 < x < 1]$  and therefore  $b_{p0}$  vanishes unless  $p$  is also odd. In this case

$$b_{p0} = 4\pi g_{p0} \int_0^{+1} P_p(x) dx. \quad (117)$$

Using equation (F6) to evaluate the integral yields (after an integration by parts and various simple integral evaluations)

$$\int_0^{+1} P_p(x) dx = -\frac{1}{p} P_{p+1}(x=0). \quad (118)$$

Because  $p+1$  is even, this expression is evaluated using equation (F9), giving a working expression for the expansion coefficients:

$$b_{p0} = 4\pi g_{p0} (-1)^{(p-1)/2} \frac{p!!}{p(p+1)!!} \quad \{p \text{ odd}\} \quad (119)$$

and two equivalent expressions for the perturbation:

$$\frac{r-a}{r} = \beta \sum_{\substack{p=1 \\ \text{odd}}}^{\infty} b_{p0} Y_{p0}(\theta, \phi) \text{ and} \quad (120)$$

$$\frac{r-a}{r} = \beta \sum_{\substack{p=1 \\ \text{odd}}}^{\infty} (-1)^{(p-1)/2} \frac{(2p+1)}{p} \frac{p!!}{(p+1)!!} P_p(\cos \theta). \quad (121)$$

## B. Shortened or Elongated Hemishells

One or both hemishells may have a symmetry axis that is cut or bonded longer or shorter than the intended radius. Again consider top and bottom hemishells. The radius of the cavity can be written

$$r = \begin{cases} a(1 + \sigma \cos \theta) & \text{top} \\ a(1 - \sigma \cos \theta) & \text{bottom} \end{cases} \quad (122)$$

where  $a$  is the nominal cavity radius and the small perturbation parameter  $\sigma$  is chosen to preserve the cavity volume to first order in  $\sigma$ . The entire cavity profile can be expressed as:

$$\frac{r-a}{r} = \sigma \cos \theta h(\cos \theta) \quad (123)$$

where  $h$  is the same step function given by equation (111). As before an expansion in Spherical Harmonic functions is sought for equation (123). The expansion coefficients are again labeled  $b_{pq}$  because (as it will turn out later) only even  $p$  terms will be needed. The coefficients are defined by

$$\cos \theta h(\cos \theta) \equiv \sum_{pq} b_{pq} Y_{pq}(\theta, \phi), \quad (124)$$

$$b_{pq} = \int \cos \theta h(\cos \theta) Y_{pq}(\theta, \phi) d\Omega. \quad (125)$$

Once again recognizing that the coefficients vanish unless  $q=0$  and recasting the integral in terms of Associated Legendre Polynomials:

$$b_{p0} = 2\pi g_{p0} \int_{-1}^{+1} h(x) x P_p(x) dx \quad (126)$$

where  $g$  is the same constant given by equation (115). Now  $h(x)x$  is an even function over the interval  $[-1 < x < 1]$  so that the integral vanishes unless  $P_p(x)$  is an even function.

Thus  $p$  must be even and equation (126) reduces to

$$b_{p0} = 4\pi g_{p0} \int_0^{+1} x P_p(x) dx \quad \{p \text{ even}\}. \quad (127)$$

Now using equation (F7) along with some integrations by parts, the integral part of this expression reduces to

$$\int_0^{+1} x P_p(x) dx = \frac{1}{2p+1} \left[ \int_0^{+1} P_{p-1}(x) dx - \int_0^{+1} P_{p+1}(x) dx \right]. \quad (128)$$

Both of the right-hand-side integrals are odd-order functions of the form evaluated by equation (118) and equation (F9). The result is

$$b_{p0} = 4\pi g_{p0} (-1)^{(p-2)/2} \frac{(p+1)!!}{(p^2-1)(p+2)!!} \quad \{p \text{ even}\}. \quad (129)$$

And this second model perturbation can be expressed as

$$\frac{r-a}{r} = \sigma \sum_{\substack{p=2 \\ \text{even}}}^{\infty} b_{p0} Y_{p0}(\theta, \phi) \text{ or} \quad (130)$$

$$\frac{r-a}{r} = \sigma \sum_{\substack{p=2 \\ \text{even}}}^{\infty} (-1)^{(p-2)/2} \frac{(2p+1)}{(p^2-1)} \frac{(p+1)!!}{(p+2)!!} P_p(\cos \theta). \quad (131)$$

### C. Parallel and Noncoincident Symmetry Axes

A third possible perturbation is that which might occur if the symmetry axes of the two hemishells are not coincident due to a lateral shift (in the common equatorial plane). In this case the symmetry axes are still parallel and relative to a common origin the radius of the cavity is expressed as

$$r = \begin{cases} a(1 + \gamma \sin \theta \cos \phi) & \text{top} \\ a(1 - \gamma \sin \theta \cos \phi) & \text{bottom} \end{cases} \quad (132)$$

where  $\gamma$  is a small perturbation parameter chosen, once again, so that the cavity volume is preserved to first order in  $\gamma$ . The azimuthal angle  $\phi$  is measured from the displacement vector describing the lateral shift. The complete radial profile is written using the  $h(x)$  step function as

$$\frac{r-a}{r} = \gamma \sin \theta \cos \phi h(\cos \theta). \quad (133)$$

The appropriate expansion in spherical harmonics will now be addressed in the usual way making use of the now familiar expansion coefficients  $b_{pq}$ . Again, this repeated use of the  $b$  coefficient symbol will be justified in the end because for this case it will be shown that the only contributions come from  $p$  even and  $q = \pm 1$ . Proceeding as before:

$$\sin \theta \cos \phi h(\cos \theta) \equiv \sum_{pq} b_{pq} Y_{pq}(\theta, \phi) \quad (134)$$

$$\begin{aligned} b_{pq} &= \int \sin \theta \cos \phi h(\cos \theta) Y_{pq}(\theta, \phi) d\Omega \\ &= \int_0^{2\pi} \cos \phi e^{iq\phi} d\phi \int_{-1}^{+1} g_{pq} \sqrt{1-x^2} h(x) P_{pq}(x) dx. \end{aligned} \quad (135)$$

First consider the  $\phi$  integral. Writing  $\cos \phi$  in terms of exponential functions:

$$\int_0^{2\pi} \cos \phi e^{iq\phi} d\phi = \frac{1}{2} \int_0^{2\pi} (e^{i\phi} + e^{-i\phi}) e^{iq\phi} d\phi \quad (136)$$

from which it is readily determined that

$$\int_0^{2\pi} \cos \phi e^{iq\phi} d\phi = \begin{cases} \pi & \text{if } q = \pm 1 \\ 0 & \text{otherwise} \end{cases}. \quad (137)$$

Next consider the specific case  $q = -1$  for which

$$b_{p,-1} = \pi g_{p,-1} \int_{-1}^{+1} \sqrt{1-x^2} h(x) P_{p,-1}(x) dx. \quad (138)$$

Now  $h(x)$  is odd and  $\sqrt{1-x^2}$  is even over the interval  $[-1 \leq x \leq 1]$  so that  $P_{p,-1}(x)$  must be odd. Thus,  $p$  must be even (yes even) leading to

$$b_{p,-1} = 2\pi g_{p,-1} \int_0^{+1} \sqrt{1-x^2} P_{p,-1}(x) dx \quad \{p \text{ even}\}. \quad (139)$$

This equation is quickly evaluated with the aid of equation (F8) and equation (128). The result is

$$b_{p,-1} = -2\pi g_{p,-1} (-1)^{(p-2)/2} \frac{(p+1)!!}{(p^2-1)(p+2)!!} \quad \{p \text{ even}\}. \quad (140)$$

In considering the case of  $q = +1$  it is only necessary to recognize that the  $b_{p,\pm 1}$  must describe a real boundary. Because the spherical harmonic functions are complex, this “reality” condition is

$$b_{p,-q} = (-1)^q b_{pq}^* \quad (141)$$

or for the present case

$$b_{p1} = -b_{p,-1} \quad (142)$$

so that

$$\begin{aligned} b_{p1} &= 2\pi g_{p,-1} (-1)^{(p-2)/2} \frac{(p+1)!!}{(p^2-1)(p+2)!!} \\ &= 2\pi g_{p1} (-1)^{(p-2)/2} \frac{p}{(p-1)} \frac{(p+1)!!}{(p+2)!!} \quad \{p \text{ even}\} \end{aligned} \quad (143)$$

where it is easily verified that  $g_{p,-1} = p(p+1)g_{p1}$ . The perturbation expansion can now be written as

$$\frac{r-a}{r} = \gamma \sum_{\substack{p=2 \\ \text{even}}}^{\infty} [b_{p1} Y_{p1}(\theta, \phi) + b_{p,-1} Y_{p,-1}(\theta, \phi)] \quad (144)$$

or equivalently as

$$\frac{r-a}{r} = 2\gamma \sum_{\substack{p=2 \\ \text{even}}}^{\infty} b_{p1} \operatorname{Re}\{Y_{p1}(\theta, \phi)\}. \quad (145)$$

#### D. The Hemishell Symmetry Axes Show an Angular Offset

If the two symmetry axes coincide at the spherical cavity center then any angular offset does not distort the cavity shape. This apparent deformation is simply a rotation about a center of radial symmetry. This case need not be considered further.

## E. Eigenfrequency Calculations and Discussion

The results of the model perturbation calculations are collected here for convenience and clarity. The cavity shape is assumed linear in the perturbation parameters.

$$\begin{aligned}
 \frac{r-a}{r} = & \beta \sum_{\substack{p=1 \\ \text{odd}}}^{\infty} b_{p0} Y_{p0}(\theta, \phi) \\
 & + \sigma \sum_{\substack{p=2 \\ \text{even}}}^{\infty} b_{p0} Y_{p0}(\theta, \phi) \\
 & + \gamma \sum_{\substack{p=2 \\ \text{even}}}^{\infty} [b_{p1} Y_{p1}(\theta, \phi) + b_{p,-1} Y_{p,-1}(\theta, \phi)]
 \end{aligned} \tag{146}$$

$$b_{pq} = \begin{cases} 4\pi g_{pq} (-1)^{(p-1)/2} \frac{p!!}{p(p+1)!!} & \text{if } p \text{ odd and } q = 0 \\ 4\pi g_{pq} (-1)^{(p-2)/2} \frac{(p+1)!!}{(p^2-1)(p+2)!!} & \text{if } p \text{ even and } q = 0 \\ 2\pi g_{pq} (-1)^{(p-2)/2} \frac{p}{(p-1)} \frac{(p+1)!!}{(p+2)!!} & \text{if } p \text{ even and } q = +1 \\ 2\pi g_{pq} (-1)^{(p-2)/2} \frac{(p+1)!!}{(p^2-1)(p+2)!!} & \text{if } p \text{ even and } q = -1 \end{cases} \tag{147}$$

$$g_{pq} \equiv (-1)^q \sqrt{\frac{2p+1}{4\pi} \frac{(p-q)!}{(p+q)!}}. \tag{148}$$

Because equation (84) demonstrates that

$$\frac{r-a}{a} = \sum_{p=0}^{\infty} \sum_{q=-p}^p c_{pq} Y_{pq}(\theta, \phi) \tag{149}$$

there is the immediate correspondence between the general perturbation coefficients  $c$  and the model perturbation coefficients  $b$ :

$$c_{pq} = \begin{cases} \beta b_{pq} & \text{if } p \text{ odd and } q = 0 \\ \sigma b_{pq} & \text{if } p \text{ even and } q = 0 \\ \gamma b_{pq} & \text{if } p \text{ even and } q = \pm 1 \end{cases}. \quad (150)$$

Thus, the boundary perturbation solution given by equations (104) through (107) can be readily applied. First, the  $\mathbf{B}$  matrices are constructed. Then the eigenvalues are obtained which are proportional to the eigenfrequency shifts. Recall that the  $\mathbf{B}$  matrices and the resulting frequency shifts depend only upon even-order perturbations. The first model perturbation, described by the parameter  $\beta$ , is of odd order. Thus, to first order in  $\beta$ , hemishells of different radii do not contribute to the degeneracy breaking of the spherical cavity eigenfrequencies.

Consider the simplest case of matrix  $\mathbf{B}^{1s}$ . From the general form of equation (H3) and the relations of this section,

$$\mathbf{B}^{1s} = \frac{K_{12s}}{5} \begin{bmatrix} -\sigma b_{20} & -\sqrt{3}\gamma b_{21} & 0 \\ -\sqrt{3}\gamma b_{21} & +\sigma b_{20} & +\sqrt{3}\gamma b_{21} \\ 0 & +\sqrt{3}\gamma b_{21} & -\sigma b_{20} \end{bmatrix}. \quad (151)$$

Using the easily verified expression

$$\frac{b_{p1}}{b_{p0}} = \frac{-b_{p,-1}}{b_{p0}} = -\frac{\sqrt{p(p+1)}}{2} \quad (152)$$

equation (151) reduces to



$$\mathbf{B}^{1s} = \frac{1}{8} \frac{z_{1s}^2 + 1}{z_{1s}^2 - 2} \begin{bmatrix} -\sigma & +\frac{3}{\sqrt{2}}\gamma & 0 \\ +\frac{3}{\sqrt{2}}\gamma & +2\sigma & -\frac{3}{\sqrt{2}}\gamma \\ 0 & -\frac{3}{\sqrt{2}}\gamma & -\sigma \end{bmatrix}. \quad (153)$$

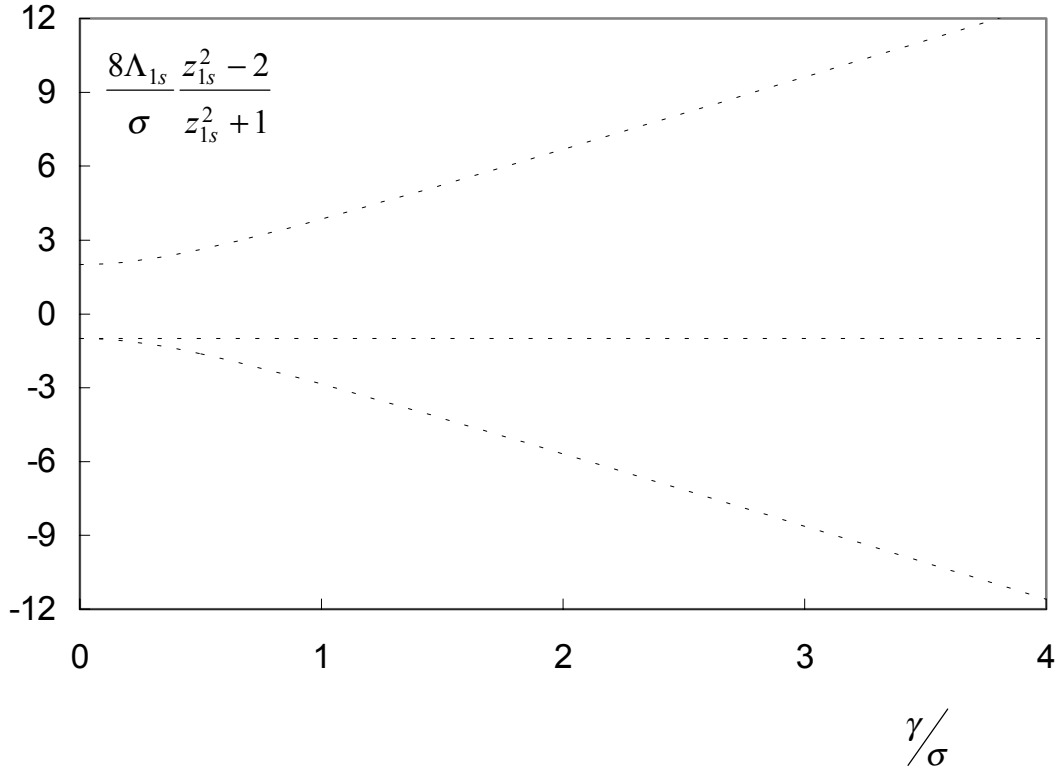
Aside from the matrix prefactor, the three eigenvalues are

$$\Lambda^{1s} = -\sigma, \frac{\sigma}{2} \pm \frac{3}{2} \sqrt{\sigma^2 + 4\gamma^2}. \quad (154)$$

If the only perturbation is a lateral offset ( $\gamma \neq 0$  and  $\sigma = 0$ ), then the eigenvalues are equally spaced:

$$\Lambda^{1s} = 0, \pm 3\gamma. \quad (155)$$

If  $\sigma$  is nonzero, then the eigenvalues depend upon both parameters as shown in the following graph. For  $\gamma = 0$  the degeneracy is only partly broken – there are only two distinct eigenvalues instead of the maximum possible of three. This appearance of only  $p+1$  eigenvalues instead of  $2p+1$  is characteristic of axisymmetric shape perturbations.



In the absence of perturbations other than those described in this section, the measured frequency splitting for any of the  $f_{1s}$  fluid resonances in the cavity is in principle sufficient for characterizing the cavity in terms of the two parameters  $\sigma$  and  $\gamma$ . The measured frequency splitting for any single cavity resonance is usually sufficient. This idea is developed more fully as the matrix  $\mathbf{B}^{2s}$  is now considered.

The matrix  $\mathbf{B}^{2s}$  for the model perturbation is constructed from the general form equation (H4) making liberal use of equations (H2), (147), and (150). Notice that despite the ever-growing number of  $c_{pq}$  parameters that must be included in the calculations, these are always reducible to the two quantities  $\sigma$  and  $\gamma$  which (along with the known  $z_{pq}$  roots) are sufficient for computing the entire resonance frequency response. The result is

$$\mathbf{B}^{2s} = \frac{\hat{Z}}{112} \begin{bmatrix} -(20+Z)\sigma & (30+5Z)\gamma & 0 & 0 & 0 \\ (30+5Z)\gamma & (10+4Z)\sigma & -15\sqrt{6}(Z-1)\gamma & 0 & 0 \\ 0 & -15\sqrt{6}(Z-1)\gamma & (20-6Z)\sigma & 15\sqrt{6}(Z-1)\gamma & 0 \\ 0 & 0 & 15\sqrt{6}(Z-1)\gamma & (10+4Z)\sigma & -(30+5Z)\gamma \\ 0 & 0 & 0 & -(30+5Z)\gamma & -(20+Z)\sigma \end{bmatrix} \quad (156)$$

where

$$Z \equiv \frac{z_{2s}^2 + 4}{z_{2s}^2 - 3} \quad \text{and} \quad \hat{Z} \equiv \frac{z_{2s}^2 - 3}{z_{2s}^2 - 6}. \quad (157)$$

Expressions for the eigenvalues are rather complicated in spite of the symmetry evident in  $\mathbf{B}^{2s}$ . It is worthwhile to examine some special cases. First, the axisymmetric case is determined by  $\gamma = 0$  for which three unique eigenvalues are found:

$$\Lambda^{2s} = \left\{ \begin{array}{c} -\left( \frac{3z_{2s}^2 - 8}{z_{2s}^2 - 6} \right) \frac{\sigma}{16} \\ \left( \frac{z_{2s}^2 - 1}{z_{2s}^2 - 6} \right) \frac{\sigma}{8} \\ \frac{\sigma}{8} \end{array} \right\}. \quad (158)$$

The first two listed eigenvalues are doubly degenerate, and the last value is nondegenerate. The five eigenvalues sum to zero as expected.

Next consider the special case of high-order overtones ( $s \gg 1$ ) for which  $z_{2s} \gg 1$ . In this case it is evident that both  $Z$  and  $\hat{Z}$  approach unity. The  $\mathbf{B}$  matrix simplifies to

$$\mathbf{B}^{2s} = \frac{1}{16} \begin{bmatrix} -3\sigma & 5\gamma & 0 & 0 & 0 \\ 5\gamma & 2\sigma & 0 & 0 & 0 \\ 0 & 0 & 2\sigma & 0 & 0 \\ 0 & 0 & 0 & 2\sigma & -5\gamma \\ 0 & 0 & 0 & -5\gamma & -3\sigma \end{bmatrix}. \quad (159)$$

Interestingly, this matrix also has only three unique eigenvalues:

$$\Lambda^{2s} = \left\{ \begin{array}{c} -\frac{1}{32}(\sigma + 5\sqrt{\sigma^2 + \gamma^2}) \\ -\frac{1}{32}(\sigma - 5\sqrt{\sigma^2 + \gamma^2}) \\ \frac{\sigma}{8} \end{array} \right\} \quad (160)$$

where the first two values are doubly degenerate and the last value is nondegenerate. Now if  $\gamma$  is zero in this large  $s$  example, the number of unique eigenvalues is further reduced to two. This is clearly seen in equation (159). The values are:

$$\Lambda^{2s} = \left\{ \begin{array}{c} -\frac{3\sigma}{16} \\ \frac{\sigma}{8} \end{array} \right\} \quad (161)$$

where the first value is doubly degenerate and the second value is triply degenerate.

Next consider the case  $\sigma = 0$  for which there may still be a lateral offset ( $\gamma \neq 0$ ).  $\mathbf{B}^{2s}$  reduces to the off-diagonal matrix

$$\mathbf{B}^{2s} = \frac{5\hat{Z}}{112} \begin{bmatrix} 0 & (6+Z)\gamma & 0 & 0 & 0 \\ (6+Z)\gamma & 0 & -3\sqrt{6}(Z-1)\gamma & 0 & 0 \\ 0 & -3\sqrt{6}(Z-1)\gamma & 0 & 3\sqrt{6}(Z-1)\gamma & 0 \\ 0 & 0 & 3\sqrt{6}(Z-1)\gamma & 0 & -(6+Z)\gamma \\ 0 & 0 & 0 & -((6+Z))\gamma & 0 \end{bmatrix}. \quad (162)$$

The five distinct eigenvalues of this matrix are

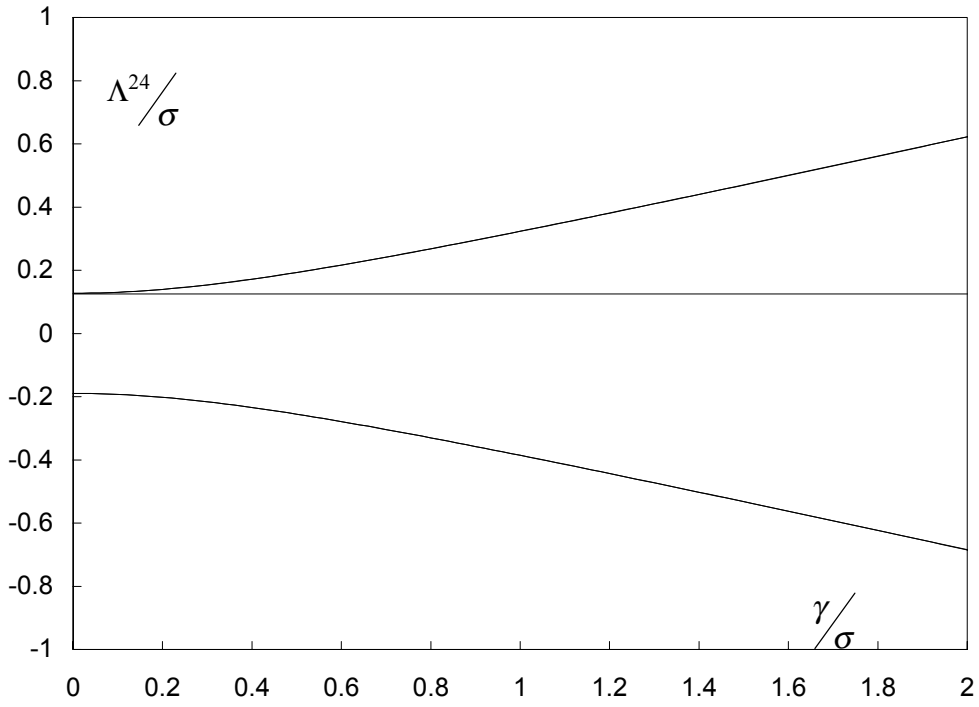
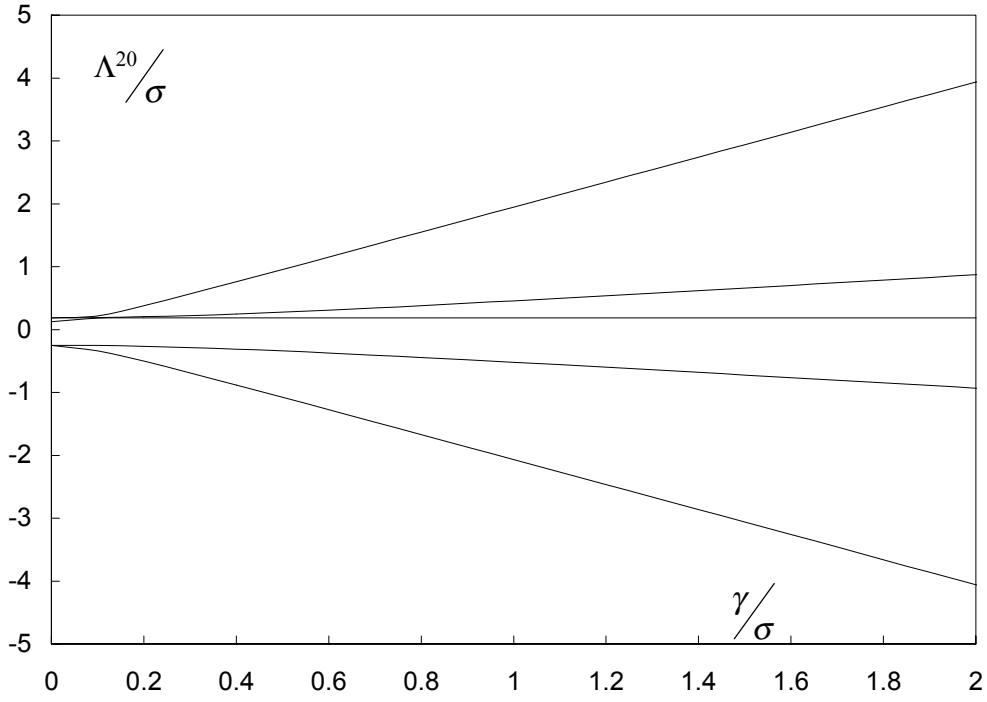
$$\Lambda^{2s} = \left\{ \begin{array}{c} 0 \\ \pm \frac{5\hat{Z}}{112} (Z+6)\gamma \\ \pm \frac{5\hat{Z}}{112} \gamma \sqrt{109Z^2 - 204Z + 144} \end{array} \right\}. \quad (163)$$

And for the limit of large overtone-number, the number of distinct eigenvalues is reduced to three:

$$\Lambda^{2s} = \left\{ \begin{array}{c} 0 \\ \pm \frac{\gamma}{16} \end{array} \right\}. \quad (164)$$

Consider the general case eigenvalues of  $\mathbf{B}^{20}$  and  $\mathbf{B}^{24}$  for the model deformation. The following graphs show the eigenvalues for various values of  $\gamma/\sigma$ . For the fundamental matrix  $\mathbf{B}^{20}$ , notice the partial degeneracy breaking for  $\gamma = 0$  and the complete degeneracy breaking at all nonzero values for  $\gamma$ . For the overtone matrix  $\mathbf{B}^{24}$  the  $Z$ -functions are beginning to approach unity:  $Z = 1.024351$  and  $\hat{Z} = 1.010546$ . The following graph demonstrates that even for this moderate value of  $s$ , the highest and lowest eigenfrequencies are virtually degenerate – the extremal lines are actually two lines that are not separately resolvable at this scale. The constant eigenvalue ( $\sigma/8$ ) remains

nondegenerate. Notice also that the eigenvalues for the overtone matrix are significantly reduced compared to those for the fundamental matrix.



The model perturbation developed in this section along with the matrix construction information in Appendices G and H are sufficient for examining specific properties of eigenvalues up to order  $\ell = 6$ . Such an analysis becomes increasingly complex and is not pursued further here. However, the following summary should suffice to encompass the important properties of the effects of the model perturbation on the eigenfrequencies of a spherical cavity.

1. Two hemishells of different but nearly equal radii (described by the parameter  $\beta$ ) yield a cavity shape perturbation that has no effect on the degenerate cavity resonances.
2. In the general case of nonzero elongation ( $\sigma$ ) and lateral offset ( $\gamma$ ) parameters, the cavity shape is such that the degeneracy breaking of each resonance is complete. Each resonance  $f_{\ell s}$  is split into the  $2\ell + 1$  resonances  $\tilde{f}_{\ell ms}$ .
3. Any single resonance group  $\tilde{f}_{\ell ms}$  is sufficient for determining  $\sigma$  and  $\gamma$  provided that there are no other cavity perturbations except those described by this model.
4. In the absence of a lateral offset ( $\sigma \neq 0, \gamma = 0$ ) the number of independent eigenfrequencies is reduced to  $\ell + 1$ . This is a special case of the general axisymmetric treatment given in section V.
5. In the absence of an elongation defect ( $\sigma = 0, \gamma \neq 0$ ) the number of independent eigenfrequencies is the full  $2\ell + 1$ . However the eigenvalues are symmetric about zero as seen in equations (155) and (163).
6. For moderate to large values of  $s$  (higher overtone frequencies) many eigenvalues are nearly degenerate. In general ( $\sigma \neq 0, \gamma \neq 0$ ) the unique eigenfrequencies are effectively reduced in number to  $\ell + 1$  as is the case for axisymmetric perturbations (see #4 above). For the special cases described above in #4 and #5, the effective numbers of eigenvalues are reduced to  $\ell$  and  $\ell + 1$ , respectively.

## V. MODEL DEFORMATION #2 – AXISYMMETRIC DEFORMATION

This section develops the eigenfrequency calculation for purely axisymmetric deformations. Except for the possibility of a specially machined cavity, an axisymmetric description is unlikely to reflect a strict reality in most cases. However, this model is pursued here for two important reasons. First, the calculations are greatly simplified and are readily extended relative to the more general cases discussed thus far. It becomes important then to understand to what extent an axisymmetric description can be used to characterize a nonaxisymmetric cavity. Second, solid hydrogen fuel layers within spherical ICF cavities will tend to a strongly axisymmetric distribution due to axially symmetric mounting structures.

### A. Eigenfrequency Calculation

The necessary theoretical framework for describing the eigenfrequencies of cavities with purely axisymmetric deformations has been developed in Section III. And some special cases have been examined with regard to hemishell construction in Section IV. However, the full axisymmetric case is now discussed in the present section.

The axisymmetric conditions for the  $\mathbf{B}$  matrix, equation (106), are  $q = 0; m = m'$  which lead to the result:

$$\mathbf{B}_{mm}^{\ell s} = \sum_{\substack{p=2 \\ \text{even}}}^{2\ell} K_{\ell ps} \tilde{C}(\ell p \ell; m 0 m) c_{p0} . \quad (165)$$

As before, the  $c_{p0}$  are the deformation coefficients defined in equation (84), the  $K_{\ell ps}$  are numerical factors given by equation (107), and the  $\tilde{C}$  are defined in equation (103) and are tabulated in appendix G as the  $m = m'$  entries. The imposed symmetry is such that  $\mathbf{B}$  is diagonal and symmetric about  $m \rightarrow -m$ . Thus, in general, the eigenvalues of  $\mathbf{B}$ ,  $\Lambda_m^{\ell s}$ , are the diagonal elements of which there are  $\ell + 1$  independent values. The discussions of hemishell construction deformations for which  $\gamma = 0$  (section IV) are special cases of



equation (165). The full numerical eigenvalues and various approximations are tabulated in Appendix H for  $\ell \leq 6$ .

The degeneracy of eigenvalues is only partially broken from the exact spherical case. The number of independent eigenvalues is  $\ell + 1$ . One eigenvalue is nondegenerate and the remainder are doubly degenerate. This specific partial breaking is unique among general deformation classifications.

The numerical coefficients used in calculating the eigenvalues are typically of order unity or somewhat smaller for the case of fundamental resonances ( $s = 0$ ). A notable exception is the identically zero value found in the expression for  $\Lambda_{\pm 1}^{20}$ . This implies that for each eigenvalue set  $\Lambda^{\ell 0}$  the relevant deformation coefficients  $c_{p0}$  ( $p \leq 2\ell$ ) will have roughly equal computational contributions. A closer examination reveals that at higher  $\ell$  values the contributions are diluted for the larger values of  $p$  for some eigenvalues. For example, the nondegenerate eigenvalues are relatively unaltered by the higher order  $p$  contributions.

## B. A First Method for Computing Deformation Coefficients

Eigenvalue expressions that combine linearity with increasing complexity in  $\ell$  allow the calculation of deformation coefficients from a set of eigenfrequencies. This section describes one such backward-calculation procedure.

Assume that a set of resonant frequency groups  $\mathbf{F}_L$  is obtained by experiment

$$\mathbf{F}_L \equiv \left\{ \left\{ f_{1s_1} \right\}, \left\{ f_{2s_2} \right\}, \dots, \left\{ f_{Ls_L} \right\} \right\}. \quad (166)$$

Consider some specific properties of  $\mathbf{F}_L$ . First, each frequency group consists of  $\ell + 1$  independent values. The degeneracy of each individual frequency need not be known. (Recall that for each set one frequency is nondegenerate and the remainder are doubly degenerate.) Second, only a single  $s$  value is required for each  $\ell$  mode, and each  $s$  value

is independent of the others. Choosing  $s_1 = s_2 = \dots = s_L = 0$  is not necessary but may prove easiest in practice. Third, the set of frequency groups must be sequential from  $\ell = 1$  up to some terminating value  $\ell = L \geq 2$ . The set  $\mathbf{F}_L$  uniquely determines (aside from mathematical accident) the deformation coefficient set  $\mathbf{C}_P$  given by

$$\mathbf{C}_P \equiv \{c/a; c_{20}, c_{40}, \dots, c_{P0}\} \quad (167)$$

where  $P = 2L$ . The ratio  $c/a$  determines *all* the unperturbed resonance frequencies according to equation (30). The procedure for computing these values follows. The  $s$ -value subscripts have been omitted for clarity.

Step 1. Compute the two possible solutions for  $\mathbf{C}_2$  given the lowest order frequency set  $\mathbf{F}_1$ . The set  $\{f_1\}$  consists of two frequencies, say  $f_1^{(1)}$  and  $f_1^{(2)}$ . By assumption the degeneracies of these frequencies are unknown except for the fact that one must be doubly degenerate and one must be nondegenerate. Thus the average frequency (which determines the ratio  $c/a$ ) can be either of two values  $(2f_1^{(1)} + f_1^{(2)})/3$  or  $(f_1^{(1)} + 2f_1^{(2)})/3$ . The coefficient  $c_{20}$  is then computed in each case according to equation (165) or equivalently equation (H12). Thus far these two possible solutions are equally valid.

Step 2. The set  $\{f_2\}$  consists of three frequencies, say  $f_2^{(1)}$ ,  $f_2^{(2)}$  and  $f_2^{(3)}$ . The average frequency, however, can only take on one of two possible values corresponding to the  $c/a$  ratios found in step 1. This constraint is sufficient for determining the specific degeneracies of the three frequencies given that two must be doubly degenerate and the third nondegenerate. Once  $c/a$  is determined so is the corresponding value of  $c_{20}$ . Finally,  $c_{40}$  is computed according to equation (165) or equation (H13).

Step 3. The average frequency for the set  $\{f_3\}$  is already determined by equation (30). Thus, the coefficient  $c_{60}$  is now uniquely determined by equation (165) or equation (H14).

Step 4. Repeat step 3 stepwise in  $\ell$  until the full set  $\mathbf{C}_P$  is obtained.

From a theoretical standpoint, this procedure is straightforward and computationally simple even considering the restrictions and requirements placed on the data. In practice its usefulness may be limited by any of several factors: experimental uncertainties; frequency shifts due to dissipative mechanisms; soft boundary effects; accidentally degenerate values; etc.

### C. A Second Method for Computing Deformation Coefficients

A second method for computing  $\mathbf{C}_p$  is now presented. The required data set  $\tilde{\mathbf{F}}_L$  is given by

$$\tilde{\mathbf{F}}_L \equiv \{c/a; f_1^{\min}, f_1^{\max}; f_2^{\min}, f_2^{\max}; \dots; f_L^{\min}, f_L^{\max}\} \quad (168)$$

where the s-value subscripts have been omitted for clarity but follow the same requirements given for equation (166). Regardless of the  $\ell$ -value of a frequency set, the required data are simply the minimum and maximum frequencies. In each case the extremal frequencies represent a subset of the  $\ell + 1$  possible values. In addition, the ratio  $c/a$  is now known. The procedure for obtaining  $\mathbf{C}_p$  is described below.

Step 1. The first coefficient  $c_{20}$  is uniquely determined by the first extremal frequency set and  $c/a$ . The extremal frequency subset for this  $\ell = 1$  case is the full frequency set of  $\ell + 1 = 2$  values.

Step 2. Compute  $c_{40}$  from the extremal set  $\{f_2^{\min}, f_2^{\max}\}$ , the known  $c/a$  and the calculated value  $c_{20}$  using equation (166) or equation (H13). This calculation is noninvertible in the sense that it is not known *a priori* which of the three eigenfrequencies, say in equation (H13), will be the extremal two. Thus, the value of  $c_{40}$  which fits the data is sought rather than computed. In general the solution is unique.

Step 3. Repeat step 2 stepwise in  $\ell$  until the full set  $\mathbf{C}_p$  is obtained.

Clearly, this second method is relatively computationally intensive because the deformation coefficient values must be sought through a least-squares fitting routine (or

other routine of choice). However, a great advantage to this second approach is the simplified data set. In an experimental setting it may not always be easy to obtain all  $\ell + 1$  frequency values in a given set because of accidental or effective degeneracy. The extremal values of a set, however, are readily apparent and accurately determined. The drawback of this second method is that  $c/a$  may not be known with sufficient accuracy (or at all). This difficulty is explored further in section VII.

## VI. DISSIPATIVE EFFECTS

This section extends the acoustic resonance calculations of Section I to include the effects of several nonideal properties of the fluid and enclosing shell. These effects manifest themselves as spectral frequency shifts and peak broadening. An understanding of these effects is important for accurately determining derived fluid and shell properties.

This section is organized as follows. The acoustic admittance of a resonator boundary is presented in terms of a generalized spherical boundary condition. Next, spherical acoustic wave equations are presented which include viscous and thermal properties of the fluid. The resonator boundary conditions are then investigated and the thermal and viscous acoustic admittance is determined. The enclosing shell is then considered as a compliant boundary providing an additional contribution to the acoustic admittance. These effects are considered as additive, and their relative contributions are examined for several inertial fusion applications. The theoretical development largely follows that of Moldover *et al.* (1986) and draws upon the works of several others cited in the text.

### A. Boundary Condition Formalism

Consider a perfectly spherical cavity filled with a real fluid. To account for nonideal boundary effects, assume that in steady-state oscillations all small quantities vary sinusoidal in time. Further, suppose that each quantity can be written in terms of the familiar velocity potential. Then the Helmholtz equation, equation (20), still holds true, but the boundary condition, equation (27), does not. The velocity potential at the boundary can show a complicated behavior that depends on the physical properties of the fluid as well as the bounding medium. It is convenient to write a new boundary condition in terms of a specific acoustic admittance  $\beta(\omega)$ :

$$\left. \frac{\partial \psi_{\ell m}}{\partial r} \right|_{r=a} = (-i\omega/c)\beta(\omega)\psi_{\ell m}(a) \quad (169)$$

where the units are chosen so that  $\beta$  is dimensionless. The complex prefactor  $i \equiv \sqrt{-1}$  is chosen so that the real part of  $\beta$  corresponds to energy dissipation and resonance broadening and that the imaginary part of  $\beta$  corresponds to resonance shifts. It is easily verified using equations (6) and (7) that

$$\beta(\omega) = (\rho_0 c / p') \vec{v} \cdot \hat{r} \big|_{r=a}. \quad (170)$$

The solution to equation (169) immediately follows upon substitution of equation (22a):

$$\frac{ka j'_\ell(ka)}{j_\ell(ka)} = (-i\omega a/c)\beta(\omega). \quad (171)$$

For the ideal resonator case of Section IA (rigid insulating boundary) the specific admittance is  $\beta = 0$ , and equation (28) is recovered from equation (171).

## B. Wave Equation for a Viscous Compressible Fluid

This section outlines a derivation of the fourth-order differential equation governing the acoustic temperature distribution in a viscous fluid. The derivation itself may not be particularly enlightening (Kirchhoff first achieved the result in 1868), but it does serve as an avenue for introducing and discussing important physical constants.

Three equations are useful for the derivation. The first is the equation of continuity introduced as equation (9) in section II:

$$\rho_0 (\vec{\nabla} \cdot \vec{v}') + \frac{\partial \rho'}{\partial t} = 0. \quad (9)$$

This equation describes conservation of mass in terms of acoustic density and velocity changes.

The second equation describes the conservation of energy. Let the temperature  $T = T_0 + T'$  where  $T_0$  is the ambient temperature and  $T'$  is the small acoustic temperature change. Then

$$T_0 \rho_0 \frac{\partial s'}{\partial t} = K \nabla^2 T'. \quad (172)$$

The proportionality constant  $K$  is the coefficient of thermal conductivity of the fluid.

The third equation is the linear viscous-fluid generalization of equation (1) in the absence of external forces. It describes the conservation of momentum. It is written compactly as

$$\rho_0 \frac{d\vec{v}'}{dt} = -\bar{\nabla} P' + \eta \nabla^2 \vec{v}' + (\eta/3 + \eta_b) \bar{\nabla} (\bar{\nabla} \cdot \vec{v}'). \quad (173)$$

In this equation  $\eta$  is the shear viscosity and  $\eta_b$  is the bulk viscosity of the fluid. The viscosity coefficients are phenomenological constants describing a fluid's ability to resist shear and other mechanisms by which momentum is transferred across a plane tangent to the velocity. The bulk viscosity is often related to molecular relaxation in compressible flow.

Equations (172) and (173) are not derived here in the interest of space. Excellent derivations are found in a number of texts, including Fetter and Walecka (1980). The following derivation of the temperature distribution equation is straightforward although it is somewhat involved. Equations (172) and (173) are subjected to various variable manipulations until both are written in terms of the independent variables  $\rho'$  and  $T'$ . Then  $\rho'$  is eliminated between them and the desired equation is the result. Beginning with equation (173), note that

$$\nabla^2 \vec{v}' = \bar{\nabla} (\bar{\nabla} \cdot \vec{v}') - \bar{\nabla} \times (\bar{\nabla} \times \vec{v}'). \quad (174)$$

But the cross-product term vanishes identically for potential flow. Furthermore, taking  $\bar{\nabla} \cdot (173)$ , using equation (9) to substitute density for velocity, and invoking harmonic time dependence ( $e^{i\omega t}$ ) for all acoustic variables yields the result

$$\omega^2 \rho' + \bar{\nabla}^2 P' + \frac{i\omega}{\rho_0} \left( \frac{4}{3} \eta + \eta_b \right) \bar{\nabla}^2 \rho' = 0. \quad (175)$$

Next, a series of thermodynamic manipulations will enable the pressure  $P'$  to be written in terms of the density and temperature. Specifically, with density and temperature as independent variables, the full differential of the pressure is

$$dP = \left( \frac{\partial P}{\partial \rho} \right)_T d\rho + \left( \frac{\partial P}{\partial T} \right)_\rho dT. \quad (176)$$

The remaining steps in analyzing this differential are simply listed without discussion in the sequence below. The thermodynamic relations are given in Appendix L.

$$\begin{aligned} dP &= \frac{c^2}{\bar{\gamma}} d\rho + \left( \frac{\partial P}{\partial T} \right)_V dT \\ dP &= \frac{c^2}{\bar{\gamma}} d\rho + \frac{-(\partial V / \partial T)_P}{(\partial V / \partial P)_T} dT \\ dP &= \frac{c^2}{\bar{\gamma}} d\rho + \frac{-\alpha_T V}{-\kappa_T V} dT \\ dP &= \frac{c^2}{\bar{\gamma}} d\rho + \frac{\alpha_T \rho c^2}{\bar{\gamma}} dT. \end{aligned} \quad (177)$$

In these equations  $c$  is the adiabatic sound speed,  $\alpha_T$  is the thermal expansion coefficient,  $\kappa_T$  is the isothermal compressibility, and  $\bar{\gamma}$  is the ratio of specific heats  $C_P / C_V$ . From equation (177) it follows that the linear acoustic approximation for  $\bar{\nabla}^2 P'$  is

$$\bar{\nabla}^2 P' = \frac{c^2}{\bar{\gamma}} \bar{\nabla}^2 \rho' + \frac{\alpha_T \rho_0 c^2}{\bar{\gamma}} \bar{\nabla}^2 T', \quad (178)$$

and substitution into equation (175) yields the important intermediate result

$$\omega^2 \rho' + \left[ \frac{c^2}{\bar{\gamma}} + \frac{i\omega}{\rho_0} \left( \frac{4}{3} \eta + \eta_b \right) \right] \bar{\nabla}^2 \rho' + \frac{\alpha_T \rho_0 c^2}{\bar{\gamma}} \bar{\nabla}^2 T' = 0. \quad (179)$$



This equation is the first of two that describe the relation between the temperature and density of a viscous fluid undergoing harmonic oscillations. To obtain the second equation, write the entropy as a function of density and temperature and substitute into equation (172). Once again, the thermodynamic derivation is listed here with the specific relations given in Appendix L.

$$ds = \left( \frac{\partial s}{\partial \rho} \right)_T d\rho + \left( \frac{\partial s}{\partial T} \right)_\rho dT \quad (180)$$

$$ds = \frac{-V}{\rho} \left( \frac{\partial s}{\partial V} \right)_T d\rho + \left( \frac{\partial s}{\partial T} \right)_V dT$$

$$ds = \frac{-V}{\rho} \left( \frac{\partial P}{\partial T} \right)_V d\rho + \frac{C_V}{T} dT$$

$$ds = \frac{-V}{\rho} \frac{\alpha_T \rho c^2}{\bar{\gamma}} d\rho + \frac{C_P}{\bar{\gamma} T} dT$$

$$ds = -\frac{\alpha_T V c^2}{\bar{\gamma}} d\rho + \frac{C_P}{\bar{\gamma} T} dT. \quad (181)$$

The acoustic time derivative  $\partial s'/\partial t$  can be calculated with equation (181). Keeping only terms linear in the acoustic quantities and invoking harmonic time dependence, it is readily found that

$$i\omega s' = -\frac{i\omega \alpha_T V c^2}{\bar{\gamma}} \rho' + \frac{i\omega C_P}{\bar{\gamma} T_0} T'. \quad (182)$$

Now substituting equation (182) into equation (172), the second equation relating the acoustic temperature and pressure is readily found:

$$-\frac{i\omega \alpha_T V c^2}{\bar{\gamma}} \rho' + \frac{i\omega C_P}{\bar{\gamma} T_0} T' - \frac{K}{T_0 \rho_0} \bar{\nabla}^2 T' = 0. \quad (182)$$

This equation is not used to eliminate the variable  $\rho'$  from equation (179). First note that (from Appendix L):

$$\alpha_T V c^2 T_0 = \frac{(\bar{\gamma} - 1) C_P}{\alpha_T \rho_0}, \quad (183)$$

so that equation (182) can be written somewhat more simply as

$$-i\omega C_P (\bar{\gamma} - 1) \rho' + i\omega \alpha_T \rho_0 C_P T' - \alpha_T \bar{\gamma} K \bar{\nabla}^2 T' = 0 \quad (184)$$

or, more to the present purpose as

$$\rho' = \frac{\alpha_T \rho_0}{(\bar{\gamma} - 1)} T' + \frac{i\alpha_T \bar{\gamma} K}{\omega C_P (\bar{\gamma} - 1)} \bar{\nabla}^2 T' \quad (185)$$

and by inference

$$\bar{\nabla}^2 \rho' = \frac{\alpha_T \rho_0}{(\bar{\gamma} - 1)} \bar{\nabla}^2 T' + \frac{i\alpha_T \bar{\gamma} K}{\omega C_P (\bar{\gamma} - 1)} \bar{\nabla}^4 T'. \quad (186)$$

Finally, using equations (185) and (186) the density terms can be eliminated in equation (179). The quick substitution result is

$$\begin{aligned} & \frac{\omega^2 \alpha_T \rho_0}{(\bar{\gamma} - 1)} T' + \frac{i\omega \alpha_T \bar{\gamma} K}{C_P (\bar{\gamma} - 1)} \bar{\nabla}^2 T' \\ & + \left[ \frac{c^2}{\bar{\gamma}} + \frac{i\omega}{\rho_0} \left( \frac{4}{3} \eta + \eta_b \right) \right] \left[ \frac{\alpha_T \rho_0}{(\bar{\gamma} - 1)} \bar{\nabla}^2 T' + \frac{i\alpha_T \bar{\gamma} K}{\omega C_P (\bar{\gamma} - 1)} \bar{\nabla}^4 T' \right] \\ & + \frac{\alpha_T \rho_0 c^2}{\bar{\gamma}} \bar{\nabla}^2 T' = 0. \end{aligned} \quad (187)$$

Now, gathering terms common in  $T'$  derivatives and multiplying through by the constant term  $(\bar{\gamma} - 1)/\alpha_T \rho_0 c^2$ , this equation is simplified somewhat to

$$\begin{aligned}
& \frac{iK}{\omega\rho_0 C_P} \left[ 1 + \frac{i\omega\bar{\gamma}}{\rho_0 c^2} \left( \frac{4}{3}\eta + \eta_b \right) \right] \bar{\nabla}^4 T' \\
& + \left[ 1 + \frac{i\omega\bar{\gamma}K}{\rho_0 c^2 C_P} + \frac{i\omega}{\rho_0 c^2} \left( \frac{4}{3}\eta + \eta_b \right) \right] \bar{\nabla}^2 T' \\
& + \frac{\omega^2}{c^2} T' = 0.
\end{aligned} \tag{188}$$

The form and solutions of equation (188) are considerably simplified through the use of the characteristic viscous and thermal penetration lengths given by

$$\delta_v \equiv \sqrt{\frac{2}{\omega} \left( \frac{4\eta}{3\rho_0} + \frac{\eta_b}{\rho_0} \right)}, \text{ and} \tag{189}$$

$$\delta_t \equiv \sqrt{\frac{2K}{\omega\rho_0 C_P}}. \tag{190}$$

These penetration lengths represent the distances over which viscous and thermal effects are transmitted within the bulk fluid. Typical values are discussed later in the text, although for derivations in this section, it is assumed that

$$\delta_{v,t} \ll a, \text{ and} \tag{191}$$

$$\frac{\omega\delta_{v,t}}{c} \ll 1. \tag{192}$$

Using the penetration length notation, equation (188) becomes

$$\frac{i\delta_t^2}{2} \left[ 1 + \frac{i\bar{\gamma}\omega^2}{2c^2} \delta_v^2 \right] \bar{\nabla}^4 T' + \left[ 1 + \frac{i\omega^2}{2c^2} (\bar{\gamma}\delta_t^2 + \delta_v^2) \right] \bar{\nabla}^2 T' + \frac{\omega^2}{c^2} T' = 0. \tag{193}$$

This is the equation to be solved through the use of the proper boundary conditions. It is first worth noting that once the temperature solutions are found, the pressure and particle velocity solutions follow readily. For example, equations (177) and (185) reveal that

$$P' = \left( \frac{\alpha_T \rho_0 c^2}{\bar{\gamma} - 1} \right) \left[ 1 + (i\delta_t^2/2) \bar{\nabla}^2 \right] T'. \quad (194)$$

Also, equations (10), (178) and (179) show that

$$\vec{v}' = \frac{i}{\omega \rho_0} \bar{\nabla} \left[ P' + \frac{i\bar{\gamma}}{2} \frac{\omega^2}{c^2} \delta_v^2 \left( P' - \frac{\alpha_T \rho_0 c^2}{\bar{\gamma}} T' \right) \right]. \quad (195)$$

These solutions describe the coupled density and entropy longitudinal acoustic waves due to viscous interaction.

In addition there is a second divergence-free solution  $\vec{w}'$  satisfying the transverse part of equation (173)

$$i\omega \rho_0 \vec{w}' = \eta \bar{\nabla}^2 \vec{w}'. \quad (196)$$

This equation describes purely transverse modes that do not exist in an ideal fluid. This expression is quickly solved. Recasting in the form of the Helmholtz equation,

$$(\bar{\nabla}^2 \bullet k_v^2) \vec{w}' = 0 \quad (197)$$

yields the immediate wavenumber solution

$$k_v^2 = \frac{-i\omega \rho_0}{\eta} = \frac{-2i}{\bar{\delta}_v^2}. \quad (198)$$

The subscript  $v$  on the wavenumber emphasizes the viscous origin of this wave solution.

The new viscous penetration length is defined as

$$\bar{\delta}_v^2 = \frac{2\eta}{\rho\omega}. \quad (199)$$

This shear viscosity penetration length is proportional to the viscous penetration length in the limit of zero bulk viscosity, see equation (189). The transverse velocity field solution for a spherical cavity [Morse and Feshbach (1953) eq. 13.1.6] is

$$\vec{w}' = w_1 \bar{\nabla} \times [\hat{r} r j_\ell(k_v r) Y_{\ell m}(\theta, \phi)] + (w_2/k_v) \bar{\nabla} \times \bar{\nabla} \times [\hat{r} r j_\ell(k_v r) Y_{\ell m}(\theta, \phi)] \quad (200)$$

where  $w_1$  and  $w_2$  are independent constants and  $\hat{r}$  is the radial unit normal vector.

Equation (193) can be written as a bi-quadratic and the solution follows fairly readily.

Consider the fourth-order expression

$$(\bar{\nabla}^4 + 2\chi\bar{\nabla}^2 + \chi^2\xi)T' = 0, \quad (201)$$

where  $\chi$  and  $\xi$  are numeric factors. The bi-quadratic form

$$(\bar{\nabla}^2 + k_t^2)(\bar{\nabla}^2 + k_\rho^2)T' = 0 \quad (202)$$

has solutions

$$k_t^2 = \chi(1 + \sqrt{1 - \xi}) \text{ and} \quad (203)$$

$$k_\rho^2 = \chi(1 - \sqrt{1 - \xi}). \quad (204)$$

By applying this scheme to equation (193) and expanding the results in the small quantities given by equation (192), it is found that

$$k_t^2 = \left( \frac{-2i}{\delta_t^2} \right) \left\{ 1 + \frac{i\omega^2}{2c^2} (\bar{\gamma} - 1)(\delta_t^2 - \delta_v^2) + O\left( \frac{\omega\delta_{t,v}}{c} \right)^4 \right\}, \quad (205)$$

$$k_\rho^2 = \left( \frac{\omega^2}{c^2} \right) \left\{ 1 - \frac{i\omega^2}{2c^2} [(\bar{\gamma} - 1)\delta_t^2 + \delta_v^2] + O\left( \frac{\omega\delta_{t,v}}{c} \right)^4 \right\}. \quad (206)$$

The subscripts  $\rho$  and  $t$  indicate that the two solutions represent the density and entropy wave solutions in the limit of zero viscosity. These expressions will be useful later in this section. The exact spherical cavity solution of equation (193), arrived at from the notation of equation (202), is

$$T' = \{T'_\rho j_\ell(k_\rho r) + T'_t j_\ell(k_t r)\} Y_{\ell m}(\theta, \phi). \quad (207)$$

The pressure follows from equation (194)

$$P' = \left( \frac{\alpha_T \rho_0 c^2}{\bar{\gamma} - 1} \right) \left[ \begin{array}{l} T'_\rho \left[ \begin{array}{l} j_\ell(k_\rho r) - \frac{\delta_t^2}{2i} [j_\ell(k_\rho r) \bar{\nabla}_t^2] \\ - \frac{\delta_t^2}{2i} \left[ k_\rho^2 j_\ell''(k_\rho r) + \frac{2k_\rho}{r} j'_\ell(k_\rho r) \right] \end{array} \right] \\ + T'_t \left[ \begin{array}{l} j_\ell(k_t r) - \frac{\delta_t^2}{2i} [j_\ell(k_t r) \bar{\nabla}_t^2] \\ - \frac{\delta_t^2}{2i} \left[ k_t^2 j_\ell''(k_t r) + \frac{2k_t}{r} j'_\ell(k_t r) \right] \end{array} \right] \end{array} \right] Y_{\ell m}(\theta, \phi). \quad (208)$$

The transverse gradient function includes all of the angular dependence and is formally defined in Appendix A. This equation can be simplified using equations (C22) and (F4)

$$P' = \left( \frac{\alpha_T \rho_0 c^2}{\bar{\gamma} - 1} \right) \left[ \begin{array}{l} T'_\rho \left( 1 + \frac{1}{2i} (\delta_t k_\rho)^2 \right) j_\ell(k_\rho r) \\ + T'_t \left( 1 + \frac{1}{2i} (\delta_t k_t)^2 \right) j_\ell(k_t r) \end{array} \right] Y_{\ell m}(\theta, \phi). \quad (209)$$

The exact velocity expression is cumbersome; it is shown here in terms of the radial and transverse components. These follow directly from equation (195)

$$-i\omega \rho_0 \bar{v}'_r = \left[ 1 + \frac{i\bar{\gamma}}{2} \left( \frac{\omega \delta_v}{c} \right)^2 \right] \frac{\partial P'}{\partial r} \hat{r} - \frac{i\alpha_T \rho_0 c^2}{2} \left( \frac{\omega \delta_v}{c} \right)^2 \frac{\partial T'}{\partial r} \hat{r} \quad (210)$$

$$-i\omega \rho_0 \bar{v}'_t = \left[ 1 + \frac{i\bar{\gamma}}{2} \left( \frac{\omega \delta_v}{c} \right)^2 \right] \bar{\nabla}_t P' - \frac{i\alpha_T \rho_0 c^2}{2} \left( \frac{\omega \delta_v}{c} \right)^2 \bar{\nabla}_t T'. \quad (211)$$

The temperature and pressure derivatives for the velocity calculations are given by

$$\frac{\partial T'}{\partial r} = [T'_\rho k_\rho j'_\ell(k_\rho r) + T'_t k_t j'_\ell(k_t r)] Y_{\ell m}(\theta, \phi) \quad (212)$$

$$\bar{\nabla}_t T' = [T'_\rho j_\ell(k_\rho r) + T'_t j_\ell(k_t r)] \bar{\nabla}_t Y_{\ell m}(\theta, \phi) \quad (213)$$

$$\frac{\partial P'}{\partial r} = \left( \frac{\alpha_T \rho_0 c^2}{\bar{\gamma} - 1} \right) \begin{bmatrix} T'_\rho k_\rho \left( 1 + \frac{\delta_t^2 k_\rho^2}{2i} \right) j'_\ell(k_\rho r) \\ + T'_\rho k_t \left( 1 + \frac{\delta_t^2 k_t^2}{2i} \right) j'_\ell(k_t r) \end{bmatrix} Y_{\ell m}(\theta, \phi) \quad (214)$$

$$\bar{\nabla}_t P' = \left( \frac{\alpha_T \rho_0 c^2}{\bar{\gamma} - 1} \right) \begin{bmatrix} T'_\rho \left( 1 + \frac{\delta_t^2 k_\rho^2}{2i} \right) j_\ell(k_\rho r) \\ + T'_\rho \left( 1 + \frac{\delta_t^2 k_t^2}{2i} \right) j_\ell(k_t r) \end{bmatrix} \bar{\nabla}_t Y_{\ell m}(\theta, \phi). \quad (215)$$

The components of the transverse velocity field, equation (200), can also be constructed.

Using the cross product relations found in Appendix A and equation (C22)

$$\bar{w}'_r = w_2 \ell(\ell+1) \frac{j_\ell(k_v r)}{k_v r} Y_{\ell m}(\theta, \phi) \hat{r} \quad (216)$$

$$\begin{aligned} \bar{w}'_t = w_1 j_\ell(k_v r) \left[ \hat{\theta} \frac{1}{\sin \theta} \frac{\partial}{\partial \phi} - \hat{\phi} \frac{\partial}{\partial \theta} \right] Y_{\ell m}(\theta, \phi) \\ + \frac{w_2}{k_v} [k_v r j'_\ell(k_v r) + j_\ell(k_v r)] \bar{\nabla}_t Y_{\ell m}(\theta, \phi). \end{aligned} \quad (217)$$

The first bracketed term in equation (217) resembles the transverse gradient in form. In fact, it is the transverse gradient followed by a rotation of the coordinate axes about  $\hat{r}$ .

### C. Viscous and Thermal Boundary Effects

The boundary conditions at the fluid/solid interface are now addressed. Solutions, using the velocity, pressure, and temperature equations derived in the preceding subsection, provide expressions for the acoustic admittance of the boundary, the resonant frequency shifts, and resonance widths. The boundary (cavity wall) conditions are three: (1) the temperature and heat flow are continuous; (2) the tangential components of the total

velocity are continuous; and (3) the ratio of the normal component of the velocity to the pressure is equal to the acoustic admittance of the shell.

For typical cavity resonators the temperature continuity condition is very nearly equivalent to requiring that the acoustic temperature variations vanish at the boundary. This is best seen by considering the product  $\rho C_p K$  for both the interior fluid and the surrounding shell. Larger values of specific heat per unit volume and thermal conductivity are characteristic of materials that can absorb and distribute larger amounts of heat with small changes in temperature. Thus  $T'$  at the shell boundary will be very small relative to  $T'$  amplitude values within the thermal boundary layer of the interior fluid provided that

$$\tau \equiv \frac{[\rho C_p K]_{shell}}{[\rho C_p K]_{fluid}} \gg 1. \quad (218)$$

The bracketed quantities are tabulated for various materials in Appendices I and J. In general  $\rho C_p K \sim 10^{14}$  for metals,  $10^{11}$  for solid hydrogens,  $10^{11}$ - $10^{12}$  for liquids,  $10^{10}$ - $10^{11}$  for high-pressure gases, and  $10^7$ - $10^8$  for gases. Thus for all situations of interest  $\tau \sim 10^3$  and equation (218) is satisfied. This first boundary condition then becomes  $T' = 0$ . Equation (207) evaluated at the boundary then shows that

$$\frac{T'_\rho}{T'_t} = -\frac{j_\ell(k_t a)}{j_\ell(k_\rho a)}. \quad (219)$$

The second boundary condition is nearly equivalent to requiring that the total tangential fluid velocities vanish at the shell wall. This is true as long as the shell forms a relatively rigid boundary with respect to the fluid. This condition is

$$\vec{v}'_t + \vec{w}'_t = 0. \quad (220)$$

A quick look at the equations of the previous subsection shows that this expression has one term proportional to  $w_1$  and all other terms proportional to  $\vec{\nabla}_t Y_{\ell m}(\theta, \phi)$ . Thus, the boundary condition is satisfied if  $w_1 = 0$  and



$$w_2 \left[ j'_\ell(k_v a) + \frac{j_\ell(k_v a)}{(k_v a)} \right] = -\frac{i}{a\omega\rho_0} \left[ 1 + \frac{i\bar{\gamma}}{2} \left( \frac{\omega\delta_v}{c} \right)^2 \right] \frac{\bar{\nabla}_t P'}{\bar{\nabla}_t Y_{\ell m}(\theta, \phi)} - \frac{\alpha_T c^2}{2\omega} \left( \frac{\omega\delta_v}{c} \right)^2 \frac{\bar{\nabla}_t T'}{\bar{\nabla}_t Y_{\ell m}(\theta, \phi)}. \quad (221)$$

Using equations (213) and (215) to “simplify” this expression yields

$$w_2 \left[ j'_\ell(k_v a) + \frac{j_\ell(k_v a)}{(k_v a)} \right] = \left( \frac{\alpha_T c^2}{ia\omega(\bar{\gamma} - 1)} \right) \times \left\{ \left[ \left( 1 + \frac{i\bar{\gamma}}{2} \left( \frac{\omega\delta_v}{c} \right)^2 \right) \times \left( 1 + \frac{\delta_t^2 k_\rho^2}{2i} \right) + \frac{\bar{\gamma} - 1}{2i} \left( \frac{\omega\delta_v}{c} \right)^2 \right] T'_\rho j_\ell(k_\rho a) \right. \\ \left. + \left[ \left( 1 + \frac{i\bar{\gamma}}{2} \left( \frac{\omega\delta_v}{c} \right)^2 \right) \times \left( 1 + \frac{\delta_t^2 k_t^2}{2i} \right) + \frac{\bar{\gamma} - 1}{2i} \left( \frac{\omega\delta_v}{c} \right)^2 \right] T'_t j_\ell(k_t a) \right] \right\}. \quad (222)$$

This expression can be simply written as

$$w_2 = \left( \frac{\alpha_T c^2}{ia\omega(\bar{\gamma} - 1)} \right) \frac{G(k_\rho^2) T'_\rho j_\ell(k_v a) + G(k_t^2) T'_t j_\ell(k_t a)}{j'_\ell(k_v a) + j_\ell(k_v a)/(k_v a)}, \quad (223)$$

where

$$G(k^2) \equiv 1 + \frac{i}{2} \left( \frac{\omega\delta_v}{c} \right)^2 - \frac{i}{2} (\delta_t k)^2 + \frac{\bar{\gamma}}{4} \left( \frac{\omega\delta_v \delta_t k}{c} \right)^2. \quad (224)$$

The third boundary condition is

$$\beta_{sh} = \frac{\rho_0 c v_r + \rho_0 c w_r}{P' - \frac{4}{3} \eta \frac{\partial v_r}{\partial r}}, \quad (225)$$

which from the various expressions in this subsection has the following terms:

$$\rho_0 c v_r = \left( \frac{i \alpha_T \rho_0 c^3}{\omega a (\bar{\gamma} - 1)} \right) \left[ G(k_\rho^2) T'_\rho k_\rho a j'_\ell(k_\rho a) + G(k_t^2) T'_t k_t a j'_\ell(k_t a) \right] \bar{\nabla}_t Y_{\ell m}(\theta, \phi) \quad (226)$$

$$\begin{aligned} \rho_0 c w_r = & \left( \frac{i \alpha_T \rho_0 c^3}{\omega a (\bar{\gamma} - 1)} \right) \times \left( \frac{-\ell(\ell+1)}{1 + k_v a j'_\ell(k_v a) / j_\ell(k_v a)} \right) \\ & \times \left[ G(k_\rho^2) T'_\rho j'_\ell(k_\rho a) + G(k_t^2) T'_t j'_\ell(k_t a) \right] \bar{\nabla}_t Y_{\ell m}(\theta, \phi) \end{aligned} \quad (227)$$

$$\begin{aligned} -\frac{4}{3} \eta \frac{\partial v_r}{\partial r} = & \left( \frac{\alpha_T \rho_0 c^2}{\bar{\gamma} - 1} \right) \times \left( \frac{2 \bar{\delta}_v^2}{3i} \right) \\ & \times \left[ G(k_\rho^2) T'_\rho k_\rho^2 j''_\ell(k_\rho a) + G(k_t^2) T'_t k_t^2 j''_\ell(k_t a) \right] \bar{\nabla}_t Y_{\ell m}(\theta, \phi). \end{aligned} \quad (228)$$

The full expression for  $\beta_{sh}$  is quite complicated. However, using equation (219) to eliminate  $T'_\rho$ , equation (F4) to eliminate the  $j''_\ell(ka)$  terms, defining

$$L \equiv \frac{-\ell(\ell+1)}{1 + k_v a j'_\ell(k_v a) / j_\ell(k_v a)}, \text{ and} \quad (229)$$

and dividing through by all common factors, yields the (still bulky) expression

$$\beta_{sh} = \left( \frac{ic}{\omega a} \right) \left[ \frac{G(k_\rho^2) \left( L + \frac{k_\rho a j'_\ell(k_\rho a)}{j_\ell(k_\rho a)} \right) - G(k_t^2) \left( L + \frac{k_t a j'_\ell(k_t a)}{j_\ell(k_t a)} \right)}{\frac{\delta_t^2}{2i} (k_\rho^2 - k_t^2)} \right. \\ \left. + G(k_\rho^2) \left[ -\frac{3 \bar{\delta}_v^2 k_\rho^2}{8i} + \frac{3 \ell(\ell+1) \bar{\delta}_v^2}{8 i a^2} - \frac{\delta_v^2}{i a^2} \frac{k_\rho a j'_\ell(k_\rho a)}{j_\ell(k_\rho a)} \right] \right. \\ \left. - G(k_t^2) \left[ -\frac{3 \bar{\delta}_v^2 k_t^2}{8i} + \frac{3 \ell(\ell+1) \bar{\delta}_v^2}{8 i a^2} - \frac{\delta_v^2}{i a^2} \frac{k_t a j'_\ell(k_t a)}{j_\ell(k_t a)} \right] \right] \quad (230)$$

This exact expression can be approximated to lowest order in the viscous and thermal penetration lengths. The various quantities within equation (230) are given by

$$G(k_\rho^2) = 1 + \frac{i}{2} \left( \frac{\omega \delta_v}{c} \right)^2 - \frac{i}{2} \left( \frac{\omega \delta_t}{c} \right)^2 + O \left( \frac{\omega \delta}{c} \right)^4 \quad (231)$$

$$G(k_t^2) = -\frac{i(\bar{\gamma}-1)}{2} \left( \frac{\omega \delta_t}{c} \right)^2 + O \left( \frac{\omega \delta}{c} \right)^4 \quad (232)$$

$$\frac{k_t a j'_\ell(k_t a)}{j_\ell(k_t a)} = \frac{(1+i)a}{\delta_t} \left[ 1 + \frac{i\omega(\bar{\gamma}-1)}{2c^2} (\delta_t^2 - \delta_v^2) + O \left( \frac{\omega \delta}{c} \right)^2 \right] [1 + O(e^{-2a/\delta})] \quad (233)$$

$$\frac{k_v a j'_\ell(k_v a)}{j_\ell(k_v a)} = \frac{(1+i)a}{\delta_v} [1 + O(e^{-2a/\delta})] \quad (234)$$

$$L = \frac{(i-1)\ell(\ell+1)}{2} \frac{\delta_v}{a} \left[ 1 + \frac{i-1}{2} \frac{\delta_v}{a} + O \left( \frac{\delta}{a} \right)^2 \right] [1 + O(e^{-2a/\delta})]. \quad (235)$$

Substituting these expansions into equation (230) yields the very simple expression

$$\beta_{sh} \approx \left( \frac{ic}{\omega a} \right) \left( \frac{k_\rho a j'_\ell(k_\rho a)}{j_\ell(k_\rho a)} - \frac{1-i}{2} \left[ (\bar{\gamma}-1) \frac{\omega^2 a^2}{c^2} \frac{\delta_t}{a} + \ell(\ell+1) \frac{\bar{\delta}_v}{a} \right] \right). \quad (236)$$

A rearrangement of equation (236) gives the solution to equation (171)

$$\frac{k_\rho a j'_\ell(k_\rho a)}{j_\ell(k_\rho a)} = -i \frac{\omega a}{c} (\beta_{sh} + \beta_t + \beta_v) \quad (237)$$

where the lowest-order thermal and viscous contributions to the acoustic admittance are defined by

$$\beta_t = \frac{1+i}{2} (\bar{\gamma}-1) \frac{\omega a}{c} \frac{\delta_t}{a} + O \left( \frac{\delta_t}{a} \right)^2, \text{ and} \quad (238)$$

$$\beta_v = \frac{1+i}{2} \ell(\ell+1) \frac{c}{\omega a} \frac{\bar{\delta}_v}{a} + O \left( \frac{\bar{\delta}_v}{a} \right)^2. \quad (239)$$

Specific forms for the shell acoustic admittance  $\beta_{sh}$  are examined in subsection D. For the present discussion, consider several limiting cases for  $\beta_{sh}$  and the resulting effects on the complex frequency response.

Case 1. For  $|\beta_{sh}| \gg 1$ , equation (137) approximates to the pressure-release boundary condition

$$j_\ell(k_\rho a) = 0. \quad (240)$$

The roots of the Bessel functions, rather than the roots of the Bessel function derivatives, determine the resonance frequencies. The thermal and viscous contributions need not be considered. They may be small relative to the shell contribution or are also large themselves. Either way, their contributions are negligible. This is also apparent by examining the amplitudes of the thermal wave  $T'_t$  in equation (219) and the viscosity-induced transverse wave  $w_2$  in equation (222) which are both proportional to  $j_\ell(k_\rho a)$ . Many of the lowest-order solutions to equation (240) are given in Appendix D. The shell admittance may be large if the interior fluid is very dense, having a total mass comparable to that of the shell. This is often the case with liquids and high-pressure gases contained in a thin-walled cavity. The shell admittance can also be large when a fluid mode resonance frequency nearly coincides with a resonance frequency of the shell. These possibilities are considered in section D on compliant boundary effects.

Case 2. Consider the case for which all of the admittances in equation (237) are small, producing only small corrections to the resonance frequencies. Specifically, consider the limitation  $\beta \ll ka$ . In this case let

$$k_\rho = k_0 + \Delta k \quad (241)$$

where  $k_0$  is the wavenumber solution in the absence of viscous and thermal effects. That is

$$\frac{j'_\ell(k_0 a)}{j_\ell(k_0 a)} = -i\beta_{sh} \quad (242)$$

and  $\Delta k$  is a small wavenumber correction to  $k_0$ . An expression in  $k_0$  is sought using equation (237). Some additional useful expansions are provided by equations (F1) and (F4)

$$j_\ell(k_\rho a) = j_\ell(k_0 a) + j'_\ell(k_0 a)\Delta k a + O(\Delta k a)^2 \quad (243)$$

$$j'_\ell(k_\rho a) = j'_\ell(k_0 a) + j''_\ell(k_0 a)\Delta k a + O(\Delta k a)^2 \quad (244)$$

$$j''_\ell(k_0 a) = -\frac{2}{k_0 a} j'_\ell(k_0 a) - \left[ 1 - \frac{\ell(\ell+1)}{(k_0 a)^2} \right] j_\ell(k_0 a). \quad (245)$$

With these expressions, it is found that, correct to order  $(\Delta k a)$

$$\Delta k a = \frac{i(\beta_t + \beta_v)}{\left[ 1 - \frac{\ell(\ell+1)}{(k_0 a)^2} \right] - \frac{2i}{k_0 a} \beta_{sh} - \beta_{sh}^2}. \quad (246)$$

As expected  $\Delta k a$  vanishes in the absence of thermal and viscous effects. The change in the complex frequency  $F$  can be written as a sum of a real frequency shift  $\Delta f$  and dissipative broadening  $g$ . That is

$$\frac{\Delta F}{f} = \frac{\Delta f + ig}{f} = \frac{\Delta k a}{k_0 a} + \frac{ig_b}{f} \quad (247)$$

where  $g_b$  is the dissipation due to bulk properties of the fluid. This quantity can be found in various acoustics texts or can be computed directly from equation (206) as

$$g_b = \frac{\pi^2 f^3}{c^2} [(\bar{\gamma} - 1)\delta_t^2 + \delta_v^2]. \quad (248)$$

In equations (247) and (248) the frequency  $f$  is taken to be the forcing frequency or free decay frequency for resonant oscillations. This first-order approximation is sufficient for considering the small correction quantities of interest.

Case 3. Finally, consider the rigid boundary limits:  $\beta_{sh} \rightarrow 0$  and  $k_0 a \rightarrow z_{\ell s}$ . From equation (246) it is readily found that

$$\frac{\Delta k a}{k_0 a} = \frac{i(\beta_t + \beta_v)}{[1 - \ell(\ell + 1)/z_{\ell s}^2]} = -\frac{1 - i}{2a} \frac{[(\bar{\gamma} - 1)\delta_t + \ell(\ell + 1)\bar{\delta}_v/z_{\ell s}^2]}{[1 - \ell(\ell + 1)/z_{\ell s}^2]}. \quad (249)$$

And so the change in the complex frequency according to equation (247) is

$$\frac{\Delta F_{\ell s}}{f_{\ell s}} = i \left( \frac{\pi f_{\ell s}}{c} \right)^2 [(\bar{\gamma} - 1)\delta_t^2 + \delta_v^2] + \frac{i - 1}{2a} \frac{[(\bar{\gamma} - 1)\delta_t + \ell(\ell + 1)\bar{\delta}_v/z_{\ell s}^2]}{[1 - \ell(\ell + 1)/z_{\ell s}^2]}. \quad (250)$$

The first term is the bulk dissipation of equation (248). The second term shows that the boundary effects contribute equally to the real and imaginary frequency shifts.

#### D. Compliant Boundary Effects

Mehl (1985) has calculated the acoustic admittance of a fluid-filled spherical shell of isotropic material. The analysis is exact taking into account the resonant responses of the shell as well as the fluid. The admittance is shown to diverge at resonances of the shell and is shown to be independent of the index  $m$ . The equations and results are not reproduced here; instead, a different and more general approach is explored.

Alterman *et al.* (1959) adapted the elastic equations of motion for an isotropic solid/fluid of Love (1944) to account for self-gravitation and radial dependence in the material properties. Specifically,

$$\rho = \rho(r), \quad (251)$$

$$\lambda = \lambda(r), \quad (252)$$

$$\mu = \mu(r). \quad (253)$$

The two independent elastic moduli for an isotropic solid are represented by the Lamé constants  $\mu$  and  $\lambda$ . In standard crystallographic notation  $c_{11} = \lambda + 2\mu$  and  $c_{44} = \mu$ . The longitudinal and shear (transverse) sound speeds of an isotropic solid are given by

$$c_L = \sqrt{(\lambda + 2\mu)/\rho} , \quad (254)$$

$$c_S = \sqrt{\mu/\rho} . \quad (255)$$

Equations (251) to (253) guarantee that any such described object has complete spherical symmetry. The radial dependence of the functions is arbitrary and thus may include solids, fluids, and property discontinuities. The full derivation of Alterman's equations is not given here but can be arrived at from the discussions of Love (1944) [see for example sections 22, 59, and 96]. If the gravitation terms are omitted the equations of torsional motion are

$$\frac{dy_1}{dr} = \frac{1}{r} y_1 + \frac{1}{\mu} y_2 \quad (256)$$

$$\frac{dy_2}{dr} = \left[ \frac{\mu(\ell-1)(\ell+2)}{r^2} - \rho_0 \omega^2 \right] y_1 - \frac{3}{r} y_2 \quad (257)$$

where  $y_1$  is the amplitude of the shear motion and  $y_2$  is proportional to the radial shear stress. The boundary conditions are (1) the shear stress  $y_2$  must vanish at all solid/fluid and solid/vacuum boundaries and (2) the displacement  $y_1$  is continuous across all solid boundaries. In the case of a single solid shell (with or without an interior fill)  $y_2$  vanishes at both inner and outer radii  $a$  and  $b$ . Fluids do not support this class of motion, and in this model any fluids have no effect on the calculations. These modes can be useful for the interpretation of cryogenic phase data as described in Section VII.

The equations of spheroidal motion are (again omitting gravitational terms)

$$\frac{dy_1}{dr} = \frac{2\lambda}{(\lambda + 2\mu)r} y_1 + \frac{1}{(\lambda + 2\mu)} y_2 + \frac{\lambda\ell(\ell+1)}{(\lambda + 2\mu)} y_3 \quad (258)$$

$$\begin{aligned} \frac{dy_2}{dr} = & \left[ \frac{4\mu(3\lambda + 2\mu)}{r^2(\lambda + 2\mu)} - \rho_0\omega^2 \right] y_1 - \frac{4\mu}{r(\lambda + 2\mu)} y_2 \\ & - \frac{2\mu\ell(\ell + 1)(3\lambda + 2\mu)}{r^2(\lambda + 2\mu)} y_3 + \frac{\ell(\ell + 1)}{r} y_4 \end{aligned} \quad (259)$$

$$\frac{dy_3}{dr} = -\frac{1}{r} y_1 + \frac{1}{r} y_2 + \frac{1}{\mu} y_4 \quad (260)$$

$$\begin{aligned} \frac{dy_4}{dr} = & -\frac{2\mu(3\lambda + 2\mu)}{r^2(\lambda + 2\mu)} y_1 - \frac{\lambda}{r(\lambda + 2\mu)} y_2 \\ & + \left[ \frac{2\mu\lambda(2\ell^2 + 2\ell - 1)}{r^2(\lambda + 2\mu)} + \frac{4\mu^2(\ell^2 + \ell - 1)}{r^2(\lambda + 2\mu)} - \rho_0\omega^2 \right] y_3 - \frac{3}{r} y_4 \end{aligned} \quad (261)$$

where  $y_1$  is the radial displacement amplitude,  $y_2$  is proportional to the radial stress,  $y_3$  is tangential displacement amplitude and  $y_4$  is proportional to the tangential stress. The boundary conditions are that: (1) tangential stresses vanish at solid/fluid and solid/vacuum interfaces; (2) radial stresses (fluid pressures) are continuous across boundaries; and (3) displacements are continuous across all boundaries.

The equations of motion for fluid regions follow the spheroidal equations with the shear constant  $\mu = 0$ . In this case there exists only a longitudinal wave speed and the simplified equations are

$$\frac{dy_1}{dr} = -\frac{2}{r} y_1 + \frac{1}{\lambda} y_2 + \frac{\ell(\ell + 1)}{r} y_3 \quad (262)$$

$$\frac{dy_2}{dr} = -\rho_0\omega^2 y_1 \quad (263)$$

$$y_3 = -\frac{1}{r\rho_0\omega^2} y_2 \quad (264)$$



$$y_4 = 0. \quad (265)$$

Given material property functions [equations (251) to (253)], Alterman's equations can be numerically integrated in the single dimension  $r$ . Only certain values of the frequency  $\omega = \omega_{\ell s}$  will yield solutions that satisfy the boundary conditions. With judicious choices for boundary conditions and material properties, any spherically symmetric solid/fluid resonator can be modeled. For example, if a fluid is given a rigid boundary the  $\omega_{\ell s}$  are exactly those of Section II. The resonance frequencies of a solid shell can also be calculated. But the great advantage of this method is that real spherical systems, such as layered capsules important for ICF applications, are solvable. With this method the acoustic admittances of all interfaces are inherent in the calculation: the frequency shifts are computed directly.

### E. Discussion and Examples

The equations developed in this chapter can be applied to a representative National Ignition Facility (NIF) capsule under a variety of conditions. The geometric properties are shown in Appendix M and the relevant thermodynamic and physical properties are given in Appendices I and J. Consider the two extreme cases illustrated in Figure M1 (a), a filled capsule at room temperature and (b), the same capsule beta-layered at a temperature just below the fuel triple point. The following tables summarize frequency shifts and dissipation parameters for several low-order resonances of the interior gas. Frequencies are computed from equation (30). Penetration lengths are computed from equations (189) and (190). Frequency shifts due to thermal and viscous effects are computed from equation (250). Frequency shifts due to compliant boundary effects are computed by the method of Alterman (1959) outlined in the previous subsection. The real part of  $\Delta F$  is equal in magnitude to the viscous and thermal boundary dissipation. Specifically,  $\text{Im}(\Delta F) = -i \text{Re}(\Delta F)$ .

Table IV-1 shows the nine lowest frequency resonances associated with the interior gas of the representative ICF capsule at room temperature. The cavity radius  $a = 0.095 \text{ cm}$  and the frequencies listed in the second column are those for the rigid boundary solution. The remaining data illustrate most of the essential features related to frequency shifts and resonance broadening. Consider the following points:

1. The three characteristic penetration lengths are very small relative to the cavity radius and decrease with increasing frequency. Thus, all viscous and thermal dissipative effects are expected to be very small as well.
2. The bulk dissipation is quite small, showing that there is little acoustic dissipation in the bulk gas. The bulk dissipation increases with increasing frequency and  $g_b/f \lesssim 10^{-5}$  throughout.
3. Viscous and thermal boundary effects, given by  $\Delta F$ , are generally somewhat larger. For nonradial fundamental resonances  $\Delta F/f \sim 5 \times 10^{-4}$ . Overtone resonances show less dissipation. The radial modes also show little dissipation due to the absence of a viscosity effect.
4. The largest effect comes from the acoustic admittance of the shell. Generally,  $\Delta f_{sh}/f \sim 2 \times 10^{-3}$ . The radial modes work against a uniform expansion of the shell and thus show less dissipation – the shell appears more rigid. The  $\ell = 1$  modes work against an inertial reactance of the shell (these “sloshing” modes are illustrated in Appendix E) and behave as a coupled oscillator. The frequency is *increased* according to the expression given by Moldover *et al.* (1986)

$$\left( \frac{\Delta f_{sh}}{f} \right)_{1s} = \left( \frac{\text{mass of gas}}{\text{mass of shell}} \right) \left( \frac{1}{z_{1s}^2 - 2} \right). \quad (266)$$

This expression agrees with the numerically calculated values in Table IV-1. The increase has been observed experimentally in unpublished work by the author.

5. The lowest elastic resonance frequency of the shell occurs at about 1600 kHz. For gas resonances in the regions of shell resonances,  $\Delta f_{sh}$  can be calculated accurately but can vary unpredictably. This effect is already seen in the table which predicts  $(\Delta f_{sh})_{11} = +1275 \text{ Hz}$  while equation (266) predicts  $(\Delta f_{sh})_{11} = +1550 \text{ Hz}$ .

Table VI-1. Energy dissipation examples for the representative ICF capsule at room temperature

mode	$f$	$\bar{\delta}_v$	$\delta_v$	$\delta_t$	$g_b$	$\text{Re}(\Delta F)$	$\Delta f_{sh}$
$\ell, s$	kHz	$\mu\text{m}$	$\mu\text{m}$	$\mu\text{m}$	Hz	Hz	Hz
1,0	348.7	0.51	1.43	0.53	1	-150	+7447
2,0	559.9	0.39	1.13	0.42	2	-240	-1805
0,1	752.8	0.33	0.98	0.36	4	-57	-423
3,0	756.3	0.33	0.98	0.36	4	-330	-2152
4,0	946.0	0.30	0.87	0.32	7	-420	-2197
1,1	995.2	0.29	0.85	0.31	7	-78	+1275
5,0	1132	0.27	0.79	0.29	9	-510	-1907
2,1	1221	0.26	0.76	0.28	11	-102	-4140
0,2	1294	0.25	0.74	0.27	12	-74	-840

Table IV-2 shows the nine lowest frequency resonances associated with the interior gas of the representative ICF capsule at 20 K. The cavity radius  $a = 0.087 \text{ cm}$ . This smaller cavity radius (compared to that of the room temperature capsule) is due to the presence of an 80- $\mu\text{m}$ -thick solid DT fuel layer. The frequencies listed in the second column are those for the rigid boundary solution. The remaining data illustrate most of the essential features related to frequency shifts and resonance broadening. Consider the following points:

1. The characteristic penetration lengths are small relative to the cavity radius and decrease with increasing frequency. The viscous penetration length is noticeably the largest with a maximum value  $\delta_v/a \approx 0.079$  for the lowest frequency mode. This is due to the large (and relatively uncertain) bulk viscosity for the low-density DT gas.
2. The largeness of  $\delta_v$  carries over into the values for the bulk dissipation  $g_b$ . The frequency dependence is strong, so that over the range of data  $(g_b/f)_{10} = 0.007$  and  $(g_b/f)_{02} = 0.026$ .
3. The viscous and thermal boundary effects are of similar magnitude to that of the bulk dissipation. The radial and overtone modes are less strongly influenced, just as was noted in the room temperature case. For the fundamental nonradial modes  $\Delta F/f \sim 0.04$ .
4. The shell admittance effects, which now include both the beryllium outer shell and the DT solid inner shell, are somewhat smaller or the same order of magnitude as the viscous and thermal boundary effects,  $\Delta f_{sh}/f \approx 0.002$ . The inertial reactance effect for the  $\ell = 1$  modes is very small and is not apparent in the data. Thus, the shell admittance is likely more affected by proximity to elastic resonances in the solid DT or through complicated triply coupled oscillator effects.

Table VI-2. Energy dissipation examples for the representative ICF capsule near the triple point of DT

mode	$f$	$\bar{\delta}_v$	$\delta_v$	$\delta_t$	$g_b$	$\text{Re}(\Delta F)$	$\Delta f_{sh}$
$\ell, s$	kHz	$\mu\text{m}$	$\mu\text{m}$	$\mu\text{m}$	kHz	kHz	kHz
1,0	87.58	8.1	69	7.8	0.60	-3.46	-0.16
2,0	140.6	6.4	54	6.1	1.53	-5.68	-0.27
0,1	189.1	5.5	47	5.3	2.81	-0.38	-0.36
3,0	189.9	5.5	47	5.3	2.85	-8.28	-0.36
4,0	237.6	4.9	42	4.7	4.45	-10.8	-0.45
1,1	249.9	4.8	41	4.6	4.94	-0.82	-0.48
5,0	284.3	4.5	38	4.3	6.24	-13.3	-0.54
2,1	306.7	4.3	37	4.1	7.43	-1.37	-0.58
0,2	325.0	4.2	36	4.0	8.37	-0.49	-0.62

Comparison of the two ICF capsule cases shows that shell admittance effects dominate the frequency shifting and dissipation at high pressures, whereas at low pressure and temperature, no particular mechanism dominates. The  $Q$  of a resonator is a good measure of the combined dissipative effects. It can be defined as the ratio of the resonance frequency to the full-frequency width at half response-maximum for any measured resonance peak. If  $g_b$  is small relative to thermal, viscous, and shell effects then  $Q$  is given approximately by

$$Q \approx \frac{f}{2|\Delta f|}. \quad (267)$$

The dissipation is fairly large for the cryogenic capsule so that  $Q \leq 50$  is the rule. In contrast  $Q \sim 500$  is typical for high pressures at room temperature.

Consider a final example of an aluminum capsule (cavity radius 10 cm, shell thickness 1.0 cm) filled with one standard atmosphere of air. This case simulates laboratory settings that use spherical resonators to investigate gas properties. While the experimental details differ in excitation and detection of sound (as well as scale), it is interesting to consider the theoretical dissipation. Table VI-3 shows a compilation of the data.

The lowest-frequency shell resonance is at 5533 Hz, and the lowest frequency radial resonance is at 13.4 kHz. The table shows that the dissipation mechanisms are like those of the high-pressure room temperature ICF capsule example. The dominant dissipation comes from the shell admittance followed by the boundary effects. Careful consideration of these small effects has allowed experimenters to measure gas properties to a relative accuracy approaching  $10^{-6}$ . At this level of achievement it is also necessary to consider the effects of small cavity perturbations such as fill holes, seams, and other cavity boundary modifications.

The somewhat large positive values for the frequency shift due to the acoustic admittance of the shell (last column of Table VI-3) are of some concern. Equation (266) predicts a

shift of only +0.7 Hz for the low-frequency mode and less for the first overtone. It is probable that the table values represent the numerical calculation uncertainty rather than a physical effect. This should not be surprising or be taken as a weakness in the theory. The calculations were made using code designed for MHz resonances of millimeter-sized objects.

Table VI-3. Energy dissipation examples for an aluminum capsule filled with one standard atmosphere of air. The cavity radius is 10 cm and the shell thickness is 1.0 cm

mode	$f$	$\bar{\delta}_v$	$\delta_v$	$\delta_t$	$g_b$	$\text{Re}(\Delta F)$	$\Delta f_{sh}$
$\ell, s$	Hz	$\mu\text{m}$	$\mu\text{m}$	$\mu\text{m}$	Hz	Hz	Hz
1,0	1126	65	91	78	0.0013	-0.64	+3
2,0	1808	51	71	61	0.0033	-1.0	+3
0,1	2432	44	62	53	0.0061	-0.26	+3
3,0	2443	44	61	52	0.0060	-1.4	+3
4,0	3056	40	55	47	0.0095	-1.8	+4
1,1	3214	39	54	46	0.011	-0.35	+5
5,0	3656	36	50	43	0.014	-2.2	+5
2,1	3945	35	48	41	0.016	-0.45	+5
0,2	4180	34	47	40	0.018	-0.33	+6

## VII. APPLICATION DISCUSSIONS

This section is dedicated to discussions of specific measurement and data interpretation issues relevant to the characterization of ICF capsules.

### A. Vibration Detection Sensitivity

Many of the applications important to the ICF effort rely on accurate detection of acoustic resonances of the gas within a closed shell. These resonances are accompanied by shell motion as described in Section VI. Because the energy mainly exists in the interior the shell vibration amplitude can be quite small compared to the gas particle displacements. Detection of these modes is not simply a matter of exciting larger amplitude motion. It is important to keep the acoustic vibrations at a level for which the linear formalism is still applicable. Nonlinear effects can include increased energy dissipation and large resonance shifts. Consider then the following calculations which relate the acoustic pressure amplitude in the gas to the shell displacement at the outer surface.

Working with the rigid boundary equations as a good approximation for the cases of interest, the pressure in the gas for the radial modes is

$$\begin{aligned} P &= P_0 + P' \\ &= P_0 + \bar{P} j_0(k_{0s} r) e^{i\omega t} \end{aligned} \tag{268}$$

where  $\bar{P}$  is a constant. The radial mode expression and the results that follow are assumed to be representative of other resonances. It also simplifies the calculation. From Section I it follows that the particle velocity is

$$\vec{v} = -\frac{\bar{P}}{i\rho c} j_0'(k_{0s} r) e^{i\omega t} \hat{r}. \tag{269}$$

Also, the particle displacement is



$$\vec{x} = \frac{\bar{P}}{\omega \rho c} j'_0(k_{0s} r) e^{i\omega t} \hat{r}. \quad (270)$$

Now the maximum gas-particle displacement  $x^*$  is given by the maximum absolute value of equation (270):

$$x^* = \frac{\bar{P}}{\omega \rho c} j'_0(z_{0s}^*), \quad (271)$$

where the  $z^*$  are the values that yield the extremum in the Bessel function derivative. Now the maximum acoustic pressure in the cavity  $P^*$  occurs at the cavity boundary. Thus, by equation (268)

$$P^* = \bar{P} j_0(z_{0s}) \quad (272)$$

where the  $z_{0s}$  are the familiar roots given by equation (29). That is  $z_{0s} = \omega_{0s} a / c$ . Thus, the ratio of the maximum acoustic pressure to the ambient cavity pressure is

$$\frac{P^*}{P_0} = \frac{\rho c^2}{P_0} \frac{z_{0s} j_0(z_{0s})}{j'_0(z_{0s}^*)} \frac{x^*}{a}. \quad (273)$$

All that remains is to relate  $x^*$  with the shell displacement amplitude at  $r = b$ . This can be accomplished using the numerical calculations of Alterman (1959) outlined in Section VI. Each mode yields different results, so it is useful to write the expression

$$x^* = \alpha_s x_b, \quad (274)$$

where  $\alpha_s$  is the calculated constant. It is also reasonable to assume the low-density gas expression  $P_0 = \rho c^2 / \bar{\gamma}$  for cryogenic capsules. With these substitutions, equation (273) is written simply as

$$\frac{P^*}{P_0} = \bar{\gamma} \alpha \frac{z_{0s} j_0(z_{0s})}{j'_0(z_{0s}^*)} \frac{x_b}{a}. \quad (275)$$

Finally, if the Bessel function fraction is written as  $\bar{J}_s$  and the pressure ratio as  $\hat{P}$  then the shell surface displacement is expressed as

$$x_b = \frac{a\hat{P}}{\bar{\gamma}\alpha_s\bar{J}_s}. \quad (276)$$

Table VII-1 shows the results for the representative NIF capsule near 18K, however, deuterium was used as the fuel. The specific heat ratio  $\bar{\gamma} = 1.66$  and the cavity radius is 0.087 cm.  $\hat{P}$  is taken to be 0.01, and other values for  $x_b$  are proportional to the choice of  $\hat{P}$ .

Table VII-1

	$s = 0$	$s = 1$	$s = 2$
$\alpha_s (10^6)$	1.65	1.61	1.59
$\bar{J}_s$	2.24	5.90	9.17
$x_b$ (pm)	1.4	0.55	0.36

Table VII-1 shows that the gas particle amplitude is very large compared to the shell wall displacement. Furthermore, picometer ( $10^{-12}$  m) shell vibration amplitude is the limit for maintaining a linear acoustic description of the gas acoustics. Vibration detection systems with this capability fall into the regime of optical interferometry.

It is expected that the response of spheroidal modes would be comparable to somewhat larger than that shown in Table VII-1 – although for these modes the amplitude response varies over the surface of the shell. This analysis ignored viscous and thermal damping effects. Inclusion would allow  $x_b$  to be somewhat larger but still in the picometer range.

For gases at higher pressures the maximal amplitude restrictions are considerably relaxed. For example, the room temperature NIF capsule can have  $x_b = 3 \mu\text{m}$  for  $\hat{P} = 0.01$ . When computing results for these higher pressures, equation (276) can still be used with the caution that  $\bar{\gamma}$  can vary from its low-density value  $\rho c^2 / P_0$ .

## B. Pressure and Density

The pressure and density of a fluid enclosed in a spherical cavity are calculated quantities based upon a suitable equation-of-state (EOS) and measurements of sound velocity and temperature. To see how this might work, consider the general EOS

$$P = P(\rho, T) \quad (277)$$

and the corollary relation

$$c = \sqrt{\left(\frac{\partial P}{\partial \rho}\right)_S} = c(\rho, T). \quad (278)$$

These equations can in principle be inverted (or in practice numerically evaluated) to obtain the expressions

$$P = P(c, T) \text{ and} \quad (279)$$

$$\rho = \rho(c, T). \quad (280)$$

Measurement of the sound velocity is a fairly straightforward evaluation of the resonance spectrum based upon the basic equation (30) and the inclusion of cavity boundary dissipation effects [real part of equation (250)] and the compliant shell effects [calculated as described in Section VI-D]. Tables VI-1, VI-2, and VI-3 demonstrate that typically these dissipation effects can be ignored if a sound velocity within 0.5% is accurate enough and if the acoustic mode frequencies are significantly less than all elastic shell mode frequencies. This is especially true if the lowest frequency acoustic mode is ignored.

In addition, the resonance frequency set might be expected to show broken degeneracies due to small perturbations in the cavity shape. Two simple methods are given here for addressing broken degeneracy. Consider one frequency set

$$\{f_{\ell s}\} = \{f_{\ell s}^1, f_{\ell s}^2, \dots, f_{\ell s}^{2\ell+1}\} \quad (281)$$

of which some or all of the frequencies are known. Often the degeneracy is only partially broken so that all of the frequencies cannot be known by inspection. For sound velocity computations consider either

$$f_{\ell s} = \frac{f_{\ell s}^{\max} + f_{\ell s}^{\min}}{2} \quad (282)$$

which is the average of the extremal frequencies of the set, or

$$f_{\ell s} = \frac{\sum_{k=obs} f_{\ell s}^k}{n_{obs}} \quad (283)$$

which is the average of all observed frequencies. Either equation will yield similar results and the maximum possible error is

$$f_{\ell s}^{err} \leq \frac{2\ell-1}{4\ell+2} (f_{\ell s}^{\max} - f_{\ell s}^{\min}) \quad (284)$$

which can approach half the frequency range at large  $\ell$ . Typically, the uncertainty will be much less than indicated by equation (284).

Once the resonance frequencies are obtained by equation (282) or (283) and dissipative corrections are applied, the sound velocity can be computed using equation (30). Only one resonance is required to complete the calculation although use of several resonances is recommended. If  $N$  is the number of resonances to be used, the sound velocity is

$$c = \frac{2\pi a}{N} \sum_{\ell s} \frac{f_{\ell s}}{z_{\ell s}}. \quad (285)$$

The pressure and density are then given by equations (279) and (280). The resonant frequencies are typically known to within 0.5% without dissipative adjustments. The uncertainty in the cavity radius is often of the same order of magnitude except in carefully constructed experiments. If  $a$  is not known, then the density can be independently determined in cryogenic experiments which measure the temperature at which the cavity contents reach the saturation curve. This technique is described in Section VII-D.

If greater accuracy is desired for the sound velocity the following iterative procedure should be used. Consider the frequencies used above as the first-order estimates  $f^{(1)}$ . These frequencies yield the first-order values  $c^{(1)}$  and  $\rho^{(1)}$ . These values along with other physical property data can be used to compute the first-order dissipative frequency shifts  $\Delta f^{(1)}$  according to Section VI. The second-order frequencies are then  $f^{(2)} = f^{(1)} + \Delta f^{(1)}$ . This new set of frequencies can then be used to find the second-order values  $c^{(2)}$  and  $\rho^{(2)}$ . This process is continued until the values converge. Remember that  $f^{(n)} = f^{(1)} + \Delta f^{(n-1)}$  and not  $f^{(n)} = f^{(n-1)} + \Delta f^{(n-1)}$ .

One other method of determining the interior fluid density of a room temperature ICF capsule is next described. While the accuracy appears to be limited to about 5% for the hydrogens, it is given here because of its simplicity. Using the first one or two radial gas modes the frequency  $f_{10}$  can be estimated using equation (30). Small but important refinements can be made from approximate values for the density, viscosity, etc. and computing approximate values for the dissipative frequency shifts. This computed value of  $f_{10}$  and the measured value give the gas density through equation (266). Notice that this method is independent of any EOS.

### C. Isotope Ratio Determination

Measurement of the sound velocity can be used to measure the isotope ratio of a simple binary gas mixture at low density. Assuming the accuracy of the EOS expression

$$P = \frac{\rho RT}{M} \quad (286)$$

where  $M$  is the molecular weight of the gas mixture, the sound velocity is

$$c^2 = \frac{\bar{\gamma} RT}{M}. \quad (287)$$

Now let  $M_1$  and  $M_2$  be the molecular weights of the lighter and heavier isotopes respectively. Then the mole fraction of the lighter isotope  $x_1$  is

$$x_1 = \frac{\frac{\bar{\gamma}RT}{c^2} - M_1}{M_2 - M_1}. \quad (288)$$

The relative uncertainty in  $x_1$  is due to the uncertainty in  $c$ . It is

$$\frac{\delta x_1}{x_1} = \frac{M}{M_2 - M_1} \frac{2\delta c}{c}. \quad (289)$$

Equation (289) shows that the relative uncertainty in the mole fraction is twice the uncertainty in the sound speed multiplied by a molecular weight prefactor. This ratio can be very large for heavy isotopes, rendering this acoustic isotope analysis impractical. However, the case of greatest interest to the fusion energy community is mixtures of deuterium and tritium. In this case the prefactor is  $\sim 4.5$  and an uncertainty in the sound speed of 0.5% translates into about a 5% uncertainty in the mole fraction. This may be acceptable for some applications.

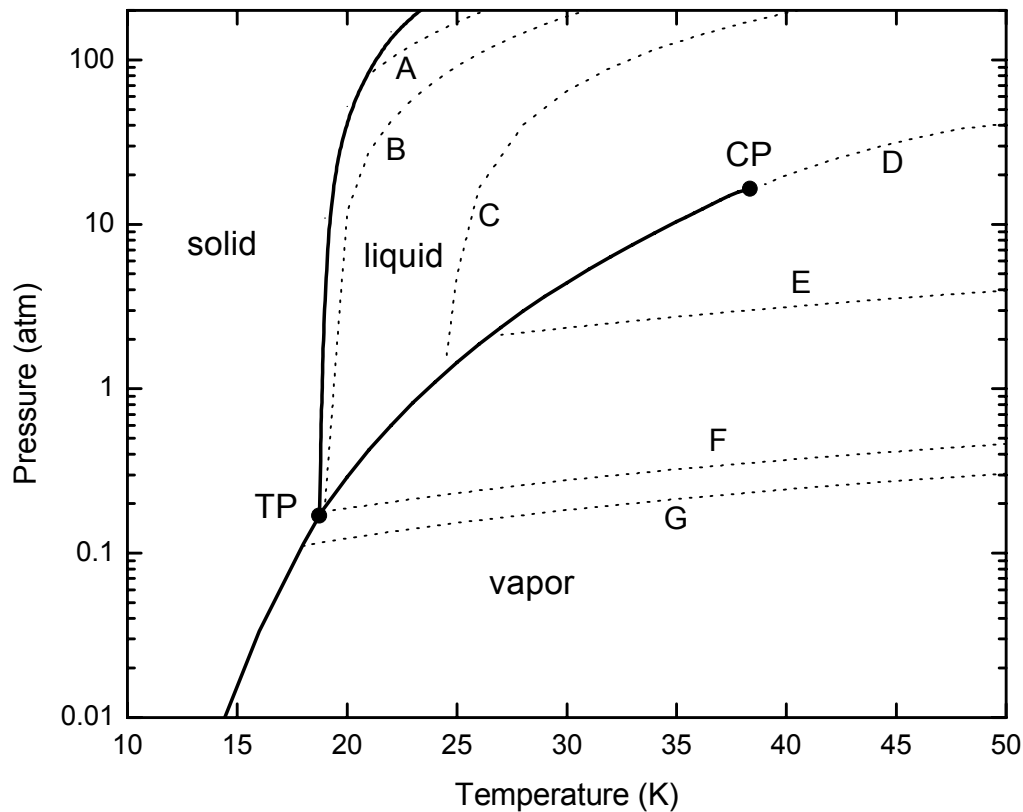
High-pressure gases that do not necessarily obey equation (286) may still be evaluated in this manner as long as an effective  $\bar{\gamma}$  is known for the density and temperature of interest and does not differ between isotopes. In other terms, for isotopes at a fixed temperature, the sound velocity can be expressed in the form of equation (287) provided that  $c \propto M^{-1/2}$ . This condition is satisfied by hydrogen and deuterium to within the uncertainty of known EOS (0.6%) up to 400 atm pressure at 300 K. It is reasonable to assume that DT mixtures should provide similar results.

#### **D. Phase of Interior Cavity Contents**

Several possibilities exist for acoustic observation of phase changes and the phase state of the interior fluid of a spherical cavity. Many of these measurements can be useful for ICF capsule experimenters. Discussion of the distribution of solid hydrogen is deferred to later sections. Consider the following:

## 1. Coexistence Curves

Typical ICF capsules are filled with high-density hydrogen isotope fuel mixtures. When these capsules are cryo-cooled the contents will undergo phase separation as contact is made with the coexistence curves. As an illustration, consider the P-T phase diagram of deuterium shown below. This plot displays the coexistence curves as solid lines. The triple point (TP) is at the intersection of these curves and the critical point (CP) is at the high-temperature end of the liquid/vapor curve. Several constant-density cooling curves are shown as dotted lines. Because an ICF capsule cavity maintains a nearly constant density of fuel, these lines are indicative of potential cooling paths.



The deuterium densities (in  $\text{mg}/\text{cm}^3$ ) associated with each path are (A) 180; (B) 174; (C) 100; (D) 67.7; (E) 4.0; (F) 0.455; (G) 0.20. Curves B and F are of density such that the thermodynamic path first reaches a coexistence curve at the TP. Curve D represents the

critical density path. The representative ICF capsule has a fill density near  $48 \text{ mg/cm}^3$  and its path lies just below that of the critical density path. It reaches the liquid-vapor coexistence curve in a manner similar to curve E but at a temperature of about 38.1 K.

Consider the specific example of curve E. The density of deuterium gas in the cavity is  $4.0 \text{ mg/cm}^3$  at all temperatures (ignoring thermal contraction of the shell). At room temperature this corresponds to a pressure of 24.6 atm. Cooling the capsule to 50 K reduces the pressure to 4 atm – this is where the curve enters the right side of the graph. Further cooling results in additional lowering of the pressure until the liquid-vapor coexistence curve is reached at about 27 K. At this point liquid begins to condense out of the gas. Upon further cooling, the path runs along the coexistence curve. The volume ratio of liquid to gas is determined by the densities of the individual phases and by the total density constraint. Cooling to the TP temperature ( $T_{TP} = 18.73 \text{ K}$ ) results in the beginning of deuterium solidification. Additional cooling results in a path along the solid-vapor coexistence curve, and aside from the possibility of supercooling, the cavity contains solid and vapor in equilibrium. Any warming or cooling of the capsule results in a movement in this thermodynamic space only along the curve E and the coexistence curves just described.

Acoustic techniques can be used to accurately map the liquid-vapor coexistence curve. Two possible techniques are now described. First, a single capsule of known (or measured) fill density between  $0.5$  and  $67 \text{ mg/cm}^3$  is cooled to a temperature just above that where it will reach the coexistence curve. The specified density range guarantees that the contents will be gaseous (curve E falls in this range). As the temperature is now slowly lowered the sound velocity and resonance frequencies are also lowered. At the point where liquid begins to condense into the cavity the *measured* sound velocity and resonance frequencies will *increase*. This is due to an effective cavity volume reduction by the presence of liquid. The temperature at which the sound velocity is at minimum is the location of the coexistence curve for the known density. Calculations of this effect using known EOS and coexistence curve data suggest that this method can be accurate to within a few mK (within a few degrees of the critical point temperature). One possible



difficulty of this technique is the potential appearance of a precondensation effect – condensation of liquid at slightly higher temperatures induced by acoustic fluctuations. Interestingly, this effect is minimized by having smoother surfaces, having small surface-to-volume ratio cavities, and by using shells of high thermal conductivity – all desirable properties of ICF capsules. Even if all of these effects can be sorted properly, there is still only one point along the curve that can be measured by any given capsule.

A modified version of the above scenario is to use a spherical shell with a cavity in communication to a small warm volume via a fill tube. In a nonacoustic experiment, pressure and temperature data can be obtained for small regions of the liquid-vapor coexistence curve. Because the thermodynamic path is no longer one of constant density, pressure, or temperature, care must be taken to ensure that the PT data actually represent a state along the coexistence curve. That is, the capsule is partially full of liquid and this liquid is in equilibrium with the vapor. In practice, the beginning of the cooling curve path would look very similar to curve E in the graph, then travel some distance down along the coexistence curve as the capsule fills, and finally leave the coexistence curve to the left into the liquid region when the capsule is full. This method has been used to examine the coexistence curve of deuterium in unpublished work by the author.

## **2. Other Liquid and Solid Detection Methods**

For cavities filled with either liquid or solid, the methods described throughout this work can accurately characterize the material. The case of a cavity filled with solid is accurately treated by the methods of Alterman (1959) outlined in Section VI-D provided that the two solid materials are mechanically isotropic. A fluid-filled spherical shell is treatable using the same methods given throughout this report for gases. Care must be taken, however, to consider the possibly large shell-admittance, viscous, and thermal boundary effects.

Of greater interest for the present work is the consideration of detecting mixed phases within the cavity. The method already mentioned in the previous subsection relies on measurement of gas resonance frequency shifts due to effective cavity volume changes.

However, the presence of liquid or solid condensed from the vapor will also affect the resonance frequencies of the enclosing spherical shell. The essential point is that a small amount of liquid or solid will provide a small mass-load shift to the shell resonances. Because  $f \propto mass^{-1/2}$  it is quickly computed that a 400-Hz frequency shift of a 1.6-MHz resonance corresponds to about 1% of the gas mass in an ICF capsule. With care, one might practically expect to be able to detect frequency shifts at just about this level. This 1% gas mass corresponds to a spherical solid mass of radius 210 microns or a spherical liquid mass of radius 220 microns. Spread over the inner surface of the shell this quantity is a layer about 4 microns thick.

The toroidal modes of the shell, characterized by transverse motion only, can only couple motion into the fluid through viscous effects. It can be expected that only the liquid quantities within about a viscous penetration length of the shell will provide a mass load to the resonance motion. From equation (189),  $\delta_v \propto f^{-1/2}$ , so that for the lowest frequency torsional mode of an ICF capsule (2.77 MHz) at cryogenic temperatures (see Table VI-2),  $\delta_v \approx 12\mu m$ . For all practical purposes, the detectable fluid quantities mass load the low frequency torsional and spheroidal modes.

Detection of small quantities of liquid or solid is likely limited to 1% of the total cavity mass through the method of observing shell resonance frequency shifts due to mass loading.

### 3. Supercooling

It is possible that carefully manufactured and highly polished capsules may allow the liquid contents to supercool as the temperature is slowly lowered through  $T_{TP}$ . This phenomenon has been visually observed with DT mixtures in translucent polymer capsules. In an unknown isotope mixture (unknown  $T_{TP}$ ) it is not clear when supercooling has occurred. It will be acoustically evident, however, when the mixture does freeze. It will freeze very quickly and completely, inducing a sudden shift in the shell resonance frequencies. If the mixture froze from the vapor, the shift would also be

large – on the order of tens of kHz. Because the mixture freezes from the liquid, the spheroidal shell resonances are significantly mass loaded both before and after freezing. The torsional modes are less significantly mass loaded, and the resonance shifts due to sudden freezing may be as large as several kHz. The author has observed freezing shifts on the order of 5 kHz for a 180 kHz resonance of a deuterium-filled aluminum capsule. Such frequency shifts are not expected to be quantitatively reproducible for they may depend largely on the exact nature of the quick freeze. More or less solid may be mechanically attached to the shell each time the liquid is frozen; there is no guarantee that the freeze will occur in any organized fashion.

#### **4. Triple Point Measurement**

In the absence of supercooling the measurement of  $T_{TP}$  is straightforward. At temperatures just above  $T_{TP}$  the resonance signature of the capsule is that of a fluid loaded shell. Small changes in temperature will not change the resonance spectrum to any measurable degree. Now if the temperature is lowered below  $T_{TP}$  the liquid will begin to freeze. The rapidity of the freeze depends upon proximity to the TP but usually occurs in seconds to a few minutes unless the temperature happens to be within a few mK of  $T_{TP}$ . When complete, this freeze will manifest itself in a shift in shell resonances that would not otherwise occur. The mass load to the shell becomes somewhat greater, and the fuel distribution will be to some degree more even around the cavity interior.

The effects on the resonance spectrum are threefold. First, the nearly-degenerate peaks within any resonance group will tend to reorient relative to each other due to the change in symmetry. In fact more peaks may be evident because the solid is not likely to be as symmetric a mass as a pool of liquid. Second, the overall breadth of the resonance group may decrease if the solid freezes with more polar symmetry than a liquid pool. Third, each resonance frequency group may show a downshift due to the better mass coupling property of the solid over the liquid. These effects are all subtle but within the capability of careful resonance measurements.

If supercooling is observed then the TP can be found by the reverse procedure. Supercooling is induced and then the temperature is incrementally raised until the liquid transition is observed with all of the characteristics just described.

### **E. Cavity Boundary Characterization**

While the overall structure of the cavity resonance spectrum reveals information on the physical properties of the contained fluid or solid, the fine structure reveals information on the shape of the cavity. Some aspects of this fine structure interpretation have been discussed in Sections III through V. The present discussion seeks to encapsulate these previous ideas and present workable data inversion techniques.

A quick review of the resonance fine structure reveals the following properties:

1. A spherical cavity is characterized by a resonance spectrum whose experimental resonances  $f_{\ell s}$  [given by equation (30)] have degeneracy  $2\ell + 1$ . This degeneracy is experimentally indistinguishable. Fine structure is not present. These properties are due to the high degree of symmetry of a spherical object.
2. Any alteration of the spherical symmetry of the cavity (distortions, defects, etc.) will induce breaking of the degeneracies of the resonance frequencies. Typically, defects of high symmetry will induce only partial degeneracy breaking while defects of low symmetry can induce complete degeneracy breaking.
3. To first order in a boundary perturbation theory, degeneracies are affected only by even-order boundary defects. The fine structure is indicative of only even-order distortions of the cavity.
4. To first order in a boundary perturbation theory, the mean resonance frequency of any fine structure group is unchanged. This also applies to the nondegenerate radial resonances.
5. The degree of degeneracy breaking (frequency shifting) is linear in the perturbation parameters.

6. Axisymmetric perturbations induce a partial degeneracy breaking that results in  $\ell + 1$  experimentally detectable resonances in the fine structure group. This property is unique among all possible general perturbations.
7. A perturbation of even-order  $p$  [see equation (39) or equation (84)] affects all resonances of order  $\ell \geq p/2$ . A resonance of order  $\ell$  is only affected by even-order perturbations  $p \leq 2\ell$ .
8. A general perturbation of order  $p$  is described by  $p+1$  parameters  $c_{pq}$  where  $q \in \{0, 1, \dots, p\}$ . The fine structure of a resonance of order  $\ell$  is described by  $4\ell^2 - 1$  parameters.

Even from a theoretical standpoint, the task of inverting frequency data into cavity shape information is daunting. The greatest analysis hurdle and the focus of much of the following discussion is centered on point 8 above: computing a large number of deformation coefficients from a limited set of resonances. Points 2, 4, 6, and 7 describe helpful analysis limitations that make the task manageable in many situations. Additional difficulties associated with resonance  $Q$ 's and cryogenic measurements are deferred to the next subsection on solid fuel distribution. For the present, assume easily detectable high- $Q$  resonances.

The inversion task is to find the deformation coefficient set that describes a nearly spherical cavity based upon the resonance spectrum (coarse and fine structure) of a fluid filling the interior. Let this inversion operation be denoted  $\mathbf{W}$  such that

$$\mathbf{W}\{f_{\ell s}^h\} \rightarrow \{c_{pq}\}, \quad (290)$$

where it is understood that:  $p$  is even;  $q \in \{0, 1, \dots, p\}$ ;  $\ell$  and  $s$  identify the unperturbed cavity resonance; and  $h \in \{-\ell, \dots, 0, \dots, +\ell\}$  enumerates the fine structure frequencies. A consideration of the lowest-order fine structure group  $f_{10}^h$  illustrates the essential difficulties of the inversion operation. For this case the operation given by

$$\mathbf{W}\{f_{10}^{-1}, f_{10}^0, f_{10}^1\} \rightarrow \{c_{20}, c_{21}, c_{22}\}. \quad (291)$$

At first glance the solution seems clear: given the frequencies and point 4 above, equation (104) is used to solve for the three perturbation parameters. But even in this simple case the solution is not unique, for only two parameters are required to describe three frequency shifts whose average remains fixed. The situation is only exacerbated by inclusion of more frequencies. Three routes to a unique solution suggest themselves.

### 1. Coefficient Reduction by *a priori* Knowledge

It may be possible to use additional experimental information to reduce the number of perturbation coefficients. This is the likely case for cavities constructed from hemishells. The  $\ell = 1$  operation becomes

$$\mathbf{W}\{f_{10}^{-1}, f_{10}^0, f_{10}^1\} \rightarrow \{c_{20}, c_{21}\} \quad (292)$$

which has a unique solution. Equation (292) is equivalent to equation (154). Even better, the general hemishell construction operation is also uniquely solvable due to the significant reduction of necessary perturbation parameters

$$\mathbf{W}\{f_{\ell 0}^h\} \rightarrow \{\sigma, \gamma\}. \quad (293)$$

Notice that it is only necessary to use the lowest-order frequency to obtain the coefficients. For this special case  $c_{p1} \propto c_{21} \propto c_{20}$  so the problem is actually overspecified – see Section IV-E. Other coefficient reduction schemes may also prove useful, but it would be difficult to categorize the possibilities. Remember, almost any reasonably defensible coefficient reduction will lead to a unique solution, thus it is worth the mental effort to closely examine the particular experiment of interest.

### 2. Incorporating Overtone Frequencies

The  $\ell = 1$  problem can also be solved through the use of overtone frequencies. Specifically,

$$\mathbf{W}\{f_{10}^h, f_{11}^h\} \rightarrow \{c_{20}, c_{21}, c_{22}\} \quad (294)$$

does, in general, have a unique solution. The use of the first overtone as well as the fundamental frequency provides the additional information necessary for uniquely determining the full coefficient set. In fact,

$$\mathbf{W}\{f_{\ell 0}^h, f_{\ell 1}^h\} \rightarrow \{c_{pq}\} \quad (295)$$

also has a unique solution. In principle this solves the difficulty of having too many unknowns. In practice, the use of the overtone frequencies can be inhibiting. They are of significantly higher frequency and thus subject to any number of detection difficulties.

### 3. Axisymmetric Solutions

Again considering the  $\ell = 1$  problem, assume a (possibly unrealistic) axisymmetric perturbation ( $c_{21} = 0, c_{22} = 0$ ). In this case there are only two distinct frequencies of which the degeneracy is indeterminate. The unperturbed frequency now becomes one of the parameters to be found

$$\mathbf{W}\{f_{10}^0, f_{10}^1\} \rightarrow \{c_{20}, f_{10}\}. \quad (292)$$

While the solution of equation (292) is still not unique, there are only two possible solutions based upon two possible degeneracy scenarios of the experimental frequencies. Inclusion of a radial mode frequency and higher-order frequencies renders a unique solution. That is

$$\mathbf{W}\{f_{0s}, f_{\ell 0}^{h'}\} \rightarrow \{c_{p0}\} \quad (292)$$

where  $h' \in \{0, 1, \dots, \ell\}$  indicates the reduced set of frequencies within a fine structure group. Recall that for axisymmetric perturbations the group consists of at most  $\ell + 1$  resonances. Details of this particular method and its usefulness are discussed later in this section.

The three scenarios above, while differing in the details of useful frequencies and coefficients, follow a general solution recipe  $\mathbf{W}$ . The procedure is as follows:

1. Using the lowest-order  $\ell = 1$  frequency group  $\{f_{10}^h\}$  or groups  $\{f_{1s}^h\}$ , calculate the lowest-order deformation coefficients  $\{c_{2q}\}$ . This is accomplished by the  $\mathbf{B}^{1s}$  matrix formalism of Section III-E.
2. Using the  $\ell = 2$  frequency group(s) and the just computed  $p = 2$  coefficients, calculate the  $p = 4$  coefficients  $\{c_{4q}\}$ . This is done with the  $\mathbf{B}^{2s}$  matrix.
3. Continue to increment  $\ell$  so that the  $\ell = L$  frequency group(s)  $\{f_{Ls}^h\}$  along with the  $p \leq 2L - 2$  coefficients  $\{c_{2q}, c_{4q}, \dots, c_{2L-2,q}\}$  are used to compute the next coefficient set  $\{c_{2L,q}\}$ .

It is important to note that this procedure requires a full set of frequencies  $\ell = 1, 2, \dots, L$  that begins with 1 and runs up to some maximum value  $L$  without any gaps. Consider a simple numeric example of an axisymmetric cavity. Let the data set consist of the following “experimental” frequency information (given in Hz):

$$f_{01} = 752750$$

$$\{f_{10}^h\} = \{347450, 351350\}$$

$$\{f_{20}^h\} = \{553650; 556450; 566500\}$$

$$\{f_{30}^h\} = \{747450; 750450; 760800; 761300\}$$

Viscous, thermal, and shell admittances can be incorporated into the analysis but will not be done here in the interest of clarity. Each frequency set consists of  $\ell + 1$  individual frequencies, each of which is doubly degenerate except one that is nondegenerate. Which frequency in a set is nondegenerate is not known *a priori* but is calculated using the radial resonance. This is the first task and quickly reveals  $f_{10} = 348735$ ,  $f_{20} = 559915$ , and  $f_{30} = 756266$ . The experimental eigenvalues of  $\mathbf{B}^{10}$  are then

$$(f_{10}^0 - f_{10})/f_{10} = -0.003685$$

$$(f_{10}^1 - f_{10})/f_{10} = +0.007499.$$

Because the eigenvalues must sum to zero, the second frequency  $f_{10}^1$  is the nondegenerate value. These two eigenvalues give an average value for the coefficient  $c_{20} = +0.0129$ . Next, the experimental eigenvalues of  $\mathbf{B}^{20}$  are



$$(f_{20}^0 - f_{20})/f_{20} = -0.01118$$

$$(f_{20}^1 - f_{20})/f_{20} = -0.006176$$

$$(f_{20}^2 - f_{20})/f_{20} = +0.01177.$$

Again the condition that the eigenvalue sum be zero identifies the nondegenerate frequency as  $f_{20}^0$ . These eigenvalues and the coefficient  $c_{20}$  determine the average value of the next deformation coefficient as  $c_{40} = -0.0210$ . The next experimental values of  $\mathbf{B}^{30}$  are

$$(f_{30}^0 - f_{30})/f_{30} = -0.01166$$

$$(f_{30}^1 - f_{30})/f_{30} = -0.007690$$

$$(f_{30}^2 - f_{30})/f_{30} = +0.005995$$

$$(f_{30}^3 - f_{30})/f_{30} = +0.006656.$$

The zero eigenvalue sum condition identifies the nondegenerate frequency as  $f_{30}^0$ . The average value of the last deformation coefficient is  $c_{60} = -0.0095$ . The actual coefficients upon which the frequency data were originally calculated are  $c_{20} = +0.0130$ ,  $c_{40} = -0.0210$ ,  $c_{60} = -0.0090$ . This quick example shows that the coefficients are recoverable as long as great care is taken in the frequency measurements. The “data” are given to within the nearest 50 Hz and yet the  $c_{60}$  coefficient is off by six percent. Although the solution is unique in the case of zero uncertainty, the uncertainty tends to grow significantly with each step.

A general solution for extracting deformation coefficients of a nonaxisymmetric cavity, while possible in principle, is somewhere between cumbersome and impossible in practice. Difficulties include distinguishing up to  $2\ell + 1$  eigenfrequencies within a group, accounting for degeneracies, and utilizing several different  $s$ -value modes for each  $\ell$ -value. Even the simplest case for which  $\ell = 1$  is not readily solved. The axisymmetric deformation coefficients, however, are readily obtained by the method and example just described. In many cases involving regular geometries (such as ICF target mounting structures), it is likely that capsules and fuel layers will be nearly axisymmetric and the

methods described above will yield quantitative results. In a general scenario it is important to explore the possibility of using an axisymmetric analysis as a qualitative solution to the general problem. Clearly, the individual frequencies cannot be used in an inversion such as

$$\mathbf{W}\{f_{\ell s}^h\} \rightarrow \{c_{p0}\} \quad (293)$$

because there is no reason to believe that the axisymmetric coefficients should yield the correct frequency splitting *even if* there were exactly  $\ell + 1$  observed frequencies per resonance. Instead, consider the inversion first mentioned in Section V-C, which can be written

$$\mathbf{W}\{f_{0s}, f_{1s}^{\min}, f_{1s}^{\max}, \dots, f_{Ls}^{\min}, f_{Ls}^{\max}\} \rightarrow \{c_{20}, c_{40}, \dots, c_{2L,0}\}. \quad (294)$$

The required data are the minimum and maximum observed frequencies for resonances of order  $\ell \leq L$ . Any overtone will suffice for a given  $\ell$  although in practice it may prove most easy to use the fundamental for each mode. The frequency  $f_{0s}$  establishes the ratio  $c/a$ . At the same time consider the less restrictive inversion

$$\mathbf{W}\{f_{0s}, f_{1s}^{\min}, f_{1s}^{\max}, \dots, f_{Ls}^{\min}, f_{Ls}^{\max}\} \rightarrow \{\tilde{\Pi}_2, \tilde{\Pi}_4, \dots, \tilde{\Pi}_{2L}\} \quad (295)$$

where

$$\tilde{\Pi}_{2\ell} \equiv \sum_{\substack{p=2 \\ \text{even}}}^{2\ell} \tilde{c}_{p0}^2 \quad (296)$$

is a measure of the summed power of deformation modes. The tilde notation indicates that the deformation coefficients are not expected to represent the true shape of the cavity. Rather, the strategy here is to establish that the frequency span  $f_{\ell s}^{\max} - f_{\ell s}^{\min}$  of any given resonance group  $f_{\ell s}$  is approximately a function of  $\tilde{\Pi}_{2\ell}$ . Or in other words, it is sought to identify the validity of the power-preserving approximation

$$\tilde{\Pi}_{2\ell} \approx \Pi_{2\ell} \equiv \sum_{\substack{p=2 \\ \text{even}}}^{2\ell} \sum_{q=-p}^p c_{pq}^2. \quad (297)$$

The right-hand-side of equation (297) is the actual deformation power for a given set of coefficients  $c_{pq}$ . The left-hand-side is the power computed using the inversion of equation (295) described in Section V-C.

To test the validity of equation (297), mock data were constructed using random values for cavity deformation coefficients. Let  $N$  be the number of numerically created cavities. The following constraints apply

$$\sum_{\substack{p=2 \\ \text{even}}}^{2\ell} \sum_{q=-p}^p c_{pq}^2 \leq \frac{\alpha}{1-\alpha} \sum_{\substack{p=2 \\ \text{even}}}^{2\ell} c_{p0}^2 \quad (298)$$

$$c_{p,-q} = (-1)^q c_{pq} \quad (299)$$

$$c_{p1}^2 \geq c_{p2}^2 \geq \dots \geq c_{pp}^2 \quad (300)$$

$$\sum_{n=1}^N \frac{|c_{p0}|}{N} = u; \quad 0.9 \leq \left| \frac{c_{p0}}{u} \right| \leq 1.1 \quad (301)$$

Equation (298) establishes a measure of a cavity's axisymmetry using a coefficient  $0 \leq \alpha \leq 1$ . If  $\alpha = 1$  then the cavity is axisymmetric and as  $\alpha$  tends toward zero the axisymmetric coefficients vanish. Equation (299) is the condition that yields a real cavity boundary. Equation (300) forces the cavity shape to be azimuthally less complicated. These first three conditions allow the construction of cavities that conform to manufacturing expectations. And finally, equation (301) forces the average value of each of the axisymmetric coefficients to the same value  $u$ ; and individually variable by 10% from this value. This last condition is mainly imposed so that the data can be graphed in a visually clear manner. Once the deformation coefficients are selected the frequencies are computed according to the boundary perturbation theory. These frequencies are then fit according to equation (295) to obtain the axisymmetric fit power  $\tilde{\Pi}_p$ . Finally this power can be compared with the actual power of the coefficients used to construct the

data  $\Pi_p$ . For each value of  $\alpha$  considered the data set consisted of  $N = 256$  cavities. The “goodness of fit”  $\delta$  for a given cavity is defined by

$$\delta^2 \equiv \frac{1}{2L} \left[ \sum_{\ell=1}^L \left( \frac{\hat{f}_{\ell 0}^{\min} - f_{\ell 0}^{\min}}{f_{\ell 0}^{\min}} \right)^2 + \sum_{\ell=1}^L \left( \frac{\hat{f}_{\ell 0}^{\max} - f_{\ell 0}^{\max}}{f_{\ell 0}^{\max}} \right)^2 \right] \quad (302)$$

where  $\hat{f}$  indicates the axisymmetric-fit frequency. Also of interest is the data inclusion factor  $R_{\bar{\delta}}$  defined by

$$R_{\bar{\delta}} \equiv \frac{\text{number of data sets with } \delta \leq \bar{\delta}}{\text{total number of data sets}}. \quad (303)$$

In practice  $\delta < 1$  so that we define  $R_1 = 1$ . Typically the subscript for  $R$  is omitted.

Figures VII-1 through VII-9, given on the following pages, display data for differing  $\alpha$  and  $\bar{\delta}$ . The six different graph symbols represent the sum deformation power, equation (296), for the following values of  $p$ : 2 – triangle; 4 – square; 6 – hexagon; 8 – star; 10 – cross; and 12 – circle. The essential features of this axisymmetric decomposition technique are:

1. The total power of the deformation through mode 12 is generally recoverable for data with a goodness-of-fit less than 0.04; this restriction corresponds to  $R > 84\%$ .
2. Data with larger values of  $\alpha$  (higher modeled axisymmetry) are fit with higher confidence. However, spurious fits for  $p \geq 10$  still represent a few percent of possible cases.
3. The power in any individual mode has a much higher uncertainty than the total power. The exception is mode 2 for which the power is recoverable with very low uncertainty.
4. The average value of  $\tilde{\Pi}_p$  for a set of cavities is larger than the average value of  $\Pi_p$  by a few percent. This difference is reduced for higher  $\alpha$ .
5. Spurious data tend to overestimate the power. Certainly, the largest deviations of the fit are overestimations.

A second test of equation (297) was performed using a slightly altered axisymmetric fitting routine. In this case it is assumed that the radial mode frequency, and therefore the ratio  $c/a$  is missing or unreliable. The mock data now consist of the total relative frequency spread for each mode, and the inversion is

$$\mathbf{W}\{\Delta f_{1s}, \Delta f_{2s}, \dots, \Delta f_{Ls}\} \rightarrow \{\tilde{\Pi}_2, \tilde{\Pi}_4, \dots, \tilde{\Pi}_{2L}\} \quad (304)$$

where

$$\Delta f_{\ell s} \equiv 2 \frac{f_{\ell s}^{\max} - f_{\ell s}^{\min}}{f_{\ell s}^{\max} + f_{\ell s}^{\min}}. \quad (305)$$

As is evident from equation (305) the unperturbed resonance frequency is taken to be the average of the maximum and minimum observed frequencies for each mode. The goodness-of-fit function is taken to be

$$\delta^2 \equiv \frac{1}{L} \sum_{\ell=1}^L \left( \frac{\hat{\Delta f}_{\ell 0} - \Delta f_{\ell 0}}{\Delta f_{\ell 0}} \right)^2. \quad (306)$$

The results of this type of axisymmetric fitting are shown in Figure VII-10. This single set of data shows the fits for 256 constructed cavities of  $\alpha = 0.95$ . This type of fit does have a rather large uncertainty, but it is not plagued by outliers. The standard deviation for a given  $p$  value is roughly constant, and the average values are large by a few percent. Other values of  $\alpha$  from 0.50 to 0.99 have little effect on the quality of the fit – the method is very robust.

$$\alpha = 0.80 \quad \bar{\delta} = 1 \quad R = 1$$

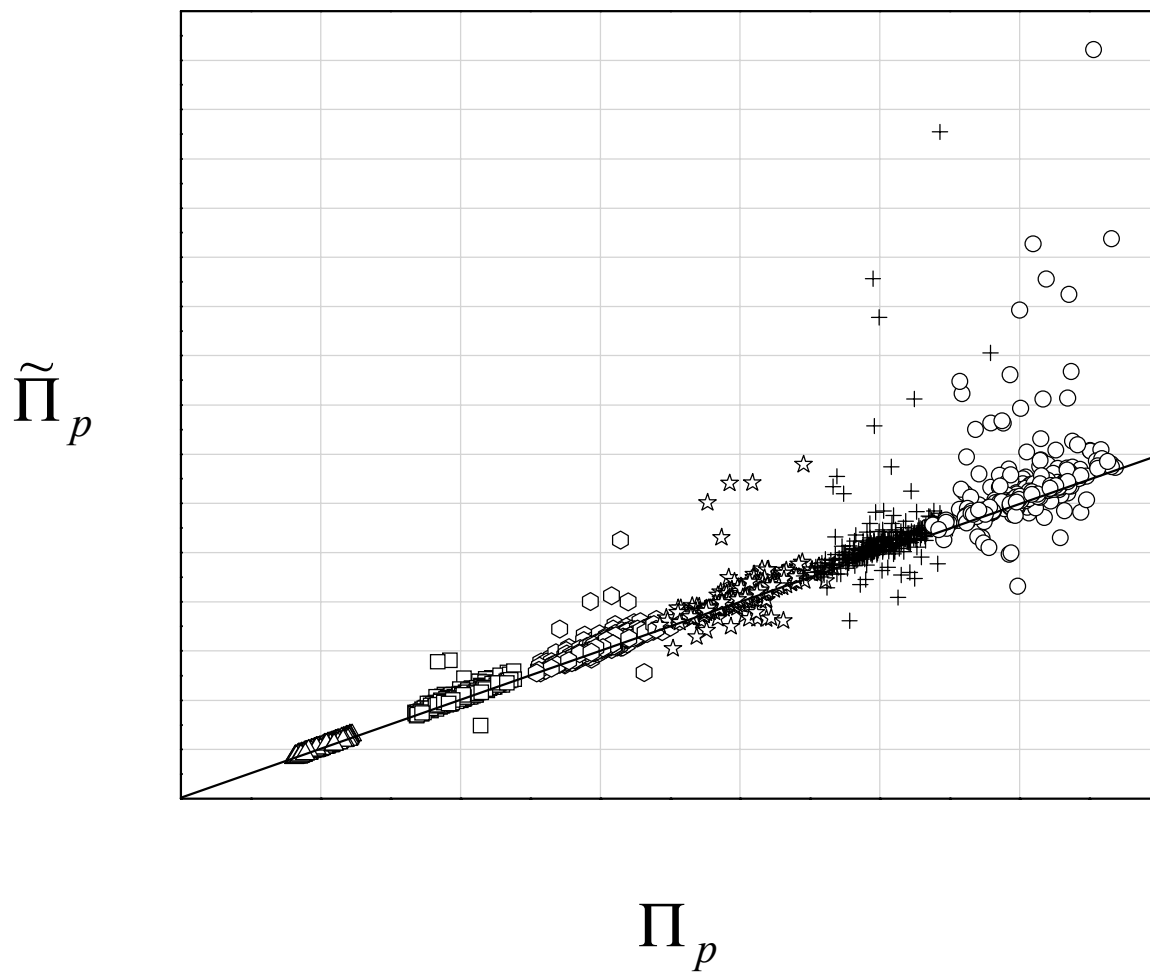


Figure VII-1

$$\alpha = 0.90 \quad \bar{\delta} = 1 \quad R = 1$$

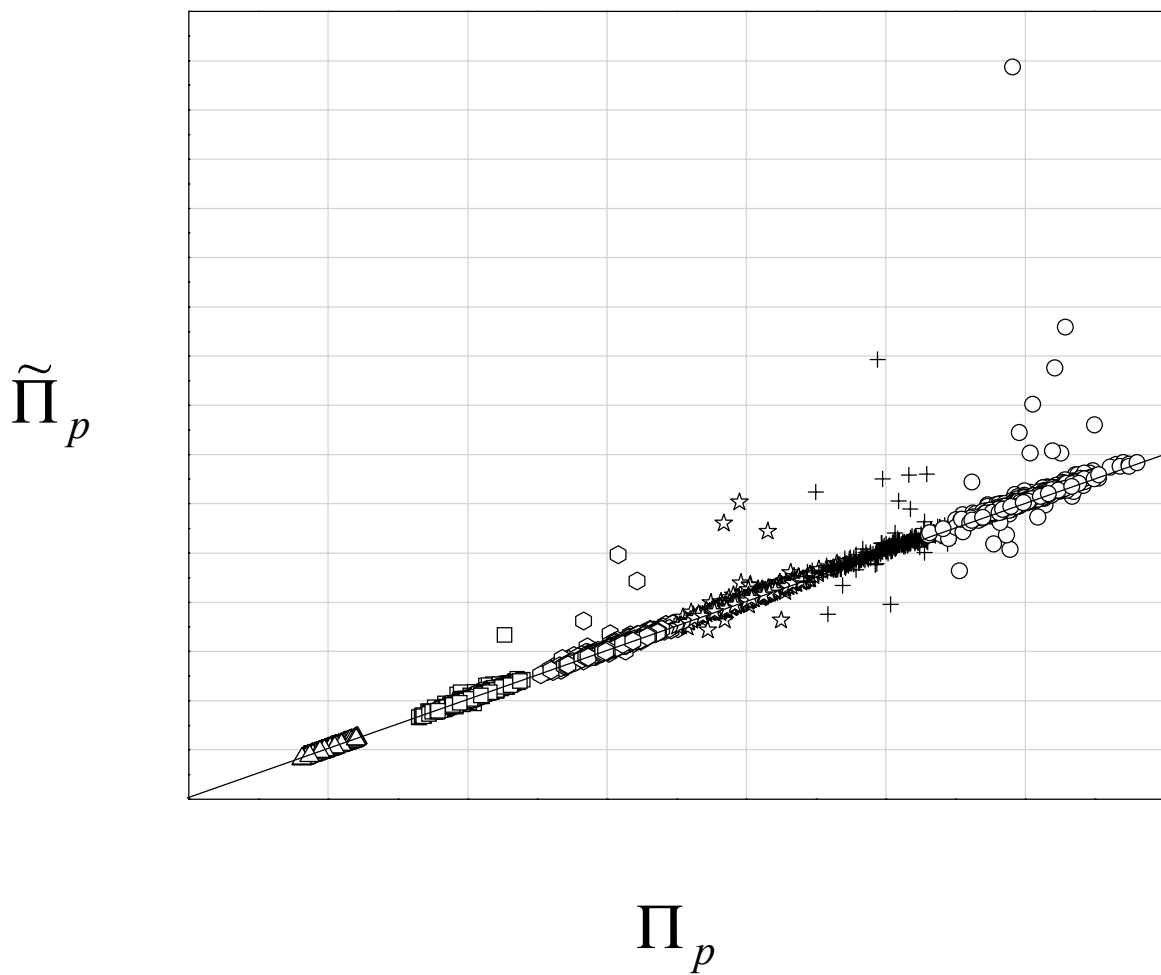


Figure VII-2

$$\alpha = 0.95 \quad \bar{\delta} = 1 \quad R = 1$$

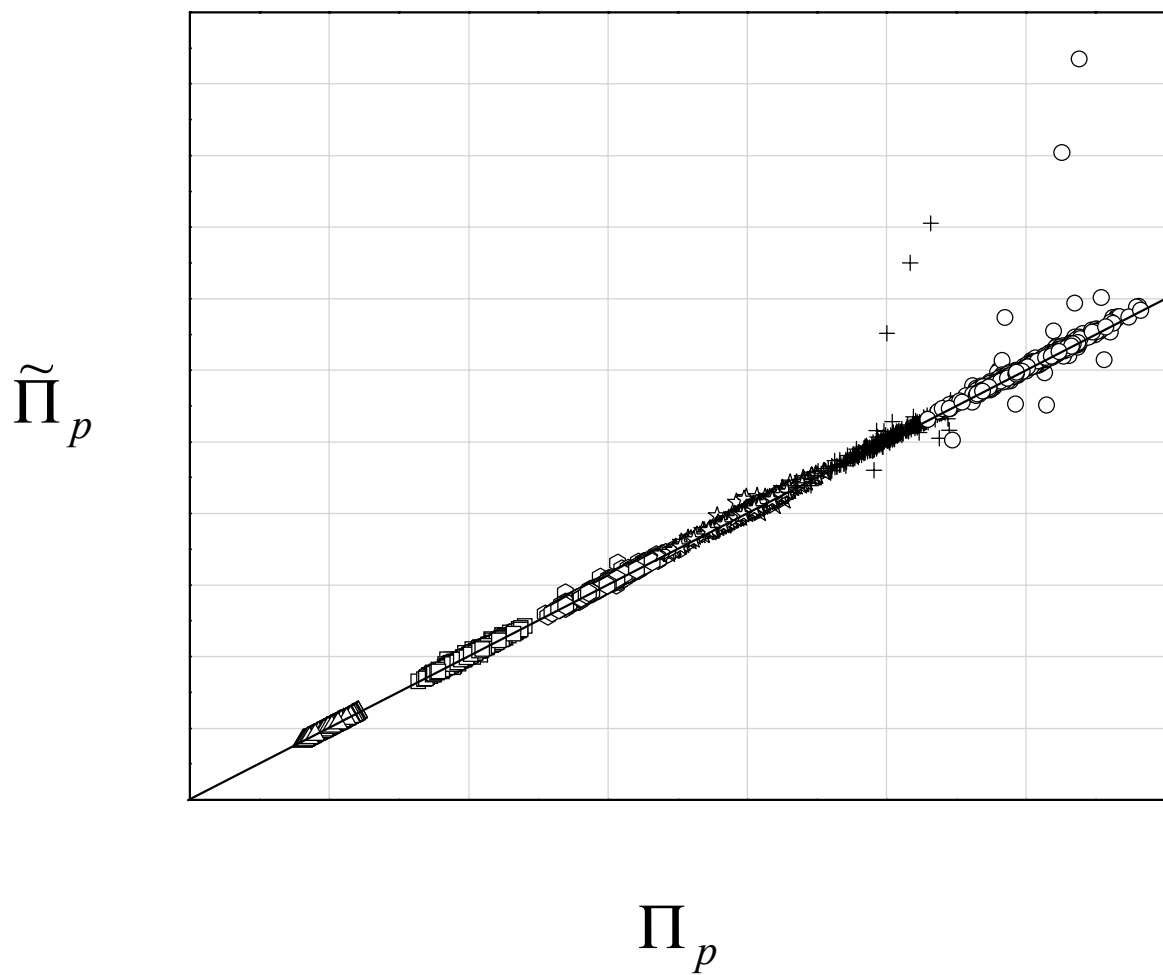


Figure VII-3



$$\alpha = 0.80 \quad \bar{\delta} = 0.04 \quad R = 0.844$$

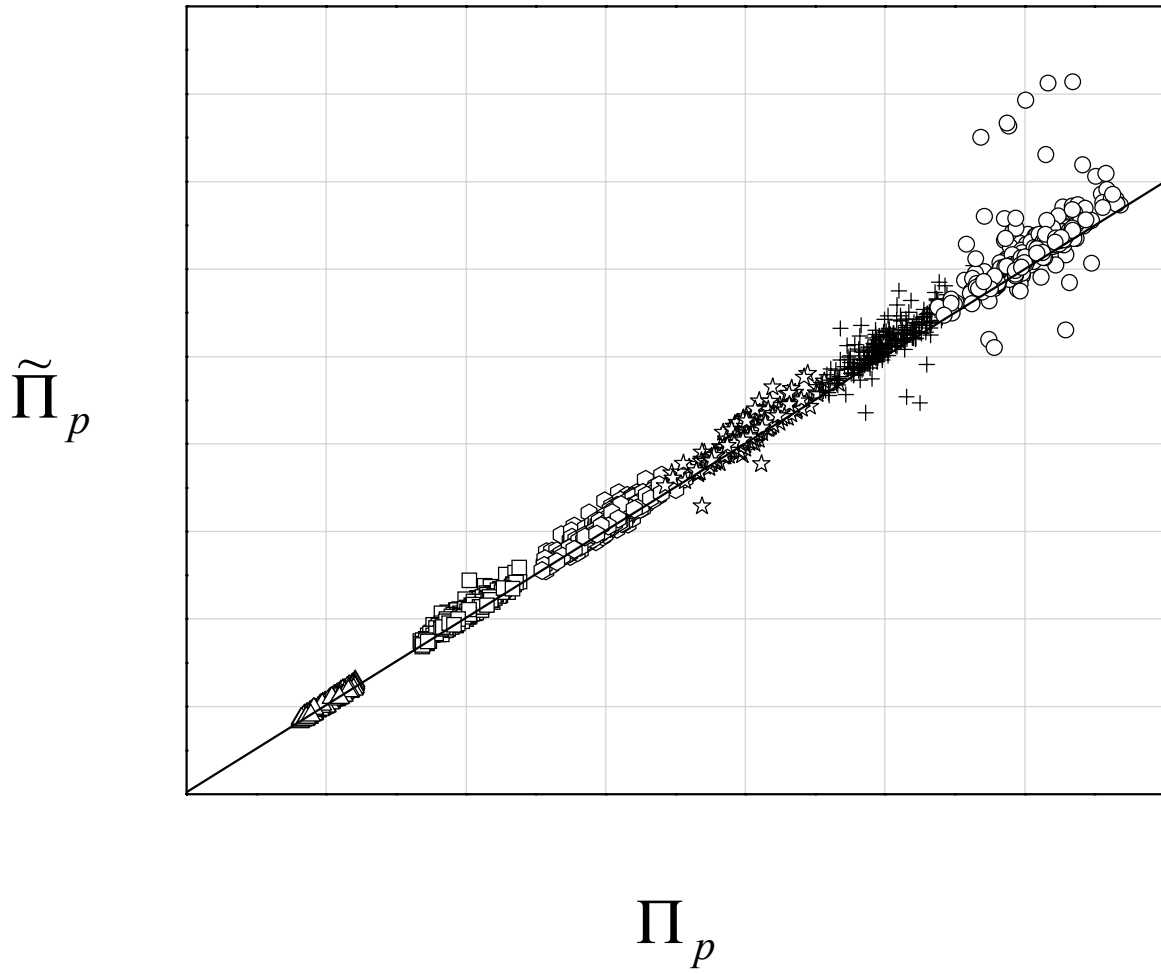


Figure VII-4

$$\alpha = 0.90 \quad \bar{\delta} = 0.04 \quad R = 0.953$$

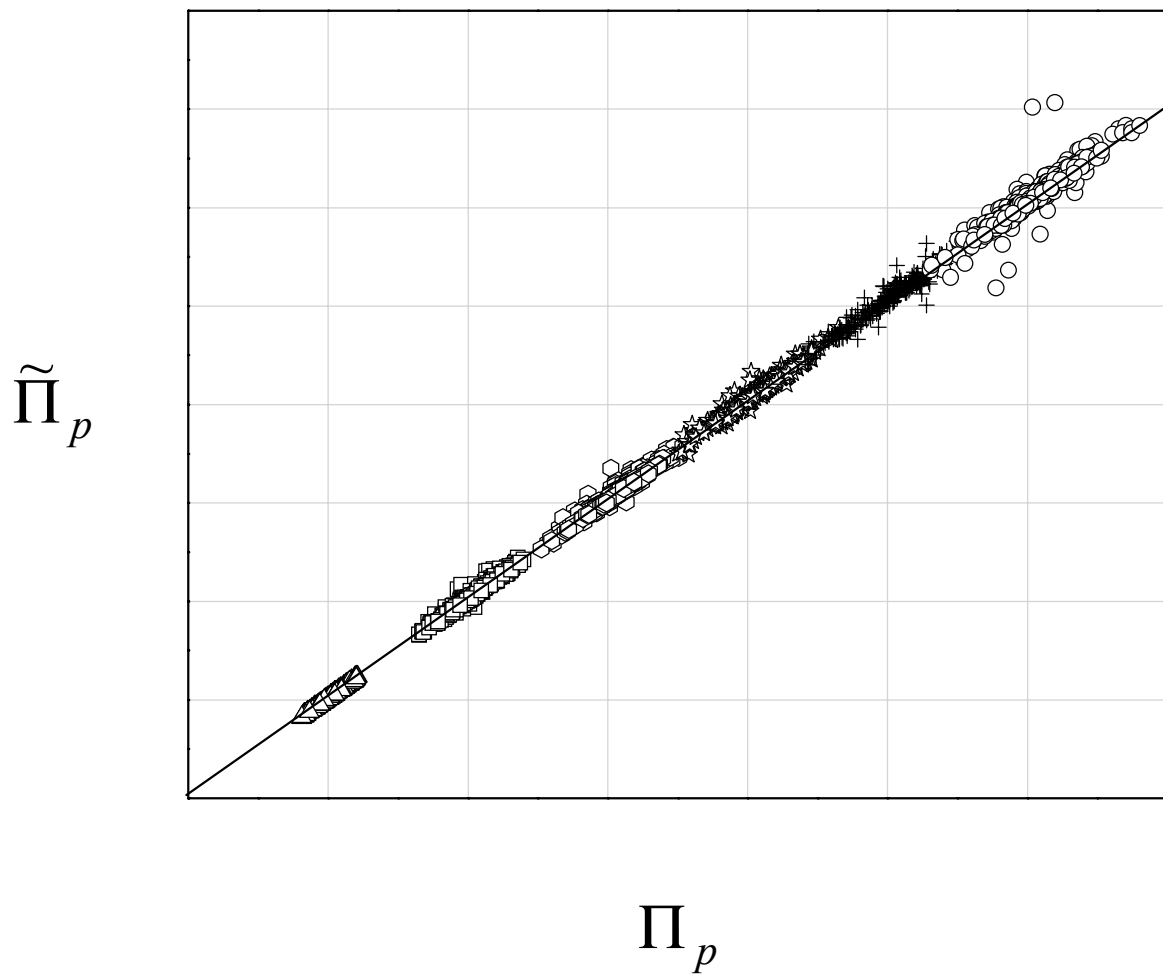


Figure VII-5

$$\alpha = 0.95 \quad \bar{\delta} = 0.04 \quad R = 0.984$$

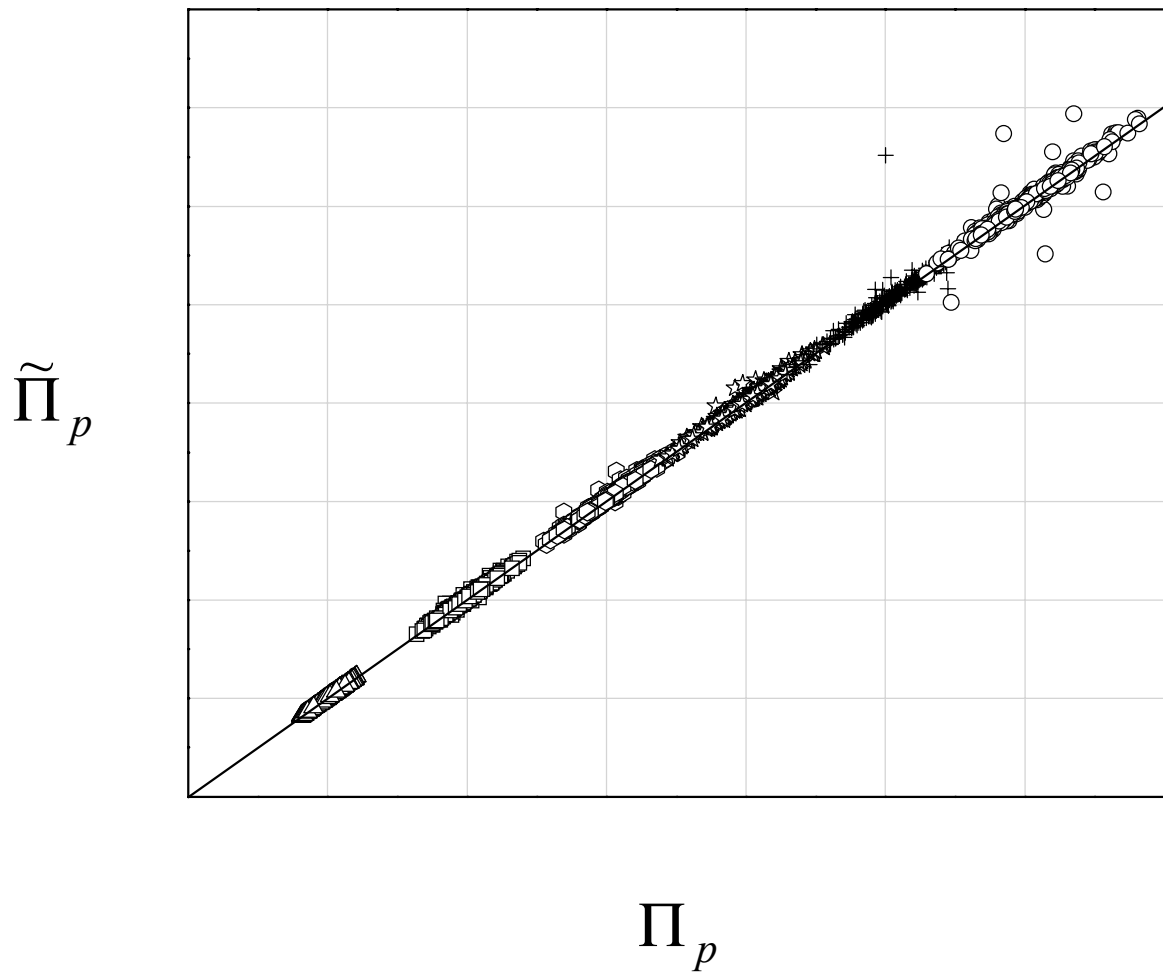


Figure VII-6

$$\alpha = 0.80 \quad \bar{\delta} = 0.02 \quad R = 0.691$$

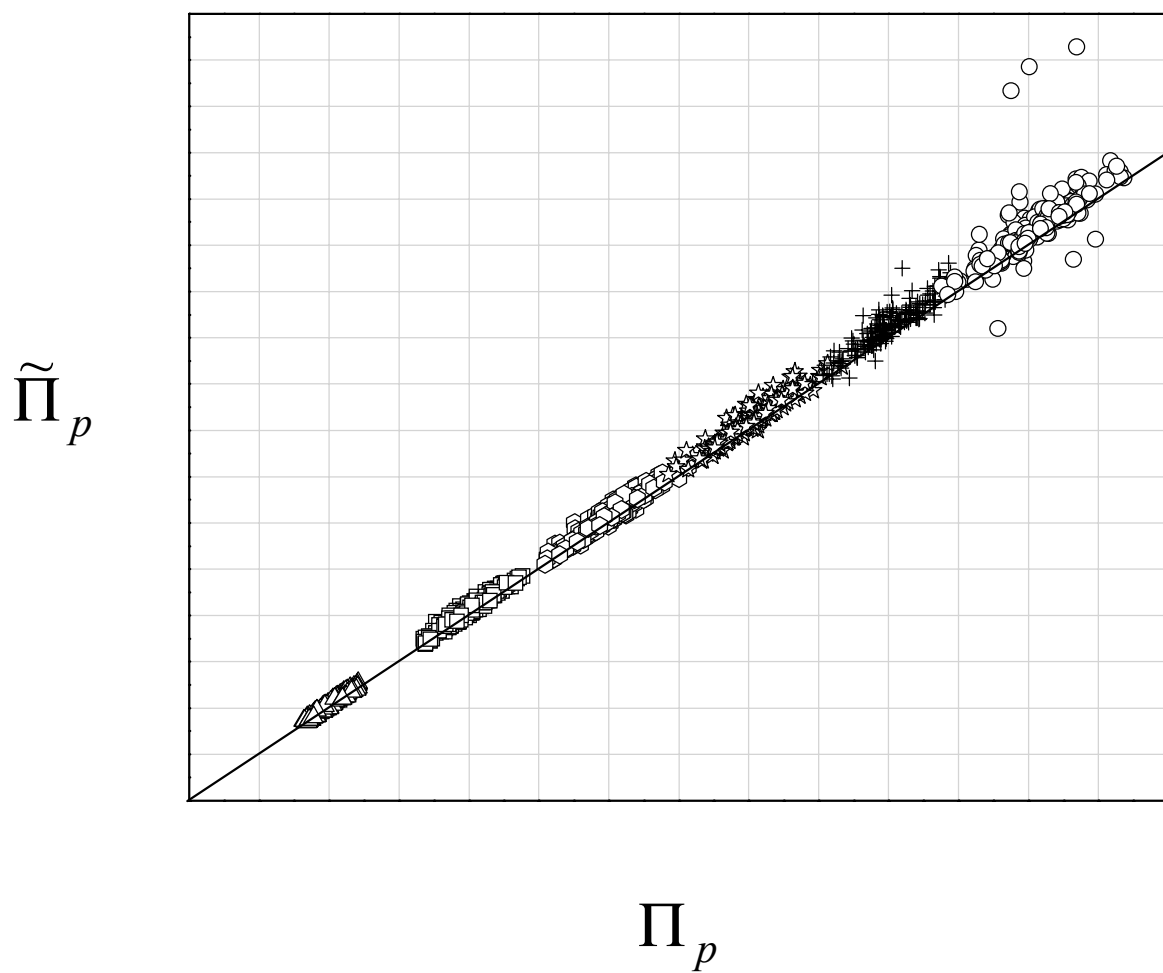


Figure VII-7

$$\alpha = 0.90 \quad \bar{\delta} = 0.02 \quad R = 0.906$$

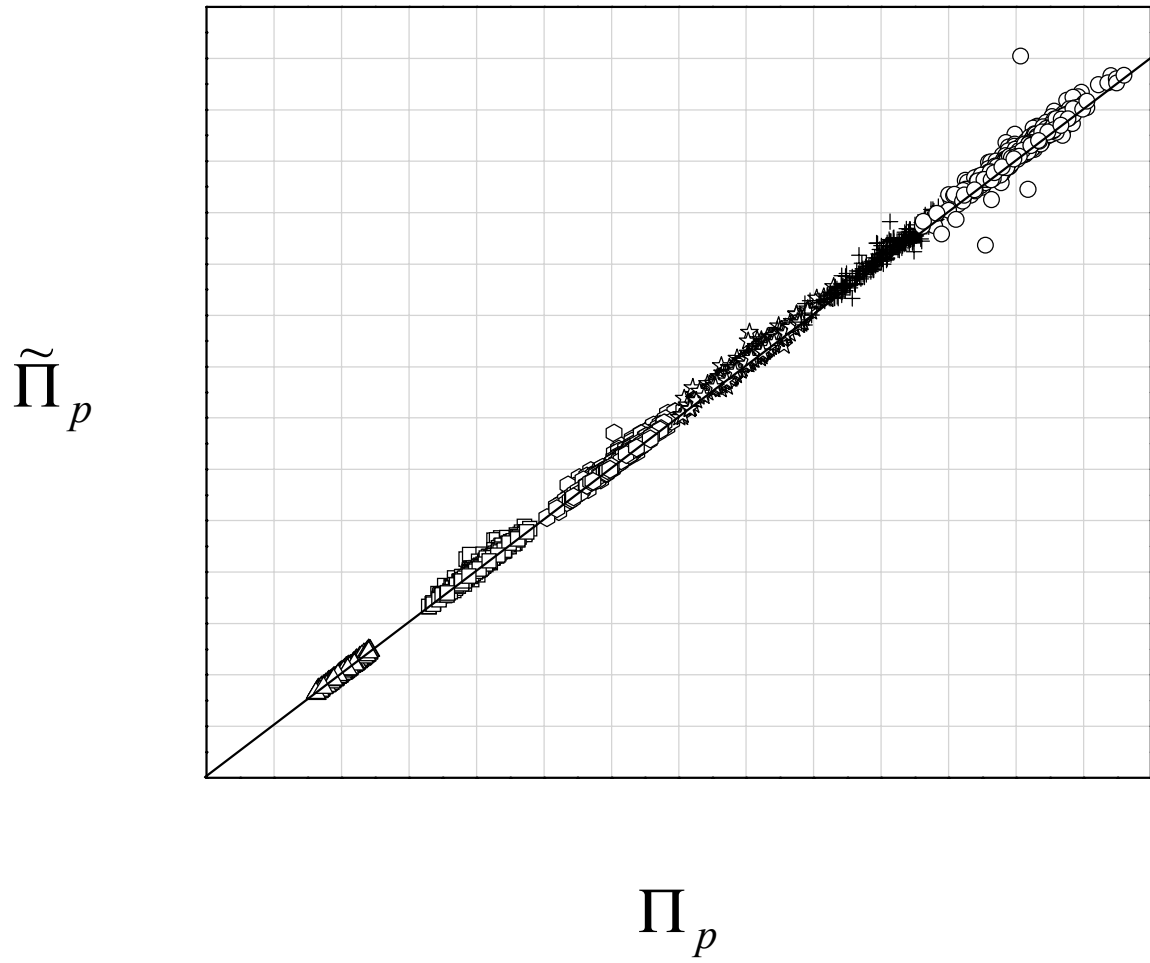


Figure VII-8

$$\alpha = 0.95 \quad \bar{\delta} = 0.02 \quad R = 0.977$$

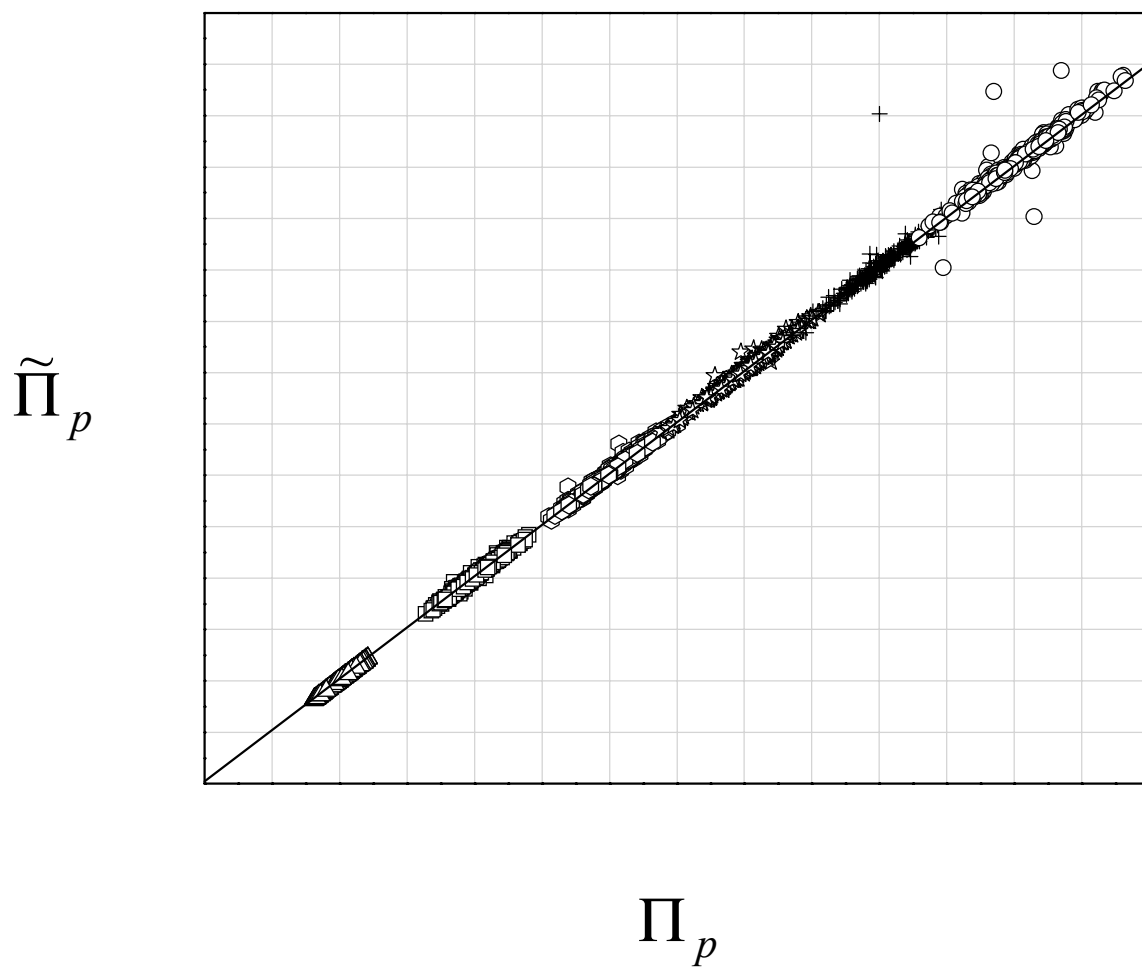


Figure VII-9

$$\alpha = 0.95 \quad \bar{\delta} = 1 \quad R = 1$$

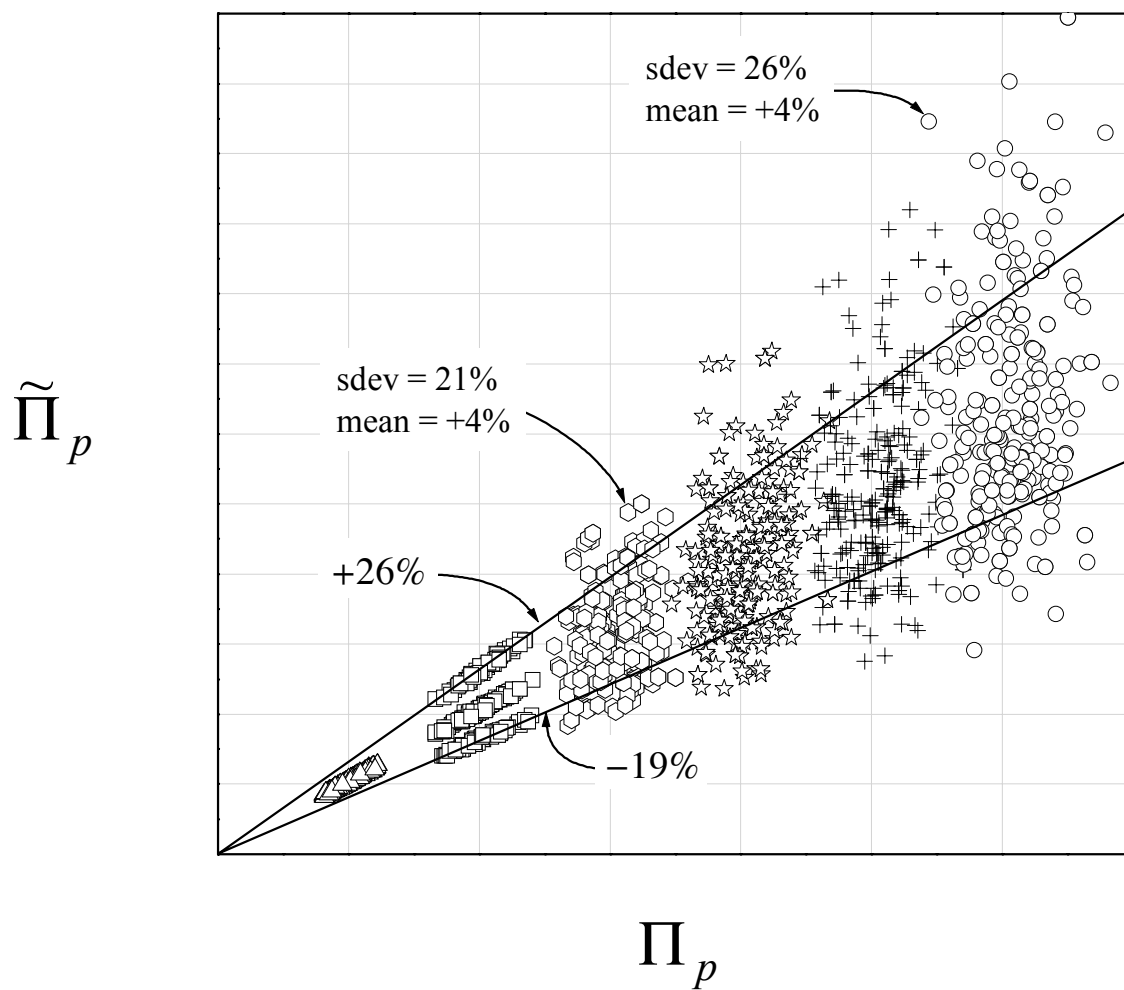


Figure VII-10

## **F. Solid Fuel Distribution**

Acoustically determining the distribution of solid within a cavity is a special case of the cavity boundary characterization discussed in the previous subsection. The specific scenario of interest to the ICF community is to characterize the distribution of solid hydrogens as beta-layering takes place. While this task might be approached from a few different paths (e.g., pulsed acoustic thickness measurements or elastic vibrational response of the shell), the method considered here is that of interpretation of the fluid resonances of the enclosed gas.

The representative ICF capsule at cryogenic temperatures is shown in Appendix M as a highly spherically symmetric object of three clear layers. This picture is idealized in at least three aspects.

First, the capsule will have defects ranging from polish variations to thickness variations to hemishell bonding asymmetries. These aspects of the capsule have already been discussed in some detail.

Second, the solid DT layer must be grown over a period of a few hours under strict temperature conditions (and possibly according to complicated thermodynamic recipes). The basic growth mechanism is that of beta-layering. In this process a confined self-heated solid will redistribute its mass to conform to isotherms. For an ICF capsule the DT is self-heated by beta decay and reabsorption, so that if the capsule surface is held at constant temperature the solid forms a spherically symmetric layer within the cavity. A good starting reference that details this phenomenon is Hoffer and Foreman (1988).

The final solid distribution may reflect the thermal perturbations outside of the capsule during the layer growth. This effect will be softened in proportion to the thermal conductivity of the shell. In most scenarios the capsule is mounted in axially symmetric or spherically symmetric structures. Thus, the thermal perturbations will have similar



symmetry. It can be expected then that the axially symmetric data reduction schemes discussed in the previous subsection may be very useful.

Third, crystal structure of the DT solid is not well understood and is certainly associated with mid- and high-order surface finish perturbations. These perturbations are beyond the reach of the acoustic methods of this report, but they have great importance for ignition success. It is likely, however, that the characterization of the first several deformation modes is indicative of the progress of beta-layering and possibly an estimator of the higher-order mode properties as well.

## APPENDIX A – Spherical Polar Coordinates

This appendix lists several important identities for working with spherical polar coordinates. A good reference for all aspects of spherical polar coordinates is Arfken (1985).

$$\vec{\nabla}\psi = \hat{r}\frac{\partial\psi}{\partial r} + \hat{\theta}\frac{1}{r}\frac{\partial\psi}{\partial\theta} + \hat{\phi}\frac{1}{r\sin\theta}\frac{\partial\psi}{\partial\phi} \quad (\text{A1})$$

$$\vec{\nabla} \cdot \vec{V} = \frac{1}{r^2 \sin\theta} \left[ \frac{\partial}{\partial r} (r^2 \sin\theta V_r) + \frac{\partial}{\partial\theta} (\sin\theta V_\theta) + \frac{\partial}{\partial\phi} (r V_\phi) \right] \quad (\text{A2})$$

$$\vec{\nabla} \times \vec{V} = \frac{1}{r^2 \sin\theta} \begin{vmatrix} \hat{r} & r\hat{\theta} & r\sin\theta\hat{\phi} \\ \frac{\partial}{\partial r} & \frac{\partial}{\partial\theta} & \frac{\partial}{\partial\phi} \\ V_r & rV_\theta & r\sin\theta V_\phi \end{vmatrix} \quad (\text{A3})$$

$$\begin{aligned} \vec{\nabla}^2\psi &= \vec{\nabla} \cdot \vec{\nabla}\psi \\ &= \frac{1}{r^2} \frac{\partial}{\partial r} \left( r^2 \frac{\partial\psi}{\partial r} \right) + \frac{1}{r^2 \sin\theta} \frac{\partial}{\partial\theta} \left( \sin\theta \frac{\partial\psi}{\partial\theta} \right) + \frac{1}{r^2 \sin^2\theta} \frac{\partial^2\psi}{\partial\phi^2} \\ &= \frac{\partial^2\psi}{\partial r^2} + \frac{2}{r} \frac{\partial\psi}{\partial r} + \frac{1}{r^2} \frac{\partial^2\psi}{\partial\theta^2} + \frac{\cos\theta}{r^2 \sin\theta} \frac{\partial\psi}{\partial\theta} + \frac{1}{r^2 \sin^2\theta} \frac{\partial^2\psi}{\partial\phi^2} \end{aligned} \quad (\text{A4})$$

$$\vec{\nabla} \times \hat{r}\psi = \hat{\theta} \frac{1}{r\sin\theta} \frac{\partial\psi}{\partial\phi} - \hat{\phi} \frac{1}{r} \frac{\partial\psi}{\partial\theta} \quad (\text{A5})$$

$$\begin{aligned} \vec{\nabla} \times \vec{\nabla} \times \hat{r}\psi &= \vec{\nabla} \frac{\partial\psi}{\partial r} - \hat{r} \left( \vec{\nabla}^2\psi - \frac{2}{r} \frac{\partial\psi}{\partial r} \right) \\ &= \vec{\nabla} \frac{\partial\psi}{\partial r} - \frac{\partial^2\psi}{\partial r^2} \hat{r} - \vec{\nabla}_t^2\psi \hat{r} \end{aligned} \quad (\text{A6})$$

$$\begin{aligned}
\vec{\nabla}_t \psi &\equiv \vec{\nabla} \psi - \hat{r} \frac{\partial \psi}{\partial r} \\
&= \hat{\theta} \frac{1}{r} \frac{\partial \psi}{\partial \theta} + \hat{\phi} \frac{1}{r \sin \theta} \frac{\partial \psi}{\partial \phi}
\end{aligned} \tag{A7}$$

$$\begin{aligned}
\vec{\nabla}_t^2 \psi &\equiv \vec{\nabla}^2 \psi - \frac{1}{r^2} \frac{\partial}{\partial r} \left( r^2 \frac{\partial \psi}{\partial r} \right) \\
&= \frac{1}{r^2 \sin \theta} \frac{\partial}{\partial \theta} \left( \sin \theta \frac{\partial \psi}{\partial \theta} \right) + \frac{1}{r^2 \sin^2 \theta} \frac{\partial^2 \psi}{\partial \phi^2}
\end{aligned} \tag{A8}$$

$$\hat{n} \bullet \vec{\nabla} = \frac{\vec{\nabla} S}{|\vec{\nabla} S|} \tag{A9}$$

$$|\vec{\mathbf{A}}|^2 = (\vec{\mathbf{A}} \bullet \hat{r})^2 + (\vec{\mathbf{A}} \bullet \hat{\theta})^2 + (\vec{\mathbf{A}} \bullet \hat{\phi})^2 \tag{A10}$$

$$\begin{aligned}
dV &= r^2 dr \sin \theta d\theta d\phi \\
&= r^2 dr d\Omega \\
&= dr dS.
\end{aligned} \tag{A11}$$

Here  $\hat{n}$  is the unit normal to the surface  $S$ ,  $dV$  is the volume element,  $d\Omega$  is the solid angle element,  $dS$  is the surface area element, and  $\psi$  is any scalar function.

## APPENDIX B – Spherical Bessel Functions of the First Kind

The spherical Bessel functions of the first kind are denoted  $j_\ell(z)$  and are solutions of the radial Helmholtz equation in spherical polar coordinates. They are related to the Bessel functions  $J_\ell(z)$  as  $j_\ell(z) = \sqrt{\pi/2z} J_{\ell+1/2}(z)$ . The first few spherical Bessel functions are given below as well as a useful recursion relation for extending this list. An excellent reference for further properties and discussion is Arfken (1985).

$$j_0(z) = \frac{\sin z}{z} \quad (\text{B1})$$

$$j_1(z) = \frac{\sin z}{z^2} - \frac{\cos z}{z} \quad (\text{B2})$$

$$j_2(z) = \left( \frac{3}{z^3} - \frac{1}{z} \right) \sin z - \frac{3}{z^2} \cos z \quad (\text{B3})$$

$$j_3(z) = \left( \frac{15}{z^4} - \frac{6}{z^2} \right) \sin z - \left( \frac{15}{z^3} - \frac{1}{z} \right) \cos z \quad (\text{B4})$$

$$j_4(z) = \left( \frac{105}{z^5} - \frac{45}{z^3} + \frac{1}{z} \right) \sin z - \left( \frac{105}{z^4} - \frac{10}{z^2} \right) \cos z \quad (\text{B5})$$

$$j_5(z) = \left( \frac{945}{z^6} - \frac{420}{z^4} + \frac{15}{z^2} \right) \sin z - \left( \frac{945}{z^5} - \frac{105}{z^3} + \frac{1}{z} \right) \cos z \quad (\text{B6})$$

$$j_6(z) = \left( \frac{12285}{z^7} - \frac{5565}{z^5} + \frac{240}{z^3} - \frac{1}{z} \right) \sin z - \left( \frac{12285}{z^6} - \frac{1470}{z^4} + \frac{23}{z^2} \right) \cos z. \quad (\text{B7})$$

$$j_\ell(z) = \frac{2\ell-1}{z} j_{\ell-1}(z) - j_{\ell-2}(z). \quad (\text{B8})$$

## APPENDIX C – Spherical Harmonic Functions

The spherical harmonic functions are the normalized solutions to Legendre's equation in spherical polar coordinates and are denoted  $Y_{\ell m}(\theta, \phi)$ . In general, each function depends upon both polar and azimuthal coordinate and is described by a polar and azimuthal index pair  $(\ell m)$  where  $\ell$  is a non-negative integer and  $|m| \leq \ell$ . Many of these functions are tabulated below. References for additional properties and discussion include Arfken (1985) and MacRobert (1948).

For  $\ell = 0$ :

$$Y_{00}(\theta, \phi) = +\sqrt{\frac{1}{4\pi}}. \quad (C1)$$

For  $\ell = 1$ :

$$Y_{10}(\theta, \phi) = +\sqrt{\frac{3}{4\pi}} \cos \theta \quad (C2)$$

$$Y_{11}(\theta, \phi) = -\sqrt{\frac{3}{4\pi}} \frac{1}{\sqrt{2}} \sin \theta e^{i\phi}. \quad (C3)$$

For  $\ell = 2$ :

$$Y_{20}(\theta, \phi) = +\sqrt{\frac{5}{4\pi}} \frac{1}{2} (3 \cos^2 \theta - 1) \quad (C4)$$

$$Y_{21}(\theta, \phi) = -\sqrt{\frac{5}{4\pi}} \sqrt{\frac{3}{2}} \sin \theta \cos \theta e^{i\phi} \quad (C5)$$

$$Y_{22}(\theta, \phi) = +\sqrt{\frac{5}{4\pi}} \sqrt{\frac{3}{8}} \sin^2 \theta e^{2i\phi}. \quad (C6)$$

For  $\ell = 3$ :

$$Y_{30}(\theta, \phi) = +\sqrt{\frac{7}{4\pi}} \frac{1}{2} (5 \cos^3 \theta - 3 \cos \theta) \quad (C7)$$

$$Y_{31}(\theta, \phi) = -\sqrt{\frac{7}{4\pi}} \frac{\sqrt{3}}{4} (5 \cos^2 \theta - 1) \sin \theta e^{i\phi} \quad (C8)$$

$$Y_{32}(\theta, \phi) = +\sqrt{\frac{7}{4\pi}} \frac{\sqrt{30}}{4} \cos \theta \sin^2 \theta e^{2i\phi} \quad (C9)$$

$$Y_{33}(\theta, \phi) = -\sqrt{\frac{7}{4\pi}} \frac{\sqrt{5}}{4} \sin^3 \theta e^{3i\phi}. \quad (C10)$$

Some higher-order expressions are

$$Y_{40}(\theta, \phi) = +\sqrt{\frac{9}{4\pi}} \frac{1}{8} (35 \cos^4 \theta - 30 \cos^2 \theta + 3) \quad (C11)$$

$$Y_{41}(\theta, \phi) = -\sqrt{\frac{9}{4\pi}} \frac{\sqrt{5}}{4} (7 \cos^3 \theta - 3 \cos \theta) \sin \theta e^{i\phi} \quad (C12)$$

$$Y_{50}(\theta, \phi) = +\sqrt{\frac{11}{4\pi}} \frac{1}{8} (63 \cos^5 \theta - 70 \cos^3 \theta + 15 \cos \theta) \quad (C13)$$

$$Y_{51}(\theta, \phi) = -\sqrt{\frac{11}{4\pi}} \frac{\sqrt{30}}{16} (21 \cos^4 \theta - 14 \cos^2 \theta + 1) \sin \theta e^{i\phi} \quad (C14)$$

$$Y_{60}(\theta, \phi) = +\sqrt{\frac{13}{4\pi}} \frac{1}{16} (231 \cos^6 \theta - 315 \cos^4 \theta + 105 \cos^2 \theta - 5) \quad (C15)$$

$$Y_{61}(\theta, \phi) = -\sqrt{\frac{13}{4\pi}} \frac{\sqrt{42}}{16} (33 \cos^5 \theta - 30 \cos^3 \theta + 5 \cos \theta) \sin \theta e^{i\phi}. \quad (C16)$$

For obtaining expressions for negative values of  $m$  use the relation

$$Y_{\ell, -m}(\theta, \phi) = (-1)^m e^{-2im\phi} Y_{\ell m}(\theta, \phi). \quad (C17)$$

The spherical harmonic functions are related to the associated Legendre polynomials by the expression.

$$Y_{\ell m}(\theta, \phi) = (-1)^m \sqrt{\frac{2\ell+1}{4\pi} \frac{(\ell-m)!}{(\ell+m)!}} P_{\ell m}(\cos\theta) e^{im\phi}. \quad (\text{C18})$$

Higher-order associated Legendre polynomials can be generated with

$$P_{\ell m}(x) = (-1)^m e^{im\phi} \frac{d^m P_{\ell}(x)}{dx^m}. \quad (\text{C19})$$

Legendre's associated equation is

$$(1-x^2) \frac{\partial^2 P_{\ell m}(x)}{\partial x^2} - 2x \frac{\partial P_{\ell m}(x)}{\partial x} + \ell(\ell+1) P_{\ell m}(x) - \frac{m^2}{1-x^2} P_{\ell m}(x) = 0 \quad (\text{C20})$$

or alternately,

$$\frac{1}{\sin\theta} \frac{\partial}{\partial\theta} \left( \sin\theta \frac{\partial P_{\ell m}(\cos\theta)}{\partial\theta} \right) + \ell(\ell+1) P_{\ell m}(\cos\theta) - \frac{m^2}{\sin^2\theta} P_{\ell m}(\cos\theta) = 0. \quad (\text{C21})$$

Equations (C21), (C18), and (A7) show that

$$r^2 \vec{\nabla}_t^2 Y_{\ell m}(\theta, \phi) = -\ell(\ell+1) Y_{\ell m}(\theta, \phi). \quad (\text{C22})$$

## APPENDIX D – Roots of the Spherical Bessel Functions and Their Derivatives

The following table lists many of the lowest-order roots  $z_{\ell s}$  of the expression

$$j_{\ell}(z)=0 \tag{D1}$$

where  $\ell$  is the order of the spherical Bessel function and the index  $s$  enumerates the roots beginning at the fundamental ( $s = 0$ ) and proceeding through the overtones ( $s > 0$ ). The  $\ell = 0$  roots are the integer multiples of  $\pi$ .

Table D1

	s = 0	s = 1	s = 2	s = 3	s = 4
$\ell = 0$	3.14159265	6.28318531	9.42477796	12.56637061	15.70796327
$\ell = 1$	4.49340946	7.72525184	10.90412166	14.06619391	17.02207553
$\ell = 2$	5.76345920	9.09501133	12.32294097	15.51460301	18.68903636
$\ell = 3$	6.98793200	10.41711855	13.69802315	16.92362129	20.12180617
$\ell = 4$	8.18256145	11.70490715	15.03966471	18.30125596	21.52541773
$\ell = 5$	9.35581211	12.96653017	16.35470964	19.65315210	22.90455065
$\ell = 6$	10.51283541	14.20739246	17.64797487	20.98346307	24.26276804
$\ell = 7$	11.65703219	15.43128921	18.92299920	22.29534802	25.60285595
$\ell = 8$	12.79078171	16.64100288	20.18247076	23.59127482	26.92704078
$\ell = 9$	13.91582261	17.83864320	21.42848697	24.87321392	28.23713436



The following table lists many of the lowest-order roots  $z_{\ell s}$  of the expression

$$j'_\ell(z) \equiv \frac{\partial j_\ell(z)}{\partial z} = 0 \quad (\text{D2})$$

where  $\ell$  is the order of the spherical Bessel function and the index  $s$  enumerates the roots beginning at the fundamental ( $s = 0$ ) and proceeding through the overtones ( $s > 0$ ).

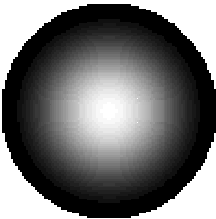
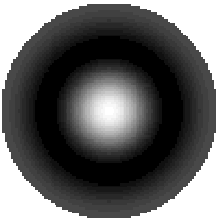
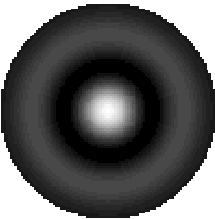
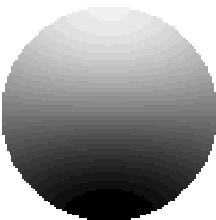
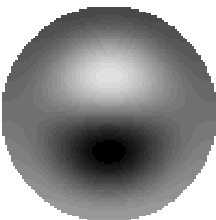
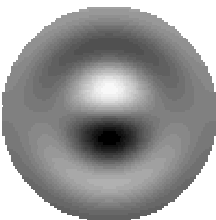
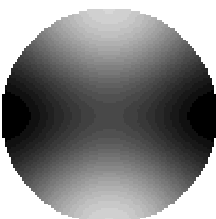
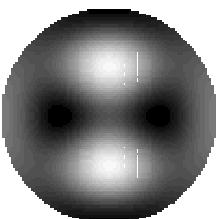
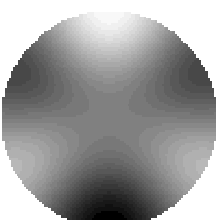
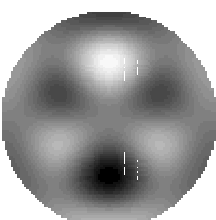
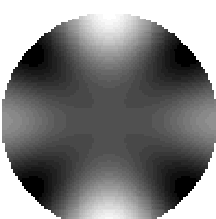
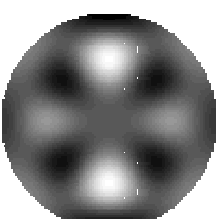
Table D2

	s = 0	s = 1	s = 2	s = 3	s = 4
$\ell = 0$	0.00000000	4.49340946	7.72525184	10.90412166	14.06619391
$\ell = 1$	2.08157598	5.94036999	9.20584014	12.40444502	15.57923641
$\ell = 2$	3.34209366	7.28993230	10.60385504	13.84611188	17.04290219
$\ell = 3$	4.51409965	8.58375496	11.97273003	15.24451382	18.46814778
$\ell = 4$	5.64670362	9.84044604	13.29556386	16.60934590	19.86242396
$\ell = 5$	6.75645633	11.07020687	14.59055216	17.94717953	21.23106830
$\ell = 6$	7.85107768	12.27933398	15.86322182	19.26270994	22.57805807
$\ell = 7$	8.93483888	13.47203035	17.11750573	20.55942813	23.90644997
$\ell = 8$	10.01037075	14.65126281	18.35631834	21.84001208	25.21865244
$\ell = 9$	11.07941839	15.81921549	19.58188902	23.10656842	26.51660256

**APPENDIX E – Axisymmetric Fluid Resonance Representations**

The following table displays pressure distribution gray-scale representations of several low-order mode resonances. For a detailed discussion see the main text.

Table E1

	$s = 0$	$s = 1$	$s = 2$	$s = 3$
$\ell = 0$ “monopole”	no solution			
$\ell = 1$ “dipole”				
$\ell = 2$ “quadrupole”				
$\ell = 3$ “hexapole”				
$\ell = 4$ “octopole”				

## APPENDIX F – Useful Mathematical Relations

The following series expansions and identities are used to derive many of the results in the main text.

$$f(a+h) = f(a) + hf'(a) + \frac{h^2}{2!} f''(a) + \frac{h^3}{3!} f'''(a) + \dots \quad (\text{F1})$$

$$(1+x)^n = 1 + nx + \frac{n(n-1)}{2!} x^2 + \frac{n(n-1)(n-2)}{3!} x^3 + \dots \quad (x^2 < 1) \quad (\text{F2})$$

$$\int_a^b u \, dv = (uv) \Big|_a^b - \int_a^b v \, du \quad (\text{F3})$$

$$z^2 j_\ell''(z) + 2z j_\ell'(z) + [z^2 - \ell(\ell+1)] j_\ell(z) = 0 \quad (\text{F4})$$

$$(1-x^2) \frac{d^2}{dx^2} P_{\ell m}(x) - 2x \frac{d}{dx} P_{\ell m}(x) + \left[ \ell(\ell+1) - \frac{m^2}{1-x^2} \right] P_{\ell m}(x) = 0 \quad (\text{F5})$$

$$(\ell+1)P_\ell(x) = P_{\ell+1}'(x) - xP_\ell'(x) \quad (\text{F6})$$

$$(2\ell+1)P_\ell(x) = P_{\ell+1}'(x) - P_{\ell-1}'(x) \quad (\text{F7})$$

$$(2\ell+1)(1-x^2)^{1/2} P_{\ell m}(x) = P_{\ell+1,m+1}(x) - P_{\ell-1,m+1}(x) \quad (\text{F8})$$

$$P_\ell(x=0) = (-1)^{\ell/2} \frac{(\ell-1)!!}{\ell!!} \quad \{\ell \text{ even}\} \quad (\text{F9})$$

## APPENDIX G – Clebsch-Gordan Coefficients

This appendix tabulates Clebsch-Gordan Coefficients used in the boundary perturbation calculations presented in Section III. The relevant coefficients are of the form  $C(\ell p \ell; m q m')$  and vanish unless  $m' = m + q$  and  $p \leq 2\ell$ . One additional constraints of the calculations require that  $p > 0$  is even and that  $|q| \leq p$ . The tables below also list the  $\tilde{C}$  coefficients defined by  $\tilde{C}(\ell, p, \ell; m, q, m') \equiv C(\ell, p, \ell; m, q, m') C(\ell, p, \ell; 0, 0, 0)$ . These calculations can be performed by a mathematics solver package or through standard formulae such as given by Rose (1957) and others.

Table G1

$\ell = 1; p = 2$		
$(m, m')$	$C$	$\tilde{C}$
(0,0)	$-\sqrt{\frac{2}{5}}$	$\frac{2}{5}$
(-1,-1) (1,1)	$\sqrt{\frac{1}{10}}$	$-\frac{1}{5}$
(-1,0) (1,0)	$\sqrt{\frac{3}{10}}$	$-\frac{\sqrt{3}}{5}$
(-1,1) (1,-1)	$\sqrt{\frac{3}{5}}$	$-\frac{\sqrt{6}}{5}$
(0,-1) (0,1)	$-\sqrt{\frac{3}{10}}$	$\frac{\sqrt{3}}{5}$

Table G2

$\ell = 2 ; p = 2$		
$(m, m')$	$C$	$\tilde{C}$
$(0,0)$	$-\sqrt{\frac{2}{7}}$	$\frac{2}{7}$
$(-2,-2) (-2,0) (0,-2)$ $(0,2) (2,0) (2,2)$	$\sqrt{\frac{2}{7}}$	$-\frac{2}{7}$
$(-2,-1) (-1,1) (1,-1) (2,1)$	$\sqrt{\frac{3}{7}}$	$-\frac{\sqrt{6}}{7}$
$(-1,-2) (1,2)$	$-\sqrt{\frac{3}{7}}$	$\frac{\sqrt{6}}{7}$
$(-1,-1) (0,-1) (0,1) (1,1)$	$-\sqrt{\frac{1}{14}}$	$\frac{1}{7}$
$(-1,0) (1,0)$	$\sqrt{\frac{1}{14}}$	$-\frac{1}{7}$

Table G3

$\ell = 2 ; p = 4$		
$(m, m')$	$C$	$\tilde{C}$
(0,0)	$\sqrt{\frac{2}{7}}$	$\frac{2}{7}$
(-2,-2) (2,2)	$\frac{1}{3} \sqrt{\frac{1}{14}}$	$\frac{1}{21}$
(-2,-1) (2,1)	$\frac{1}{3} \sqrt{\frac{5}{14}}$	$\frac{\sqrt{5}}{21}$
(-2,0) (0,-2) (0,2) (2,0)	$\sqrt{\frac{5}{42}}$	$\frac{1}{7} \sqrt{\frac{5}{3}}$
(-2,-1) (2,-1)	$\frac{1}{3} \sqrt{\frac{5}{2}}$	$\frac{1}{3} \sqrt{\frac{5}{7}}$
(-2,2) (2,-2)	$\frac{\sqrt{5}}{3}$	$\frac{1}{3} \sqrt{\frac{10}{7}}$
(-1,-2) (1,2)	$-\frac{1}{3} \sqrt{\frac{5}{14}}$	$-\frac{\sqrt{5}}{21}$
(-1,-1) (1,1)	$-\frac{2}{3} \sqrt{\frac{2}{7}}$	$-\frac{4}{21}$
(-1,0) (1,0)	$-\sqrt{\frac{5}{21}}$	$-\frac{1}{7} \sqrt{\frac{10}{3}}$
(-1,1) (1,-1)	$-\frac{2}{3} \sqrt{\frac{5}{7}}$	$-\frac{2\sqrt{10}}{21}$
(-1,2) (1,-2)	$-\frac{1}{3} \sqrt{\frac{5}{2}}$	$-\frac{1}{3} \sqrt{\frac{5}{7}}$
(0,-1) (0,1)	$\sqrt{\frac{5}{21}}$	$\frac{1}{7} \sqrt{\frac{10}{3}}$

Higher-order coefficients are tabulated only for axisymmetric calculations for which  $m = m'$ .

Table G4

$\ell = 3; m = m'$		
$(\ell, p,  m )$	$C$	$\tilde{C}$
(3,2,0)	$-\frac{2}{\sqrt{15}}$	$\frac{4}{15}$
(3,2,1)	$-\frac{1}{2}\sqrt{\frac{3}{5}}$	$\frac{1}{5}$
(3,2,2)	0	0
(3,2,3)	$\frac{1}{2}\sqrt{\frac{5}{3}}$	$-\frac{1}{3}$
(3,4,0)	$\sqrt{\frac{2}{11}}$	$\frac{2}{11}$
(3,4,1)	$\frac{1}{3\sqrt{22}}$	$\frac{1}{33}$
(3,4,2)	$-\frac{7}{3\sqrt{22}}$	$-\frac{7}{33}$
(3,4,3)	$\frac{1}{\sqrt{22}}$	$\frac{1}{11}$
(3,6,0)	$-\frac{10}{\sqrt{429}}$	$\frac{100}{429}$
(3,6,1)	$\frac{5}{2}\sqrt{\frac{3}{143}}$	$-\frac{25}{143}$
(3,6,2)	$-\sqrt{\frac{3}{143}}$	$\frac{10}{143}$
(3,6,3)	$\frac{1}{2\sqrt{429}}$	$-\frac{5}{429}$

Table G5

$\ell = 4; m = m'$		
$(\ell, p,  m )$	$C$	$\tilde{C}$
(4,2,0)	$-2\sqrt{5/77}$	20/77
(4,2,1)	$-17/2\sqrt{385}$	17/77
(4,2,2)	$-4/\sqrt{385}$	8/77
(4,2,3)	$\sqrt{7/220}$	-1/11
(4,2,4)	$2\sqrt{7/55}$	-4/11
(4,4,0)	$9\sqrt{2/1001}$	162/1001
(4,4,1)	$9/\sqrt{2002}$	81/1001
(4,4,2)	$-\sqrt{11/182}$	-9/91
(4,4,3)	$-3\sqrt{7/286}$	-27/143
(4,4,4)	$\sqrt{14/143}$	18/143
(4,6,0)	$-2\sqrt{5/143}$	20/143
(4,6,1)	$1/2\sqrt{715}$	-1/143
(4,6,2)	$\sqrt{11/65}$	-2/13
(4,6,3)	$-17/2\sqrt{715}$	17/143
(4,6,4)	$2/\sqrt{715}$	-4/143
(4,8,0)	$7\sqrt{10/2431}$	490/2431
(4,8,1)	$-28\sqrt{2/12155}$	-392/2431
(4,8,2)	$14\sqrt{2/12155}$	196/2431
(4,8,3)	$-4\sqrt{2/12155}$	-56/2431
(4,8,4)	$1/\sqrt{24310}$	7/2431



Table G6

$\ell = 5; m = m'$		
$(\ell, p,  m )$	$C$	$\tilde{C}$
(5,2,0)	$-\sqrt{10/39}$	10/39
(5,2,1)	$-3\sqrt{3/130}$	3/13
(5,2,2)	$-\sqrt{6/65}$	2/13
(5,2,3)	$-1/\sqrt{390}$	1/39
(5,2,4)	$\sqrt{6/65}$	$-2/13$
(5,2,5)	$\sqrt{15/26}$	$-5/13$
(5,4,0)	$\sqrt{2/13}$	2/13
(5,4,1)	$2\sqrt{2/117}$	4/39
(5,4,2)	$-1/3\sqrt{26}$	$-1/39$
(5,4,3)	$-\sqrt{2/13}$	$-2/13$
(5,4,4)	$-\sqrt{2/13}$	$-2/13$
(5,4,5)	$\sqrt{2/13}$	2/13
(5,6,0)	$-4\sqrt{5/663}$	80/663
(5,6,1)	$-2\sqrt{3/1105}$	8/221
(5,6,2)	$6\sqrt{3/1105}$	$-24/221$
(5,6,3)	$29/2\sqrt{3315}$	$-58/663$
(5,6,4)	$-8\sqrt{3/1105}$	32/221
(5,6,5)	$\sqrt{15/884}$	$-10/221$
(5,8,0)	$7\sqrt{10/4199}$	490/4199
(5,8,1)	$-7\sqrt{2/20995}$	$-98/4199$
(5,8,2)	$-2\sqrt{34/1235}$	$-28/247$
(5,8,3)	$73/\sqrt{41990}$	511/4199

Table G6 cont.

$\ell = 5; m = m'$		
$(\ell, p,  m )$	$C$	$\tilde{C}$
(5,8,4)	$-31/\sqrt{41990}$	$-217/4199$
(5,8,5)	$\sqrt{5/8398}$	$35/4199$
(5,10,0)	$-6\sqrt{21/4199}$	$756/4199$
(5,10,1)	$5\sqrt{21/4199}$	$-630/4199$
(5,10,2)	$-20\sqrt{3/29393}$	$360/4199$
(5,10,3)	$15\sqrt{3/117572}$	$-135/4199$
(5,10,4)	$-5/\sqrt{88179}$	$30/4199$
(5,10,5)	$1/2\sqrt{88179}$	$-3/4199$

Table G7

$\ell = 6; m = m'$		
$(\ell, p,  m )$	$C$	$\tilde{C}$
(6,2,0)	$-\sqrt{14/55}$	14/55
(6,2,1)	$-13/\sqrt{770}$	13/55
(6,2,2)	$-\sqrt{10/77}$	2/11
(6,2,3)	$-\sqrt{5/154}$	1/11
(6,2,4)	$\sqrt{2/385}$	$-2/55$
(6,2,5)	$\sqrt{11/70}$	$-1/5$
(6,2,6)	$\sqrt{22/35}$	$-2/5$
(6,4,0)	$2\sqrt{7/187}$	28/187
(6,4,1)	$32/\sqrt{11781}$	64/561
(6,4,2)	$\sqrt{11/4284}$	1/51
(6,4,3)	$-9/\sqrt{1309}$	$-18/187$
(6,4,4)	$-16/\sqrt{1309}$	$-32/187$
(6,4,5)	$-\sqrt{11/119}$	$-2/17$
(6,4,6)	$3\sqrt{11/476}$	3/17
(6,6,0)	$-20/\sqrt{3553}$	400/3553
(6,6,1)	$-10/\sqrt{3553}$	200/3553
(6,6,2)	$\sqrt{11/323}$	$-20/323$
(6,6,3)	$43/\sqrt{14212}$	$-430/3553$
(6,6,4)	$4/\sqrt{3553}$	$-80/3553$
(6,6,5)	$-5\sqrt{11/1292}$	50/3553
(6,6,6)	$\sqrt{11/323}$	$-20/323$
(6,8,0)	$5\sqrt{14/3553}$	350/3553

Table G7 cont.

$\ell = 6; m = m'$		
$(\ell, p,  m )$	$C$	$\tilde{C}$
(6,8,1)	$5\sqrt{2/24871}$	50/3553
(6,8,2)	$-71/\sqrt{49742}$	$-355/3553$
(6,8,3)	$-\sqrt{19/2618}$	$-5/187$
(6,8,4)	$89/\sqrt{49742}$	445/3553
(6,8,5)	$-5\sqrt{11/4522}$	$-25/323$
(6,8,6)	$\sqrt{11/4522}$	5/323
(6,10,0)	$-6\sqrt{21/7429}$	756/7429
(6,10,1)	$13\sqrt{3/52003}$	$-234/7429$
(6,10,2)	$5\sqrt{21/7429}$	$-630/7429$
(6,10,3)	$-5\sqrt{57/10948}$	45/391
(6,10,4)	$83/\sqrt{156009}$	$-498/7429$
(6,10,5)	$-7\sqrt{7/89148}$	147/7429
(6,10,6)	$\sqrt{3/52003}$	$-18/7429$
(6,12,0)	$66\sqrt{7/185725}$	30492/185725
(6,12,1)	$-396/\sqrt{1300075}$	$-26136/185725$
(6,12,2)	$99/\sqrt{208012}$	3267/37145
(6,12,3)	$-22/\sqrt{52003}$	$-1452/37145$
(6,12,4)	$33/\sqrt{1300075}$	2178/185725
(6,12,5)	$-6/\sqrt{130005}$	$-396/185725$
(6,12,6)	$1/\sqrt{5200300}$	33/185725

## APPENDIX H – B Matrices and Eigenvalues

The **B** matrices are given by

$$\mathbf{B}_{mm'}^{\ell s} = \sum_{\substack{p=2 \\ \text{even}}}^{2\ell} K_{\ell ps} \tilde{C}(\ell p \ell; m q m') c_{pq} \quad (\text{H1})$$

which is equation (106). The K coefficients are defined as

$$K_{\ell ps} \equiv \sqrt{\frac{2p+1}{4\pi}} \left( \frac{z_{\ell s}^2 - \ell(\ell+1) + \frac{1}{2}p(p+1)}{z_{\ell s}^2 - \ell(\ell+1)} \right) \quad (\text{H2})$$

which is equation (107). These coefficients are of order unity unless  $p$  is very large. For very large overtone number ( $s \rightarrow \infty$ )  $K$  approaches the square root term for all  $\ell$  values.

The general matrices for  $\ell=1$  and  $\ell=2$  are:

$$\mathbf{B}^{1s} = \frac{K_{12s}}{5} \begin{bmatrix} -c_{20} & -\sqrt{3}c_{21} & -\sqrt{6}c_{22} \\ -\sqrt{3}c_{21} & +2c_{20} & +\sqrt{3}c_{21} \\ -\sqrt{6}c_{22} & +\sqrt{3}c_{21} & -c_{20} \end{bmatrix} \quad (\text{H3})$$

$$\mathbf{B}^{2s} = \frac{1}{21} \begin{bmatrix} -6K_{22s}c_{20} + K_{24s}c_{40} & -3\sqrt{6}K_{22s}c_{21} + \sqrt{5}K_{24s}c_{41} & -6K_{22s}c_{22} + \sqrt{15}K_{24s}c_{42} & \sqrt{35}K_{24s}c_{43} & \sqrt{70}K_{24s}c_{44} \\ -3\sqrt{6}K_{22s}c_{21} + \sqrt{5}K_{24s}c_{41} & 3K_{22s}c_{20} - 4K_{24s}c_{40} & -3K_{22s}c_{21} - \sqrt{30}K_{24s}c_{41} & -3\sqrt{6}K_{22s}c_{22} - 2\sqrt{10}K_{24s}c_{42} & -\sqrt{35}K_{24s}c_{43} \\ -6K_{22s}c_{22} + \sqrt{15}K_{24s}c_{42} & -3K_{22s}c_{21} - \sqrt{30}K_{24s}c_{41} & 6K_{22s}c_{20} + 6K_{24s}c_{40} & 3K_{22s}c_{21} + \sqrt{30}K_{24s}c_{41} & 6K_{22s}c_{22} - \sqrt{15}K_{24s}c_{42} \\ \sqrt{35}K_{24s}c_{43} & -3\sqrt{6}K_{22s}c_{22} - 2\sqrt{10}K_{24s}c_{42} & 3K_{22s}c_{21} + \sqrt{30}K_{24s}c_{41} & 3K_{22s}c_{20} - 4K_{24s}c_{40} & 3\sqrt{6}K_{22s}c_{21} - \sqrt{5}K_{24s}c_{41} \\ \sqrt{70}K_{24s}c_{44} & -\sqrt{35}K_{24s}c_{43} & 6K_{22s}c_{22} - \sqrt{15}K_{24s}c_{42} & 3\sqrt{6}K_{22s}c_{21} - \sqrt{5}K_{24s}c_{41} & -6K_{22s}c_{20} + K_{24s}c_{40} \end{bmatrix} \quad (\text{H4})$$

and higher-order matrices quickly become cumbersome and are not reproduced here.

The eigenvalues of  $\mathbf{B}^{1s}$  are

$$\Lambda^{1s} = \left\{ \begin{array}{l} -\frac{K_{12s}}{5} (c_{20} + \sqrt{6}c_{22}) \\ \frac{K_{12s}}{10} \left( c_{20} + \sqrt{6}c_{22} + \sqrt{(3c_{20} - \sqrt{6}c_{22})^2 + 24c_{21}^2} \right) \\ \frac{K_{12s}}{10} \left( c_{20} + \sqrt{6}c_{22} - \sqrt{(3c_{20} - \sqrt{6}c_{22})^2 + 24c_{21}^2} \right) \end{array} \right\}. \quad (\text{H5})$$

The eigenvalues for axisymmetric perturbations ( $q=0$ ) up to  $\ell=6$  are given below. Notice that the number of distinct eigenvalues is  $\ell+1$  instead of the maximum possible  $2\ell+1$ . As listed above, each expression represents a doubly degenerate eigenvalue except the first in each set, which is nondegenerate. Taking this degeneracy into account, the eigenvalues for each set sum to zero.

$$5 \Lambda^{1s} = \left\{ \begin{array}{l} 2K_{12s}c_{20} \\ -K_{12s}c_{20} \end{array} \right\} \quad (\text{H6})$$

$$21 \Lambda^{2s} = \left\{ \begin{array}{l} 6K_{22s}c_{20} + 6K_{24s}c_{40} \\ 3K_{22s}c_{20} - 4K_{24s}c_{40} \\ -6K_{22s}c_{20} + K_{24s}c_{40} \end{array} \right\} \quad (\text{H7})$$

$$2145 \Lambda^{3s} = \left\{ \begin{array}{l} 572K_{32s}c_{20} + 390K_{34s}c_{40} + 500K_{36s}c_{60} \\ 429K_{32s}c_{20} + 65K_{34s}c_{40} - 375K_{36s}c_{60} \\ -455K_{34s}c_{40} + 150K_{36s}c_{60} \\ -715K_{32s}c_{20} + 195K_{34s}c_{40} - 25K_{36s}c_{60} \end{array} \right\} \quad (\text{H8})$$

$$17017 \Lambda^{4s} = \left\{ \begin{array}{l} 4420K_{42s}c_{20} + 2754K_{44s}c_{40} + 2380K_{46s}c_{60} + 3430K_{48s}c_{80} \\ 3757K_{42s}c_{20} + 1377K_{44s}c_{40} - 119K_{46s}c_{60} - 2744K_{48s}c_{80} \\ 1768K_{42s}c_{20} - 1683K_{44s}c_{40} - 2618K_{46s}c_{60} + 1372K_{48s}c_{80} \\ -1547K_{42s}c_{20} - 3213K_{44s}c_{40} + 2023K_{46s}c_{60} - 392K_{48s}c_{80} \\ -6188K_{42s}c_{20} + 2142K_{44s}c_{40} - 476K_{46s}c_{60} + 49K_{48s}c_{80} \end{array} \right\} \quad (\text{H9})$$

$$12597\Lambda^{5s} = \left\{ \begin{array}{l} 3230K_{52s}c_{20} + 1938K_{54s}c_{40} + 1520K_{56s}c_{60} \\ + 1470K_{58s}c_{80} + 2268K_{5,10,s}c_{10,0} \\ \hline 2907K_{52s}c_{20} + 1297K_{54s}c_{40} + 456K_{56s}c_{60} \\ - 294K_{58s}c_{80} - 1890K_{5,10,s}c_{10,0} \\ \hline 1938K_{52s}c_{20} - 323K_{54s}c_{40} - 1368K_{56s}c_{60} \\ - 1428K_{58s}c_{80} + 1080K_{5,10,s}c_{10,0} \\ \hline 323K_{52s}c_{20} - 646K_{54s}c_{40} - 1102K_{56s}c_{60} \\ + 1533K_{58s}c_{80} - 405K_{5,10,s}c_{10,0} \\ \hline -1938K_{52s}c_{20} - 646K_{54s}c_{40} + 1824K_{56s}c_{60} \\ - 651K_{58s}c_{80} + 90K_{5,10,s}c_{10,0} \\ \hline -4845K_{52s}c_{20} + 646K_{54s}c_{40} - 570K_{56s}c_{60} \\ + 105K_{58s}c_{80} - 9K_{5,10,s}c_{10,0} \end{array} \right\} \quad (\text{H10})$$

$$6128925\Lambda^{6s} = \left\{ \begin{array}{l} 1560090K_{62s}c_{20} + 917700K_{64s}c_{40} + 690000K_{66s}c_{60} \\ + 603750K_{68s}c_{80} + 623700K_{6,10,s}c_{10,0} + 1006236K_{6,12,s}c_{12,s} \\ \hline 1448655K_{62s}c_{20} + 699200K_{64s}c_{40} + 345000K_{66s}c_{60} \\ + 86250K_{68s}c_{80} - 193050K_{6,10,s}c_{10,0} - 862488K_{6,12,s}c_{12,s} \\ \hline 1114350K_{62s}c_{20} + 120175K_{64s}c_{40} - 379500K_{66s}c_{60} \\ - 612375K_{68s}c_{80} - 519750K_{6,10,s}c_{10,0} + 539055K_{6,12,s}c_{12,s} \\ \hline 557175K_{62s}c_{20} - 589950K_{64s}c_{40} - 741750K_{66s}c_{60} \\ - 163875K_{68s}c_{80} + 705375K_{6,10,s}c_{10,0} - 239580K_{6,12,s}c_{12,s} \\ \hline -222870K_{62s}c_{20} - 1048800K_{64s}c_{40} - 138000K_{66s}c_{60} \\ + 767625K_{68s}c_{80} - 410850K_{6,10,s}c_{10,0} + 71874K_{6,12,s}c_{12,s} \\ \hline -1225785K_{62s}c_{20} - 721050K_{64s}c_{40} + 86250K_{66s}c_{60} \\ - 474375K_{68s}c_{80} + 121275K_{6,10,s}c_{10,0} - 13068K_{6,12,s}c_{12,s} \\ \hline -2451570K_{62s}c_{20} + 1081575K_{64s}c_{40} - 379500K_{66s}c_{60} \\ + 94875K_{68s}c_{80} - 14850K_{6,10,s}c_{10,0} + 1089K_{6,12,s}c_{12,s} \end{array} \right\} \quad (\text{H11})$$

Next, consider the following numerical approximations to equations (H6) through (H11) for the fundamental resonances  $s = 0$ . Each expression represents a doubly degenerate eigenvalue except the first in each set, which is nondegenerate.

$$\Lambda^{10} = \begin{Bmatrix} +0.577 c_{20} \\ -0.288 c_{20} \end{Bmatrix} \quad (\text{H12})$$

$$\Lambda^{20} = \begin{Bmatrix} +0.285 c_{20} + 0.710 c_{40} \\ +0.142 c_{20} - 0.473 c_{40} \\ -0.285 c_{20} + 0.118 c_{40} \end{Bmatrix} \quad (\text{H13})$$

$$\Lambda^{30} = \begin{Bmatrix} +0.228 c_{20} + 0.338 c_{40} + 0.831 c_{60} \\ +0.171 c_{20} + 0.056 c_{40} - 0.628 c_{60} \\ -0.394 c_{40} + 0.249 c_{60} \\ -0.286 c_{20} + 0.169 c_{40} - 0.042 c_{60} \end{Bmatrix} \quad (\text{H14})$$

$$\Lambda^{40} = \begin{Bmatrix} +0.205 c_{20} + 0.252 c_{40} + 0.394 c_{60} + 0.945 c_{80} \\ +0.174 c_{20} + 0.126 c_{40} - 0.020 c_{60} - 0.756 c_{80} \\ +0.082 c_{20} - 0.154 c_{40} - 0.433 c_{60} + 0.378 c_{80} \\ -0.072 c_{20} - 0.294 c_{40} + 0.335 c_{60} - 0.108 c_{80} \\ -0.287 c_{20} + 0.196 c_{40} - 0.079 c_{60} + 0.013 c_{80} \end{Bmatrix} \quad (\text{H15})$$

$$\Lambda^{50} = \begin{Bmatrix} +0.193 c_{20} + 0.213 c_{40} + 0.287 c_{60} + 0.448 c_{80} + 1.051 c_{10,0} \\ +0.173 c_{20} + 0.143 c_{40} + 0.086 c_{60} - 0.090 c_{80} - 0.876 c_{10,0} \\ +0.116 c_{20} - 0.036 c_{40} - 0.259 c_{60} - 0.435 c_{80} + 0.500 c_{10,0} \\ +0.019 c_{20} - 0.071 c_{40} - 0.208 c_{60} + 0.467 c_{80} - 0.188 c_{10,0} \\ -0.116 c_{20} - 0.071 c_{40} + 0.345 c_{60} - 0.198 c_{80} + 0.042 c_{10,0} \\ -0.289 c_{20} + 0.071 c_{40} - 0.108 c_{60} + 0.032 c_{80} - 0.004 c_{10,0} \end{Bmatrix} \quad (\text{H16})$$



$$\Lambda^{60} = \left\{ \begin{array}{l} +0.185 c_{20} + 0.191 c_{40} + 0.237 c_{60} + 0.325 c_{80} + 0.500 c_{10,0} + 1.151 c_{12,0} \\ +0.172 c_{20} + 0.146 c_{40} + 0.118 c_{60} + 0.046 c_{80} - 0.155 c_{10,0} - 0.987 c_{12,0} \\ +0.132 c_{20} + 0.025 c_{40} - 0.130 c_{60} - 0.329 c_{80} - 0.417 c_{10,0} + 0.617 c_{12,0} \\ +0.066 c_{20} - 0.123 c_{40} - 0.255 c_{60} - 0.088 c_{80} + 0.565 c_{10,0} - 0.274 c_{12,0} \\ -0.026 c_{20} - 0.219 c_{40} - 0.047 c_{60} + 0.413 c_{80} - 0.329 c_{10,0} + 0.082 c_{12,0} \\ -0.145 c_{20} - 0.150 c_{40} + 0.030 c_{60} - 0.255 c_{80} + 0.097 c_{10,0} - 0.015 c_{12,0} \\ -0.291 c_{20} + 0.225 c_{40} - 0.130 c_{60} + 0.051 c_{80} - 0.012 c_{10,0} + 0.001 c_{12,0} \end{array} \right\}. \quad (\text{H17})$$

## APPENDIX I – Material Properties of Some Solids

The following table lists material properties of solids as gathered from a variety of sources. Neither the materials list nor the cited properties list is intended to be comprehensive. However, the lists reflect items of interest to fusion capsule fabricators and experimentalists. The given elastic constants are those for isotropic symmetry (assumed for polycrystalline samples). Many sound velocities are computed using  $c_S^2 = \mu/\rho$  and  $c_L^2 = (\lambda + 2\mu)/\rho$ . Note also the relationship between the Lamé constants and the standard crystallographic notation:  $\mu = c_{44}$ ,  $\lambda = c_{12}$ , and thus  $c_{11} = \lambda + 2\mu$ . All quantities are given in cgs units. Estimated quantities are marked with an asterisk.

Table II

Property	Al	Be	Cu	Au	SS304	D <sub>2</sub>	DT*
$T$	298	294	298	298	298	18.7	19.8
$\rho$	2.70	1.85	8.93	19.7	7.91	0.206	0.253
$\lambda$ ( $10^{11}$ )	6.14	1.712	10.6	15.0	11.3	0.018	0.021
$\mu$ ( $10^{11}$ )	2.49	14.87	4.83	2.84	7.60	0.021	0.024
$c_S$ ( $10^5$ )	3.04	8.96	2.33	1.20	3.10	1.00	0.97
$c_L$ ( $10^5$ )	6.42	13.04	4.76	3.24	5.79	1.70	1.65
$\rho c_L$ ( $10^4$ )	173	241	425	638	458	3.5	4.2

The tables on the following pages provide additional data on various materials over a range of temperatures. All values are in cgs units.

# Thermophysical Properties of Aluminum

$T$	$\rho$	$C_P$	$K$	$\rho C_P K$	$\lambda$	$\mu$	$c_S$	$c_L$	$\rho c_L$
		$10^7$	$10^7$	$10^{14}$	$10^{11}$	$10^{11}$	$10^2$	$10^2$	$10^4$
15	2.73	0.013	176	~6	---	---	---	---	---
20	2.73	0.02	117	~6	6.26	2.80	3200	6590	180
25	2.73	0.03	77.3	~6	---	---	---	---	---
50	2.73	0.15	12.3	5.0	---	---	---	---	---
75	2.73	0.35	4.39	4.2	---	---	---	---	---
100	2.73	0.49	3.02	4.0	6.25	2.76	3180	6570	179
125	2.73	0.60	2.70	4.4	---	---	---	---	---
150	2.72	0.69	2.48	4.7	6.23	2.71	3160	6540	178
175	2.72	0.76	2.42	5.0	---	---	---	---	---
200	2.72	0.80	2.37	5.2	6.20	2.64	3120	6500	177
225	2.71	0.83	2.36	5.3	---	---	---	---	---
250	2.71	0.86	2.35	5.5	6.17	2.57	3090	6460	175
275	2.70	0.88	2.36	5.6	---	---	---	---	---
300	2.70	0.90	2.37	5.8	6.14	2.49	3040	6420	173

# Thermophysical Properties of Beryllium

$T$	$\rho$	$C_P$	$K$	$\rho C_P K$	$\lambda$	$\mu$	$c_S$	$c_L$	$\rho c_L$
		$10^7$	$10^7$	$10^{14}$	$10^{11}$	$10^{11}$	$10^2$	$10^2$	$10^4$
15	1.86	0.01	26.8	~0.5	---	---	---	---	---
20	1.86	0.015	34.8	~1	1.60	15.2	9040	13100	244
25	1.86	0.02	41.2	~1.5	---	---	---	---	---
50	1.86	0.04	40.0	~3	---	---	---	---	---
75	1.86	0.08	18.9	~3	1.60	15.2	9040	13100	244
100	1.86	0.15	9.90	2.7	1.61	15.2	9040	13100	244
125	1.86	0.33	7.20	4.4	---	---	---	---	---
150	1.86	0.65	4.51	5.5	1.62	15.1	9030	13100	243
175	1.86	0.89	3.75	5.6	---	---	---	---	---
200	1.85	1.09	3.01	6.1	1.65	15.1	9030	13100	243
225	1.85	1.32	2.68	6.5	---	---	---	---	---
250	1.85	1.49	2.36	6.5	1.68	15.0	9000	13100	242
275	1.85	1.66	2.18	6.7	1.70	14.9	8970	13000	241
300	1.85	1.81	2.00	6.7	1.72	14.8	8940	13000	241

# Thermophysical Properties of Copper

$T$	$\rho$	$C_P$	$K$	$\rho C_P K$	$\lambda$	$\mu$	$c_S$	$c_L$	$\rho c_L$
		$10^7$	$10^7$	$10^{14}$	$10^{11}$	$10^{11}$	$10^2$	$10^2$	$10^4$
15	9.02	0.012	156	17	---	---	---	---	---
20	9.02	0.019	105	18	10.9	5.06	2370	4830	435
25	9.02	0.025	68.0	15	---	---	---	---	---
50	9.02	0.11	12.2	12	10.9	5.06	2370	4830	435
75	9.01	0.20	6.15	11	---	---	---	---	---
100	9.01	0.26	4.83	11	10.9	5.01	2360	4820	434
125	9.00	0.29	4.55	12	---	---	---	---	---
150	8.99	0.32	4.28	12	10.8	4.99	2360	4810	432
175	8.98	0.34	4.20	13	---	---	---	---	---
200	8.97	0.36	4.13	13	10.7	4.95	2350	4790	430
225	8.96	0.37	4.08	14	---	---	---	---	---
250	8.95	0.38	4.04	14	10.7	4.89	2340	4780	428
275	8.94	0.38	4.01	14	---	---	---	---	---
300	8.93	0.39	3.98	14	10.6	4.83	2330	4760	425

# Thermophysical Properties of Gold

$T$	$\rho$	$C_P$	$K$	$\rho C_P K$	$\lambda$	$\mu$	$c_S$	$c_L$	$\rho c_L$
		$10^7$	$10^7$	$10^{14}$	$10^{11}$	$10^{11}$	$10^2$	$10^2$	$10^4$
15	19.9	---	22.6	---	---	---	---	---	---
20	19.9	0.019	15.0	5.7	15.7	2.96	1220	3300	657
25	19.9	0.036	10.2	7.3	---	---	---	---	---
50	19.9	0.075	4.20	6.3	15.6	2.96	1220	3290	654
75	19.9	0.094	---	---	---	---	---	---	---
100	19.9	0.107	3.45	7.3	15.5	2.94	1220	3280	652
125	19.8	0.114	3.40	7.7	---	---	---	---	---
150	19.8	0.120	3.35	8.0	15.4	2.91	1210	3270	648
175	19.8	0.123	3.31	8.1	---	---	---	---	---
200	19.8	0.125	3.27	8.1	15.3	2.88	1210	3260	646
225	19.8	0.125	---	---	---	---	---	---	---
250	19.7	0.126	3.20	7.9	15.1	2.86	1200	3250	640
275	19.7	0.127	3.18	8.0	---	---	---	---	---
300	19.7	0.129	3.15	8.0	15.0	2.84	1200	3240	638

Thermophysical Properties of SS304

$T$	$\rho$	$C_P$	$K$	$\rho C_P K$	$\lambda$	$\mu$	$c_S$	$c_L$	$\rho c_L$
		$10^7$	$10^7$	$10^{14}$	$10^{11}$	$10^{11}$	$10^2$	$10^2$	$10^4$
15	7.98	---	0.014	---	---	---	---	---	---
20	7.98	---	0.020	---	11.5	8.00	3170	5870	468
25	7.98	---	0.027	---	---	---	---	---	---
50	7.98	0.27	0.055	0.12	11.5	7.99	3160	5870	468
75	7.98	---	0.075	---	---	---	---	---	---
100	7.97	0.33	0.090	0.24	11.4	7.94	3160	5850	467
125	7.97	---	0.10	---	---	---	---	---	---
150	7.96	0.36	0.11	0.32	11.4	7.87	3140	5840	465
175	7.95	---	---	---	---	---	---	---	---
200	7.94	0.40	0.12	0.38	11.3	7.78	3130	5820	462
225	7.93	---	---	---	---	---	---	---	---
250	7.92	0.44	0.14	0.49	11.3	7.69	3120	5800	460
275	7.91	---	---	---	---	---	---	---	---
300	7.90	0.465	0.15	0.55	11.3	7.60	3100	5790	458

Thermophysical Properties of Solid Hydrogens (near 18K)

	$\rho$	$C_P$	$K$	$\rho C_P K$	$\lambda$	$\mu$	$c_S$	$c_L$	$\rho c_L$
		$10^7$	$10^5$	$10^{12}$	$10^{11}$	$10^{11}$	$10^2$	$10^2$	$10^4$
H-H	0.087	3.1	0.30	0.08	0.010	0.011	1100	1880	1.6
H-D	0.139	3.0	---	---	0.015	0.015	1050	1790	2.5
H-T	0.190	2.9	---	---	0.017	0.020	1030	1750	3.3
D-D	0.197	2.7	0.31	0.18	0.018	0.021	1000	1700	3.5
D-T	0.253	3.5	---	---	0.021	0.024	970	1650	4.2
T-T	0.311	2.0	---	---	0.024	0.028	950	1600	5.0



## APPENDIX J – Physical Properties of Some Fluids

The following tables list material properties of gases and liquids gathered from a variety of sources. Neither the fluid list nor the cited properties list is intended to be comprehensive. However, the lists reflect items of interest to fusion capsule fabricators and experimentalists. For computational purposes a fluid can often be treated as a solid for which shear elastic constants are zero, thus the table includes an effective Lamé constant  $\lambda (= \rho c^2)$ . The data were taken from a variety of sources and estimated data are marked with an asterisk. All values are in cgs units unless otherwise noted. An excellent source for additional information on a variety of elemental gases is Friend (1992).

Table J1 – Physical Properties of Some Gases

property	air	D <sub>2</sub>	D <sub>2</sub>	D <sub>2</sub>	D-T	D-T	D-T	He-4
$T$	298	298	30	19	298	30	20	19
$P$ (atm)	1.00	350	4.43	0.192	350	3.92*	0.198	0.10
$\rho$ (10 <sup>-3</sup> )	1.225	47.3	8.24	0.050	53*	9.66*	0.0778	0.26
$c$ (10 <sup>2</sup> )	340	1141	320	259	1000*	290*	230*	258
$\rho c$	41.7	5400	264	1.30	5300*	280	1.79*	6.7
$\lambda$ (10 <sup>5</sup> )	14.2	6160	84.4	0.335	5300*	81.2	0.41*	1.7
$\eta$ (10 <sup>-3</sup> )	0.184	0.13	0.02*	0.013*	0.14*	0.02*	0.014*	0.195
$\eta_b$ (10 <sup>-3</sup> )	0.11	2.9*	0.4*	0.26*	1*	1*	1*	0
$C_P$ (10 <sup>7</sup> )	1.01	7.61	5.36	5.2	7.4*	5.5*	7.0*	5.3
$\bar{\gamma}$	1.40	1.41	2.37	1.66	1.4*	2.4*	1.66*	1.68
$K$ (10 <sup>3</sup> )	2.64	13	1.5	0.7	12*	1.5*	0.9*	2.5
$\rho C_P K$ (10 <sup>7</sup> )	3.27	4680	66.2	0.18	4706	80	0.49	3.45

Table J2 – Physical Properties of Some Liquids

property	water	D <sub>2</sub>	D <sub>2</sub>	D <sub>2</sub>	D-T	D-T	D-T
$T$	298	38	30	19	38	30	20
$P$ (atm)	1.00	16.5	4.32	0.192	15*	3.9*	0.22*
$\rho$	1.00	0.070	0.144	0.174	0.14*	0.19*	0.22*
$c$ (10 <sup>2</sup> )	1500	266	759	1074	240*	720*	940*
$\rho c$ (10 <sup>2</sup> )	1500	18.6	109	187	34*	136*	209*
$\lambda$ (10 <sup>9</sup> )	22.5	0.050	0.83	2.01	0.081*	0.98*	2.0*
$\eta$ (10 <sup>-3</sup> )	10	0.12*	0.21	0.47*	0.15*	0.24*	0.48*
$\eta_b$ (10 <sup>-3</sup> )	30*	---	---	---	---	---	---
$C_P$ (10 <sup>7</sup> )	4.19	51.4	10.2	5.50	55*	13*	7.7*
$\bar{\gamma}$	---	7.51	2.12	1.60	---	---	---
$K$ (10 <sup>3</sup> )	61	9.1	13.7	12.4	10*	15*	14*
$\rho C_P K$ (10 <sup>11</sup> )	26	3.3	2.0	1.2	7.7	3.7	2.4

The following table lists critical data for the vapor phase of the hydrogen isotopes as given by Souers (1986). The subscripts *CP* and *TP* indicate critical point data and triple point data, respectively. Estimated data are marked with an asterisk.

Table J3 – Critical Data for the Hydrogen Isotopes

property	nH <sub>2</sub>	H-D	H-T	nD <sub>2</sub>	D-T	T <sub>2</sub>
<i>M</i> (g/mol)	2.0156	3.0219	4.0239	4.0282	5.0302	6.0321
<i>T<sub>CP</sub></i> (K)	33.19	35.91	37.13*	38.34	39.42*	40.44*
<i>P<sub>CP</sub></i> (atm)	12.98	14.65	15.50*	16.43	17.50*	18.26*
<i>ρ<sub>CP</sub></i> (kg/m <sup>3</sup> )	3.10*	4.84*	6.60*	6.77*	8.75*	10.7*
<i>T<sub>TP</sub></i> (K)	13.96	16.60	17.70*	18.73	19.79*	20.62
<i>P<sub>TP</sub></i> (atm)	0.0711	0.1221	0.1439*	0.1693	0.1982*	0.2132
<i>ρ<sub>TP</sub></i> (kg/m <sup>3</sup> )	0.0127	0.0276*	0.0406*	0.0455*	0.0629*	0.0778*

## APPENDIX K – Thermal Expansion Properties of Some Solids

The linear thermal expansion of many materials from 0K to 300K is well described by the equation

$$\frac{L_{293} - L_T}{L_{293}} \times 10^5 = a_0 + a_1 \tilde{T} + a_2 \tilde{T}^2 + a_3 \tilde{T}^3 + a_4 \tilde{T}^4 + a_5 \tilde{T}^5 \quad (\text{J1})$$

where  $\tilde{T} \equiv T/100K$ ,  $L_{293}$  is the object length at 293K, and  $L_T$  is the length at Kelvin temperature  $T$ . The coefficients  $a_n$  for various materials given in the following table were derived from data compiled by Corruccini and Gniewek (1961).

Table K1

	Al	Be	Cu	Au	SS304
$a_0$	+415.0	+131.0	+326.0	+324.0	+296.0
$a_1$	+10.97	-2.545	+18.26	+17.70	+17.73
$a_2$	-21.04	+10.84	-54.24	-137.8	-34.81
$a_3$	-58.27	-11.92	-17.67	+67.73	-32.28
$a_4$	+26.76	+0.2377	+12.93	-17.31	+18.00
$a_5$	-3.578	+0.3042	-1.952	+1.755	-2.610

## APPENDIX L – Thermodynamic Relations

An excellent thermodynamics reference is Callen (1985). A brief summary of useful relations is given here. The specific heats at constant pressure and constant volume (density) are

$$C_P = T \left( \frac{\partial s}{\partial T} \right)_P, \quad (\text{L1})$$

$$C_V = T \left( \frac{\partial s}{\partial T} \right)_V. \quad (\text{L2})$$

The isentropic and isothermal compressibilities are

$$\kappa_s = -\frac{1}{V} \left( \frac{\partial V}{\partial P} \right)_s = \frac{1}{\rho} \left( \frac{\partial \rho}{\partial P} \right)_s, \quad (\text{L3})$$

$$\kappa_T = -\frac{1}{V} \left( \frac{\partial V}{\partial P} \right)_T = \frac{1}{\rho} \left( \frac{\partial \rho}{\partial P} \right)_T. \quad (\text{L4})$$

The coefficient of thermal expansion is

$$\alpha_T = \frac{1}{V} \left( \frac{\partial V}{\partial T} \right)_P = -\frac{1}{\rho} \left( \frac{\partial \rho}{\partial T} \right)_P. \quad (\text{L5})$$

The adiabatic sound speed is

$$c^2 = \left( \frac{\partial P}{\partial \rho} \right)_s. \quad (\text{L6})$$

These six quantities, equations (L1) through (L6), are thermodynamically linked in a number of ways. Some useful relations are

$$\bar{\gamma} \equiv \frac{C_P}{C_V} = \frac{\kappa_T}{\kappa_s}, \quad (\text{L7})$$

$$C_P = C_V + \frac{TV\alpha_T^2}{\kappa_T}, \quad (\text{L8})$$

$$c^2 = \frac{1}{\bar{\gamma}} \left( \frac{\partial P}{\partial \rho} \right)_T = \frac{\bar{\gamma}}{\rho \kappa_T} = \frac{1}{\rho \kappa_s}, \quad (\text{L9})$$

$$\bar{\gamma} - 1 = \frac{TV\alpha_T^2 \rho c^2}{C_P}. \quad (\text{L10})$$

Other miscellaneous thermodynamic relations are listed below.

$$\left( \frac{\partial s}{\partial V} \right)_T = \left( \frac{\partial P}{\partial T} \right)_V \quad (\text{L11})$$

$$\left( \frac{\partial X}{\partial Y} \right)_Z = - \frac{(\partial Z / \partial Y)_X}{(\partial Z / \partial X)_Y} \quad X, Y, Z \in \{P, T, V, s\} \quad (\text{L12})$$

$$\frac{\partial \rho}{\rho} = - \frac{\partial V}{V}. \quad (\text{L13})$$

## APPENDIX M – Representative ICF Capsule Properties

Figure M1 shows the basic geometric properties and fuel characteristics of a representative ICF capsule. The two sections are 60-degree planar slices of spherical capsules. At room temperature, the DT gas fuel is of a density to produce 350 atm of pressure. The shell thickness is 150  $\mu\text{m}$ . The same capsule brought below the DT triple point will form a solid fuel layer, evenly distributed around the inside of the capsule (beta-layering). This solid is in equilibrium with its DT vapor at about 0.19 atm.

---

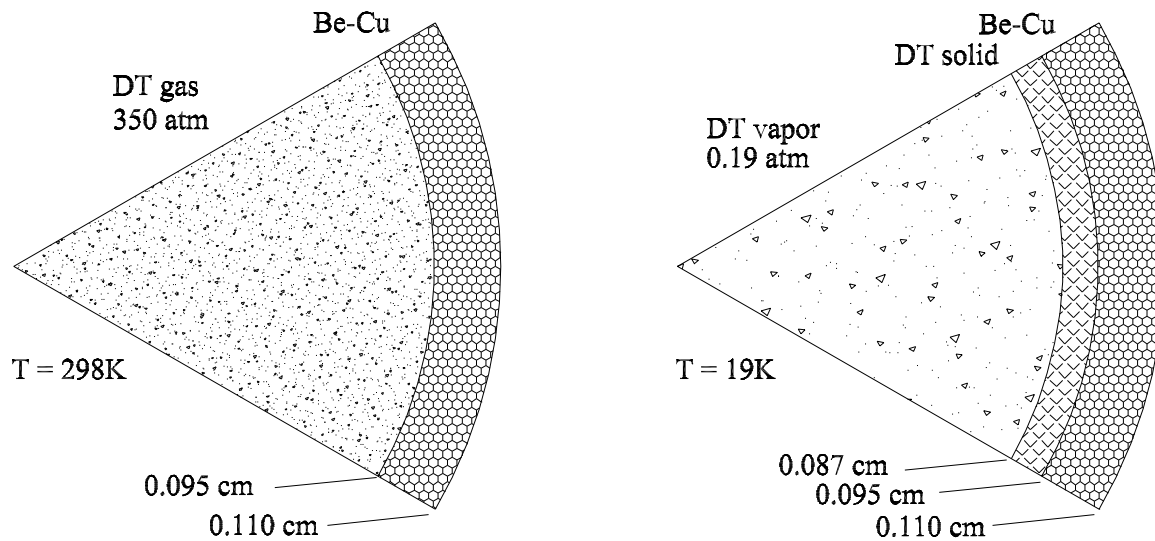


Figure M1

## APPENDIX N – Notation and Units Summary

A theoretical exposition of this nature requires many symbols representing seemingly innumerable physical quantities. Certain diacritics are used as universal modifiers; these are listed in the first table. Care has been taken to use a symbol set with few ambiguities, and in these cases the intended symbol meaning should be clear. The second table lists most of the symbols used in this work. A discussion at the end clarifies the use of units.

### Diacritics

$x_0$	ambient conditions of $x$
$x'$	acoustic property $x$ (when used as a physical property modifier)
$\tilde{x}$	effective $x$ for a nearly spherical cavity
$x_{sh}$	shell property $x$
$x_v$	viscous property of $x$
$x_t$	thermal property of $x$
$x_\rho$	density wave property of $x$
$x_{CP}$	critical point property
$x_{TP}$	triple point property
$\ell$	resonance order number
$m$	resonance azimuthal number
$s$	resonance radial overtone number
$p$	deformation order number
$q$	deformation azimuthal number

### Symbols

$a$	spherical cavity radius
$a_{\ell m}$	velocity potential expansion coefficients
$b_{\ell m}$	model perturbation expansion parameters



$\mathbf{B}$	nonradial-frequency perturbation eigenmatrices
$c$	adiabatic sound speed
$c_L$	longitudinal wave speed
$c_S$	shear wave speed
$c_{pq}$	general cavity perturbation parameter
$C, \tilde{C}$	Clebsch-Gordan coefficients
$\mathbf{C}_P$	cavity property set derived from $\mathbf{F}_L$
$C_P, C_V$	specific heats at constant pressure and volume
$f$	frequency
$\underline{E}$	complex frequency
$\mathbf{F}_L, \tilde{\mathbf{F}}_L$	eigenfrequency sets for theoretical evaluation
$\bar{g}$	angular perturbation function
$g_b$	bulk dissipation
$g_{\ell m}$	$P_{\ell m}$ to $Y_{\ell m}$ conversion constant
$i = \sqrt{-1}$	imaginary unit
$j_\ell(z)$	spherical Bessel functions of the first kind of order $\ell$
$k$	acoustic wavenumber
$k_0$	acoustic wavenumber in the absence of viscous and thermal effects
$\Delta k$	viscous and thermal correction to $k_0$
$K$	coefficient of thermal conductivity
$\ell, \ell'$	resonance order number
$m, m'$	resonance azimuthal number
$p$	deformation order number
$P = P_0 + P'$	fluid pressure
$P_{\ell m}$	Legendre polynomial functions
$q$	deformation azimuthal number

$Q$	resonance “quality” factor
$r$	radial coordinate
$s = s_0 + s'$	fluid entropy
$S_{\ell s}$	radial eigenfrequency constants
$t$	time
$T$	temperature
$\vec{v} = \vec{v}_0 + \vec{v}'$	fluid velocity
$V$	cavity volume -also- thermodynamic volume
$\vec{w}'$	divergence-free acoustic velocity
$w_1, w_2$	transverse velocity field solution coefficients
$y_1, y_2, y_3, y_4$	Alterman (1959) calculation parameters
$Y_{\ell m}$	spherical harmonic functions
$z = ka$	roots of spherical Bessel function derivatives
$Z, \hat{Z}$	useful constants relating $z$ quantities
$\alpha$	internal fluid to external shell wall displacement ratio
$\alpha_T$	coefficient of thermal expansion
$\beta$	radii perturbation parameter -also- acoustic admittance
$\gamma$	lateral shift perturbation parameter
$\bar{\gamma} = C_P / C_V$	ratio of specific heats
$\Lambda$	eigenvalues of matrix <b>B</b>
$\delta_v, \delta_t$	viscous and thermal penetration lengths
$\bar{\delta}_v$	shear viscous penetration length
$\varepsilon, \varepsilon_{\ell m}$	small expansion parameters
$\kappa_s$	adiabatic compressibility
$\kappa_T$	isothermal compressibility
$\lambda, \mu$	isotropic solid Lamé constants

$\eta, \eta_b$	coefficients of shear and bulk viscosity
$\rho = \rho_0 + \rho'$	fluid density
$\sigma$	elongation perturbation parameter
$\theta$	polar coordinate
$\phi$	azimuthal coordinate
$\psi$	spatial velocity potential
$\Psi$	velocity potential
$\omega = 2\pi f$	angular frequency

## Units

Throughout this report cgs units are the units of choice. Notable exceptions are references to pressure in atmospheres and distances in microns. The following table lists the cgs units for various quantities.

temperature	$K$
distance	$cm$
time	$s$
mass	$g$
speed	$cm / s$
force	$dyne = g \cdot cm / s^2$
energy	$erg = g \cdot cm^2 / s^2$
density	$g / cm^3$
pressure, elasticity	$dyne / cm^2 = g / cm \cdot s^2$
thermal conductivity	$erg / cm \cdot s \cdot K = g \cdot cm / K \cdot s^3$
specific heat	$erg / K = g \cdot cm^2 / K \cdot s^2$
viscosity	$dyne \cdot s / cm^2 = g / cm \cdot s$

## APPENDIX O – References

- Alterman, Z., *et al.*, “Oscillations of the earth,” *Proc. Roy. Soc. London*, **252**, 80 (1959).
- Arfken, G., *Mathematical Methods for Physicists*, Academic Press, New York (1985).
- Callen, H. B., *Thermodynamics and an Introduction to Thermostatistics*, John Wiley & Sons, New York (1985).
- Corruccini, R. J. and Gniewek, J. J., “Thermal expansion of technical solids at low temperatures,” *National Bureau of Standards Monograph* 29 (1961).
- Friend, D. G., *NIST Standard Reference Database 12* (software), Fluid Mixtures Data Center, Thermophysical Division, NIST, Boulder CO (1992).
- Fetter, A. L. and Walecka, J. D., *Theoretical Mechanics of Particles and Continua*, McGraw-Hill, New York (1980).
- Hoffer, J. K. and Foreman, L. R., “Radioactively induced sublimation in solid tritium,” *Phys. Rev. Lett.*, **60**, 1310 (1988).
- Love, A. E. H., *The Mathematical Theory of Elasticity*, Dover, New York (1944).
- MacRobert, T. M., *Spherical Harmonics: An Elementary Treatise on Harmonic Functions with Applications*, Dover, New York (1948).
- Mehl, J. B., “Acoustic resonance frequencies of deformed spherical resonators,” *J. Acoust. Soc. Am.*, **71**, 1109 (1982).
- Mehl, J. B., “Spherical acoustic resonator: Effects of shell motion,” *J. Acoust. Soc. Am.*, **78**, 782 (1985).
- Mehl, J. B., “Acoustic resonance frequencies of deformed spherical resonators II,” *J. Acoust. Soc. Am.*, **79**, 278 (1986).
- Moldover, M. R., Mehl, J. B., and Greenspan, M., “Gas-filled resonators: Theory and experiment,” *J. Acoust. Soc. Am.*, **79**, 253 (1986).
- Morse, P. M. and Feshbach, H., *Methods of Theoretical Physics: Part II*, McGraw-Hill (1953).

- Pierce, A. D., *Acoustics: An Introduction to Its Physical Principles and Applications*, Acoustical Society of America, New York (1989).
- Rose, M. E., *Elementary Theory of Angular Momentum*, John Wiley & Sons, New York (1957).
- Souers, P. C., *Hydrogen Properties for Fusion Energy*, University of California Press, Berkeley (1986).